UNIVERSITY OF SOUTHAMPTON

FACULTY OF FACULTY OF ENGINEERING AND THE ENVIRONMENT

Department of Mechanical Engineering

Volume 1 of 1

Mechanisms of Encrustation within Ureteral Stents

by

Ali Mosayyebi

Thesis for the degree of Doctor of Philosophy

March 2018

UNIVERSITY OF SOUTHAMPTON

ABSTRACT

FACULTY OF ENGINEERING AND THE ENVIRONMENT

Bioengineering Science Research Group

Thesis for the degree of Doctor of Philosophy

MECHANISMS OF ENCRUSTATION WITHIN URETERAL STENTS

Ali Mosayyebi

Ureteric obstructions due to intrinsic or extrinsic causes (e.g., stones, tumours, and fibrosis) can impair urine flow, resulting in pain, urinary tract infection, and kidney damage. Ureteral stenting is one of the most effective and least invasive clinical procedures for restoring urine drainage in the occluded ureter. A ureteric stent is a hollow tube with side-holes, which allows the urine to bypass the source of obstruction. Despite their clinical success, stents often suffer from failures and side effects that impact on both patient's quality of life and costs for national health services. One of the most common complications is encrustation of the stent's surface caused by calcifications, and particularly of side-holes, which are essential for maintaining urine drainage. Despite efforts have been devoted to develop novel materials and stent coatings; encrustation still remains a major complication. Few studies have however suggested that flow dynamics can potentially govern formation and deposition of encrusting crystals; however, improvements to the flow performance of stents are hindered by a lack of quantitative correlation between flow and encrustation processes. This study aims to develop a novel ureteric stent architecture, which flow performance is designed to reduce encrustation rates. In a first step of the study, a correlation between flow metrics – specifically wall shear stress (WSS) - and the accumulation of encrusting particles in stents was investigated. For this purpose, microfluidic-based models of the occluded and stented ureter (referred to as 'stent-on-chip' models) were developed, replicating the complexity of the WSS field at key hydrodynamic regions of interest (such as side-holes of the stent and the cavity formed by a ureteric occlusion). Using this model, a robust and inverse correlation between WSS and size/growth rate of encrusting deposits was demonstrated. Critical regions suffering from low WSS, and thus prone to faster encrustation, were also identified. These included holes that did not experience flow exchange between the stent and the ureter (referred to as 'inactive' holes), and the occluded cavity. The presence of these critical regions was also verified at a full-scale, both experimentally and numerically, to further validate the ability of

microfluidic-based models to replicate relevant flow domains of a stented ureter. Stent-on-chip models were then employed as a technology platform to screen the effect of changing different architectural features of the stent. Changes to the thickness and shape of the side-holes were investigated, with a focus on those alterations that could be easily implemented within industrial constraints. A novel stent design, combining optimal thickness and a triangular hole shape, was developed; it showed significantly lower encrustation rates when compared to a standard stent design. Finally, a fabrication method was developed and validated for fabricating triangular side-holes on a commercial ureteric stent. The developed stent design and fabrication method are easy-to-implement and thus the novel stent prototype can be potentially employed as an adjuvant approach to existing material and surface coatings against encrustation. Future pre-clinical investigations are required to evaluate the potential clinical benefit of the proposed stent design.

Table of Contents

Table of Tables

Table of Figures

Table of Figures

Table of Figures

List of Accompanying Materials

Research Outputs

Patents (relevant to this thesis)

- **Mosayyebi**, X. Zhang, C. Manes, D. Carugo; *UK priority patent | application GB1714337.1 | filed 6th September 2017 | Patent Title: Stent with streamlined side-holes*

Enterprise (relevant to this thesis)

- Co-founder of SimpleStent | More information: https://futureworlds.com/discover-simple-stents-transforming-ureteral-stenting/

Scientific network establishment (relevant to this thesis)

- Establishment of SUSNet (Southampton Urinary System Network) | More information: https://www.southampton.ac.uk/minather/susnet.page?

Peer-reviewed journal publications (relevant to this thesis)

- **A. Mosayyebi**, A. Vijayakumar, Q. Y. Yue, E. Bres-Niewada, C. Manes, D. Carugo and B. K. Somani; *Engineering solutions to ureteral stent: material, coating and design*; Central European journal of urology. 2017;70 (3):270.
- **A. Mosayyebi**, C. Manes, D. Carugo, B. K. Somani; *Advances in Ureteral Stent Design and Materials*; Current Urology Reports (Invited Review - Accepted) – Chapter 2
- **A. Mosayyebi**, Q. Y. Yue, B. K. Somani, X. Zhang, C. Manes and D. Carugo; *Particle accumulation in ureteric stents is governed by fluid dynamics: in-vitro study using a 'stent-on-chip' model*; Journal of Endourology (Accepted with revisions) – Chapter 3
- **A. Mosayyebi**, X. Zhang, B. K. Somani, D. Lange, C. Manes and D. Carugo; *Decreasing deposition of encrusting particles in stents using material- and coating-independent designs;* Biomicrofluidics (Submitted – under review) – Chapter 5

Conference Proceedings (relevant to this thesis)

- **Mosayyebi**, X. Zhang, D. Carugo and C. Manes; *Effect of fluid dynamics on encrustation in a microfluidic model of the occluded and stented ureter*; MicroTAS (October 2016 - Dublin)
- **Mosayyebi**; *Investigating the flow dynamics in the obstructed and stented ureter by means of a biomimetic artificial model*; 35th World Congress of Endourology (September 2017 - Canada) – **Invited Speaker**
- **Mosayyebi**, B. K. Somani, X. Zhang, C. Manes and D. Carugo; Accumulation of stent encrustations depends on fluid dynamics: In-vitro study on a stent-on-a-chip model; EULIS (October 2017 - Austria)
- **Mosayyebi**, X. Zhang, C. Manes and D. Carugo; Stented ureter on a chip; CBE Biofilm Meeting (February 2018 - USA)
- **Mosayyebi**, X. Zhang, D C. Manes and D. Carugo; Stent on a Chip: a platform to study the deposition of encrusting bodies; CBE Biofilm Meeting (July 2018 - USA) – Upcoming
- **A. Mosayyebi**; D. Lange, B. K. Somani, X. Zhang, C. Manes, D. Carugo; *Full-scale study of the flow field in stented ureter models: In-vitro & In-silico*, 36th World Congress of Endourology (September 2018 - France)
- **A. Mosayyebi**, K. Looi, E. Newman, A. Tan, D. Carugo; *Study of the Flow Field - in In-vitro & In-silico Stented Ureter Models*; BioMedEng18 (September 2018, London)

Peer-reviewed journal publications (others)

- E. Bottaro, **A. Mosayyebi**, D. Carugo*, and C. Nastruzzi; *Analysis of the diffusion process by pH indicator in microfluidic chips for liposome production*; Micromachines
- C. L. Sones, I. N. Katis, B. Mills, M. Feinäugle, **A. Mosayyebi**, J. Butement, R. W. Eason; *Rapid and mask-less laser-processing technique for the fabrication of microstructures in polydimethylsiloxane*; Applied Surface Science
- D. A. Cristaldi, F. Yanar, **A. Mosayyebi**, P. G. Manrique, D. Carugo, E. Stulz, X. Zhang; Easy-to-perform and cost-effective fabrication of continuous-flow reactors and their applications for nanomaterials synthesis; New Biotechnology

Conference proceedings (others)

- C. L. Sones, I. N. Katis, P. He, B. Mills, **A. Mosayyebi**, J. Butement, M. Feinäugle, R. W. Eason; *Laser-based printing and patterning for biological applications*; International Workshop on the Fabrication and Application of Microstructured Optical Devices Keio University, Hiyoshi Campus, (February 2014 – Japan) – **Invited**
- **Mosayyebi**, A. Karabchevsky, J. S. Wilkinson; *Nanoparticle-enhanced chemiluminescence in micro-flow injection analysis*; 6th Mediterranean Conference on Nano-Photonics (MediNano-6) (October 2013 – France)
- L. Sones, I. N. Katis, B. Mills, M. Feinäugle, **A. Mosayyebi**, J. Butement, R. W. Eason; *Mask-less laser-machining for rapid low-cost patterning of microstructures in polydimethylsiloxane (PDMS)*; E-MRS '13 Materials Research Society Spring Meeting (May 2013 – Germany)
- L. Sones, I. N. Katis, B. Mills, M. Feinäugle, **A. Mosayyebi**, J. Butement, R. W. Eason; *Rapid low-cost patterning of microstructures in polydimethylsiloxane via mask-less laser-machining*; CLEO/Europe-IQEC 2013 (May 2013 – Germany)

Awards and Prize

- Conference grant awarded from IMechE to attend MicroTAS2016 in Dublin in October 2016.
- Young Investigator Award from Centre for Biofilm Engineering and an opportunity to discuss face to face with Food and Drug Administration (FDA) in the Washington DC in February 2018.
- STSM research grant awarded by the COST Action “European network of multidisciplinary research to improve the urinary stents” (CA16217), and conducted in collaboration with the University of Bern.

Academic Thesis: Declaration Of Authorship

I, ... Ali Mosayyebi

declare that this thesis and the work presented in it are my own and has been generated by me as the result of my own original research.

Mechanisms of Encrustation within Ureteral Stents .....

.....

I confirm that:

1. This work was done wholly or mainly while in candidature for a research degree at this University;
2. Where any part of this thesis has previously been submitted for a degree or any other qualification at this University or any other institution, this has been clearly stated;
3. Where I have consulted the published work of others, this is always clearly attributed;
4. Where I have quoted from the work of others, the source is always given. With the exception of such quotations, this thesis is entirely my own work;
5. I have acknowledged all main sources of help;
6. Where the thesis is based on work done by myself jointly with others, I have made clear exactly what was done by others and what I have contributed myself;
7. Parts of this work have been published as:

Signed: .....

Date: .....

Acknowledgements

Hereby, I would like to say thanks to my supervisory team Dr Dario Carugo, Dr Costantino Manes and Dr Xunli Zhang who have been supporting and supervising me since I started this project. Especially Dr Dario Carugo and Dr Costantino Manes for continuous support at every single step of my project, spiritually and even financially. Special thanks to my parents, as I would have not had the opportunity to be in the current position I am in without their support. Also, my friends Ms Sarvenaz Sohrabi, Ms Sarvin Nouroozi, Mr Antonio Di Grazia, Dr Sarchil Qadar, Ms Daniella Ivanova, Ms Marieta Marinova, Mr Rene Kaufmann for their kind support during my study.

I would like to thank everyone who kindly supported me during my study taking from Ms Sue Berger, Ms Katherine Daye, Ms Fionna Haigh, Ms Gwyneth Skiller, Prof Martin Browne, Prof Philippa Reed, Dr Andrew Chipperfield, Prof Tim Leighton, Prof Claudio Nastruzzi, Prof Mandy Fader, Prof Bill Keevil, Dr Sandra Wilks, Dr Gustavo A. M. de Almeida, Research and Innovation Services team, University Advice Centre, University International Office, University Digital Learning team, University incubator team (FutureWorlds), to our collaborators Dr Francesco Clavica, Dr Bhaskar Somani, Dr Dirk Lange, NAMRIP, μ-VIS for their support during my research.

Definitions and Abbreviations

2D – two dimensional

BPH - bening prostatic hypeoplasia

CAD – computation assisted design

CAGs - glycosmainoglycans

CFD – computational flaid dynamics

DLC – diamond–like carbon

ER – external radius

FDA – food & drug administration

FSI – Fluid structure interaction

IR – internal radius

Nitinal - nickel titanium

NO – non-occluded

NU – non-uniform wall

O - occluded

PC – phosphoryl choline

PDMS - poly dimethylsilmane

PMMA - poly methyl methacrylate

PTEF – polytetraflaoroethylene

PUA – polyvinylalchokol

SoC – stent on chip

T – wall thickness

U – uniform wall

UPJ – ureteropelvice junction

UTI - urinary tract infection

VUJ – vesicoureteric junction

WSS – wall shear stress

Chapter 1 Introduction

1.1 Outline

This chapter provides first an overview of the anatomy and physiology of the urinary system. It subsequently describes a common pathological condition, known as obstructive uropathy, and focuses on different sources of ureteric obstruction and related physiological implications. The function of ureteral stents in the treatment and management of ureteric obstructions is then introduced. Particular attention is devoted to complications and side effects associated with ureteral stenting.

Finally, the chapter outlines the main aim of the thesis and the individual objectives, with reference to the specific chapters where these are addressed. The main aspects of novelty of the work presented in this thesis are also described.

1.2 Urinary System

The urinary system comprises multiple biological entities that together contribute to excrete waste products of metabolism and maintain the stable physico-chemical environment required for cell and tissue functioning (i.e., homeostasis). This is achieved through a series of important functions, including [1]:

- Chemical and physical regulation
    - Water and blood volume management;
    - Control of electrolytic concentration and stabilisation of pH levels in blood;
    - Activation of Vitamin-D, controlling absorption of calcium and phosphorus in the body.
- Production of biological catalysts and signalling molecules
    - Release of the hormone *erythropoietin*, which triggers production of red blood cells in the bone marrow;
    - Secretion of the enzyme *renin*, which is involved in blood pressure regulation.
- Waste management

- Formation (kidneys), transport (ureters), storage (bladder), and release (urethra) of waste products in the form of urine;
- Excretion of waste products such as ammonia and creatinine. Ammonia is converted into the less toxic urea in the liver.

These functions involve the different constituents of the urinary system, comprising kidneys, ureters, bladder, and urethra (see Figure 1-1)

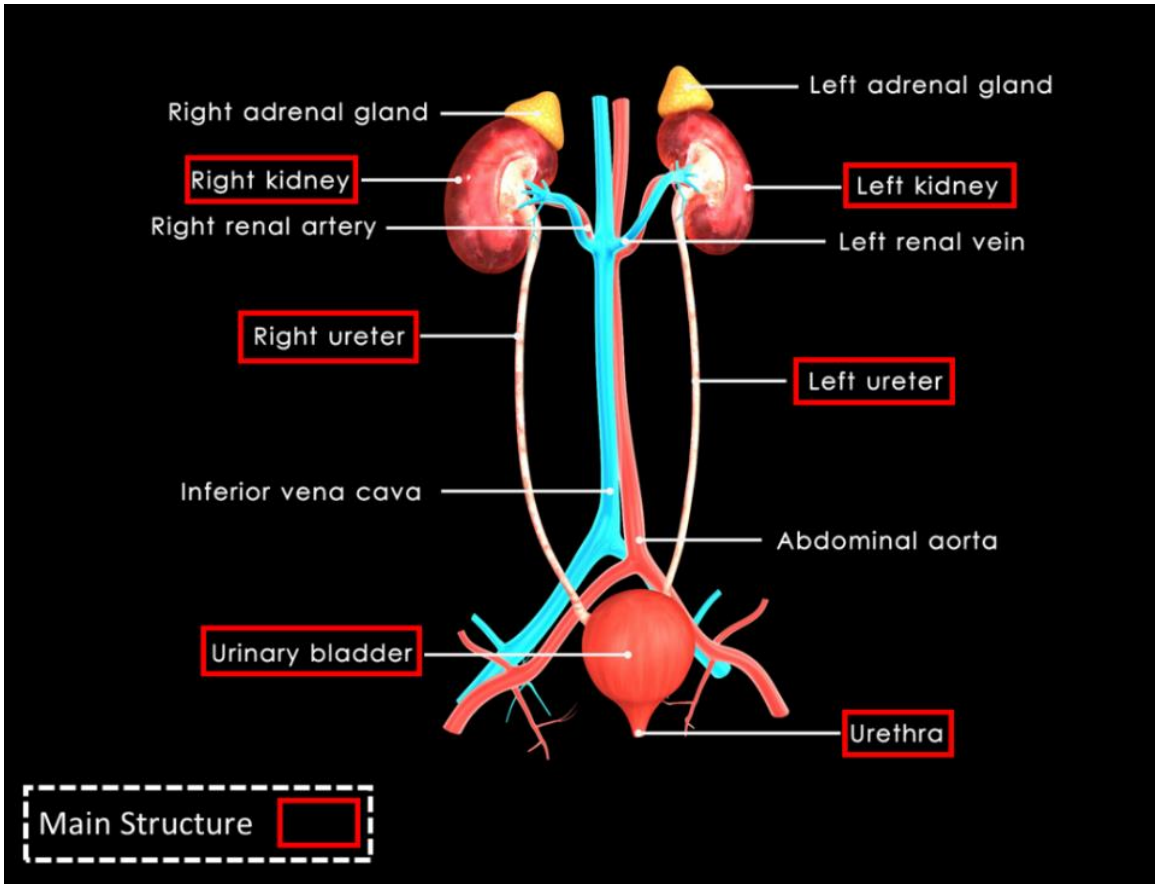

Figure 1-1 Anatomical structure of the human urinary system and the corresponding peripheral haematic circulation. The main constituents are highlighted within red rectangular boxes, and include two kidneys, two ureters, one bladder, and one urethra. The image has been purchased from iStock (Canada) and re-adapted.

The ureter is a collapsible, muscular tube approximately 30 cm long and extending from kidneys to the bladder [2]. Each ureter consists of three layers of tissue:

1. *Inner mucosa*, comprising epithelium and vascularised connective tissue. It secretes mucus, which coats and protects the cells' surface.

2. *Muscular coat*, which is responsible for the peristaltic motion of the ureter driving urine into the bladder.
3. *Fibrous coat*, comprising a supporting layer of fibrous connective tissue to anchor the ureter to neighbouring tissues.

1.3 Obstructive Uropathy

"Obstructive uropathy" refers to an impairment of urine flow within the urinary tract, usually caused by a physical constriction that may alter the physiological flow dynamics of urine (also known as urodynamics) [3, 4]. Obstructive events may interest different tracts of the urinary system, and frequently localise within ureters. There are distinct types of pathological obstruction, usually classified as intrinsic (e.g., caused by kidney stones occluding the ureter lumen) or extrinsic (e.g., caused by tumors, such as prostatic or bladder tumours, externally compressing on the urinary tract) (see Figure 1-2) [5]. Based on data from the National Health Service (NHS), every year 15% of men and 10% of women are diagnosed with kidney stone disease in the UK [6]. Moreover, this pathological condition affects 16% of men and 8% of women in the US [7], and 12% of the total population in Canada [8] every year. Furthermore, more than 20% of men are diagnosed with prostate cancer in Europe, and 2.7 million people worldwide are diagnosted with bladder cancer [9] every year.

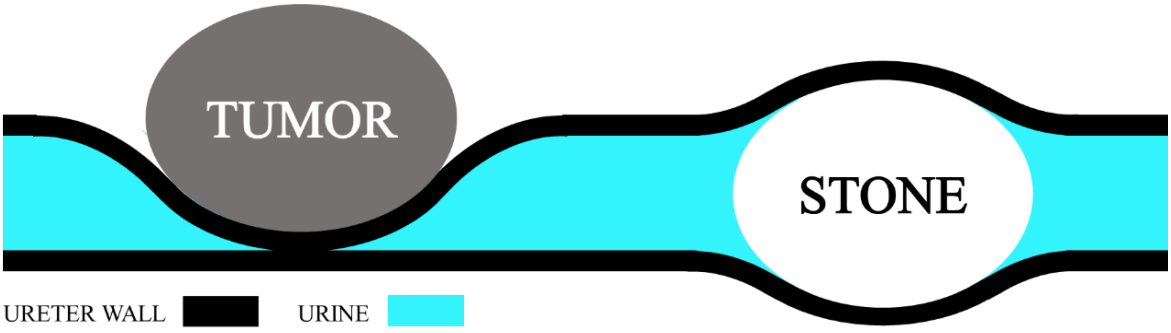

Figure 1-2 Schematic depiction of extrinsic (e.g. tumour) and intrinsic (e.g. kidney stone) causes of ureteral obstructions. In both cases, the physiological urine flow through the ureter lumen is significantly compromised.

From a functional perspective, an obstruction of the ureter lumen results in a significant decrease of its hydraulic diameter, causing abnormally elevated renal pelvic pressures (>20 cmH_2O, according to Fung et al. [10]) and potentially leading to irreversible kidney damage. Localised

dilation of the ureter lumen and urinary reflux (i.e., urine flow from the bladder towards the kidneys) can also occur in association with obstructive events. Urinary backflow can drive bacterial pathogens into the kidneys, potentially causing infection of extended compartments of the urinary system [11-13].

Obstructive uropathy is associated with a number of symptoms such as flank pain, fever, nausea or vomiting, presence of blood in urine (or haematuria), slow and frequent urination, and painful micturition (or dysuria) [14]. Common diagnostic procedures include ultrasound of the abdomen, X-ray based examinations including intravenous pyelogram (IVP) [15] and voiding cystourethrogram (VCUG) [16, 17], renal nuclear medicine scan [18], and magnetic resonance imaging (MRI) [19].

There are three common treatment options against obstructive uropathy: (i) surgery, such as ureteroscopic excision, which is a method commonly used for removing tumour masses, polyps, or scar tissue covering the urinary tract [20]; (ii) high intensity ultrasound-based treatments (i.e. lithotripsy [21]), which involve the use of shock waves to break large kidney stones into smaller fragments [22]; and (iii) placement of a ureteral stent, which is regarded as a temporary and minimally invasive procedure allowing urine to bypass a source of obstruction [11].

1.4 Ureteral stenting

Ureteral stents represent the main focus of the present study, and are largely employed in the clinic as a temporary measure to retrieve urine drainage when this is impaired by an obstruction of the ureter lumen. Compared to other treatment options, stenting can be potentially performed in an outpatient setting, without the need for anaesthesia [23]. A common stent architecture employed for the treatment of intrinsic or extrinsic ureteric occlusions consists of a ~18-40 cm long polymeric hollow tube. It contains numerous side-holes across its wall, and pig tales (also known as J-ends) for anchoring to the kidney pelvis and bladder, respectively, and preventing migration [24]. Side-holes provide pathways for urine to bypass the occlusion, and are manually punched alongside the stent at almost equally spaced positions (see Figure 1-3).

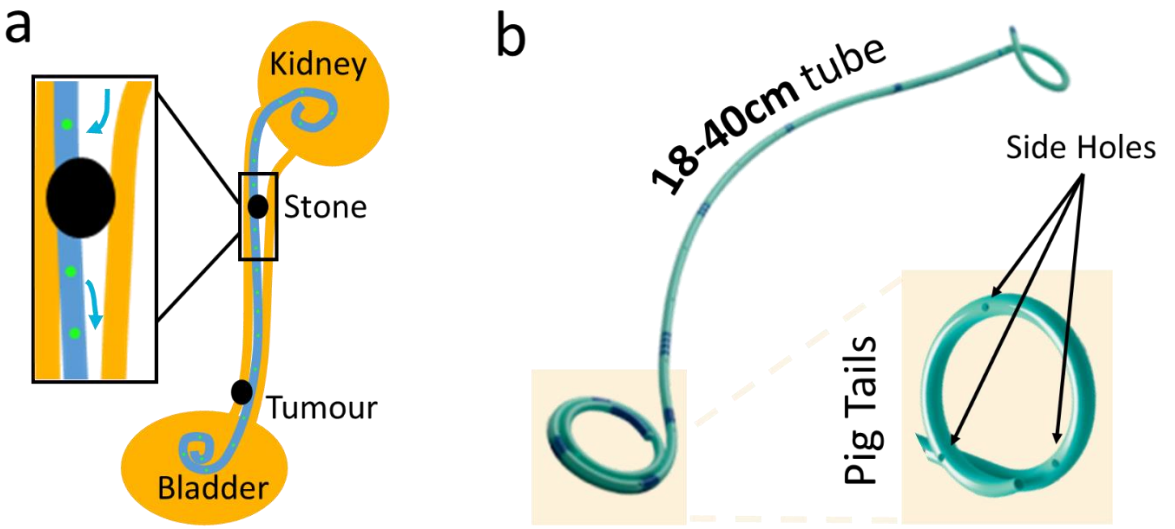

Figure 1-3. a) Schematic depiction of the stented urinary tract, demonstrating the functioning principle of a ureteric stent. The blue arrows indicate urine flow direction, before and after the obstruction. b) Image of a typical ureteral stent. The inset shows a zoomed-in view of one of its pig tales, which provide anchoring of the stent in both kidney pelvis and bladder. Black arrows indicate some of the circular side-holes that are present along the stent.

A study by Keeley et al. [25] revealed that over 80% of stent placements are associated with pain and reduced patients' quality of life. Some of the key complications and side effects associated with ureteral stenting are reported below, and grouped based on the corresponding physical, chemical or biological determinants:

- Hydrodynamic effects, including urine backflow and inhibition of the peristaltic activity of the ureter [26-28];
- Complications associated with the procedure of stent placement, including stone passage [26, 29, 30], ureter or bladder irritation [31], and ureteric wall thickening [32];
- Migration of the stent from its primary position [33], with associated loss of function;
- Haematuria, abdominal and intestinal pain [32];
- Compromised stent functionality due to microbiological or physico-chemical factors. These include (i) bacterial colonisation over the stent surface, which can yield to biofilm formation [34], and (ii) formation and deposition of encrustation over the stent surface [35-39].

Formation of encrustation and biofilms over the stent surface (see Figure 1-4 and Figure 1-5) is recognised as one of the primary causes of stent failure [32], with incidence rates of 58% and 28%,

respectively [40]. Encrustation can compromise urine drainage through the stent, for instance by occluding functional segments or components of the stent, such as side-holes [41]. This can result in increased renal pelvic pressure, and potentially lead to severe complications. In these cases, surgical re-intervention or pharmaceutical treatment are often required, which have a significant impact on treatment costs and patients' quality of life [42]. Only in 2012 in Thailand, the cost of ureteral stenting for healthcare providers was within the range of ~$9K to ~$12K USD per intervention. Costs increased in the case of patients with urinary tract infection (UTI), within the range of ~$13K to ~$16K [43]. In 2013, in the USA, the total cost of a stent placement procedure was within the range of ~4K to ~$6K [44].

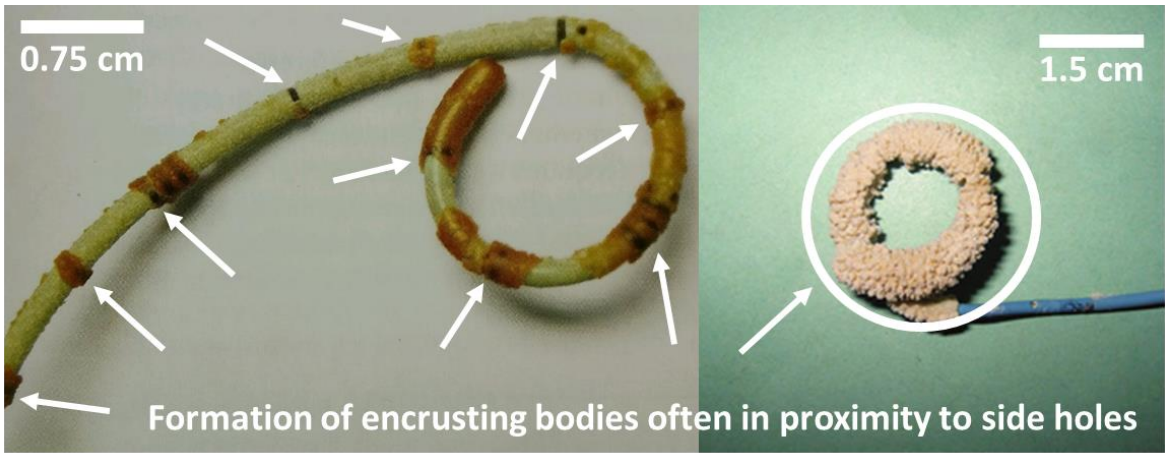

Figure 1-4 (left) Photograph of a ureteric stent retrieved from patients after 12 weeks. White arrows show the location of side-holes, and the formation of encrustation (orange colour) within the holes or in their vicinity. (Right) The J-ends of the stent are regions often prone to encrustation. Images are taken from [45], with minor modifications. Stents have approximate dimensions of 1.5 mm × 2.5 mm (ID × OD).

In the last few years, several researchers and biomedical enterprises have attempted to reduce the extent of encrustation and biofilm formation in stents, by changing the constitutive material or developing surface coatings [46]. Although some of these developments were effective in reducing encrustation rates [47], encrustation is still largely recognised by clinicians as a major cause of stent failure and associated side effects on patients.

Importantly, there has been a limited body of work aimed at identifying the mechanisms of encrustation or biofilm formation in stents [26, 48-54], both in the short-term deployment (i.e. up to 12 weeks) (see Figure 1-4) and long-term deployment (up to 6 years) [55] (see Figure 1-5).

Earlier studies mostly focused on the physico-chemical or microbiological determinants of encrustation, with only limited attention devoted to flow processes.

This has limited our understanding of the primary determinants of encrustation, and particularly of their dependence or impact on urine drainage in the stented ureter [54]. A more pervasive understanding of these processes would potentially lead to the design of robust and effective technological solutions against stent encrustation [48, 49].

Figure 1-5 Photograph illustrating samples of encrusted ureteral stents retrieved after 6 years from an 88-year old patient. The red circles indicate complete blockage of side-holes after long-term stent deployment. The image has been taken from Gu *et al.* [55], with minor adaptations. Stents have approximate dimensions of 1.5 mm × 2.5 mm (ID × OD).

1.5 Modelling flow in the stented ureter

Few earlier studies have been performed with the aim of gaining a more pervasive understanding of the flow dynamics in the stented ureter. For instance, Choong *et al.* [54] developed a simplified artificial model of the urinary system (shown in Figure 1-6) replicating kidney, ureter, bladder and urethra. The model was employed to investigate bulk encrustation in stents, under dynamic flow conditions. In a more recent study, Clavica *et al.* [30] developed an artificial model of the ureter to investigate the effect of ureteric occlusions and stent placement on the renal pelvic pressure. Experiments and simulations were also performed to investigate the local flow features nearby a ureteric occlusion, revealing the presence of cavity flow (see Figure 1-7).

These studies provided an important contribution towards our understanding of the flow field in the stented ureter and of its potential role in stent encrustation. The developed models however, did not allow for monitoring of both flow and encrustation processes *in-situ*, thus limiting the ability to quantitatively correlate flow metrics with formation and growth of encrusting structures.

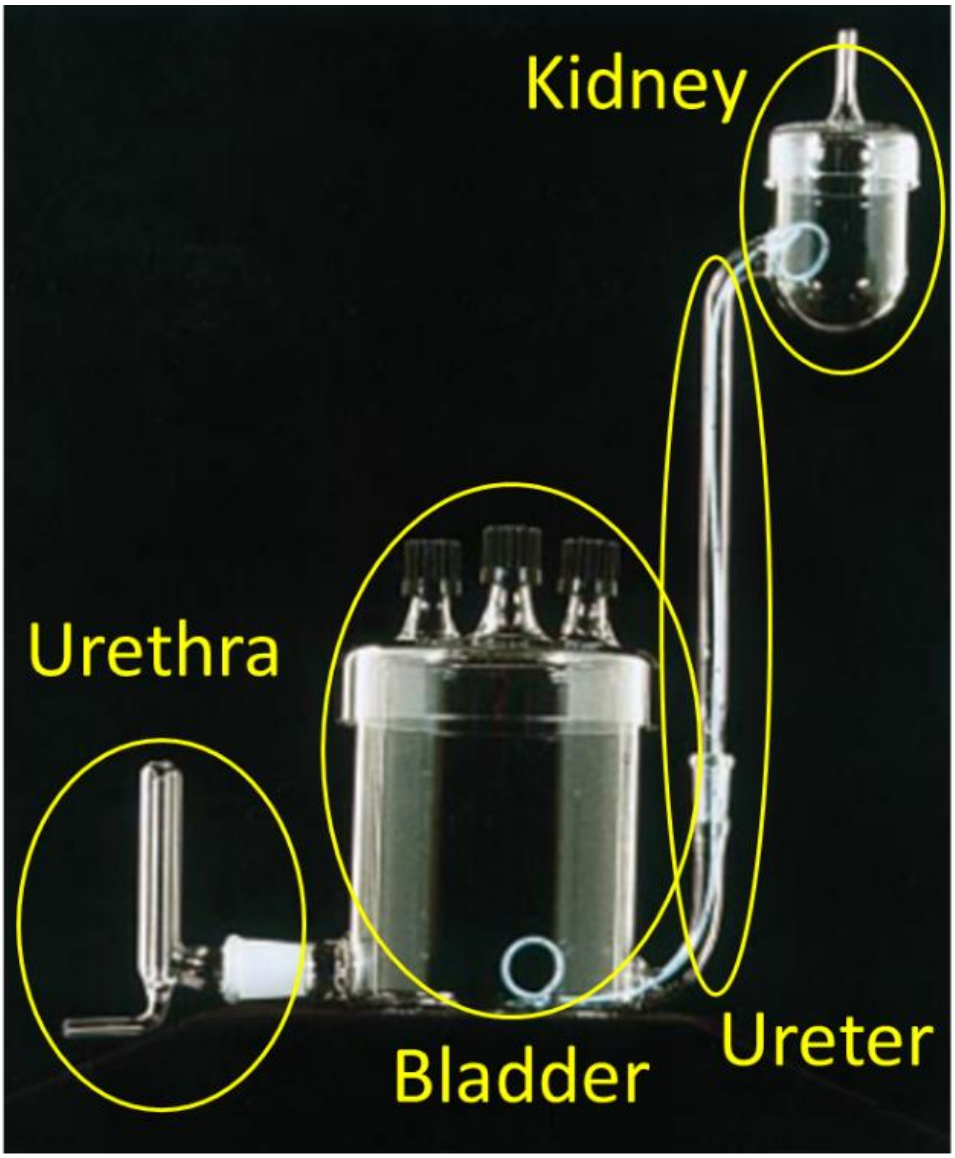

Figure 1-6 Artificial model of the urinary tract to study the effect of ureteral stenting on urine drainage. The top reservoir mimics a kidney that is connected to the bladder (bottom reservoir) by a rigid tube (replicating the ureter) (taken from [54] with minor adaptations).

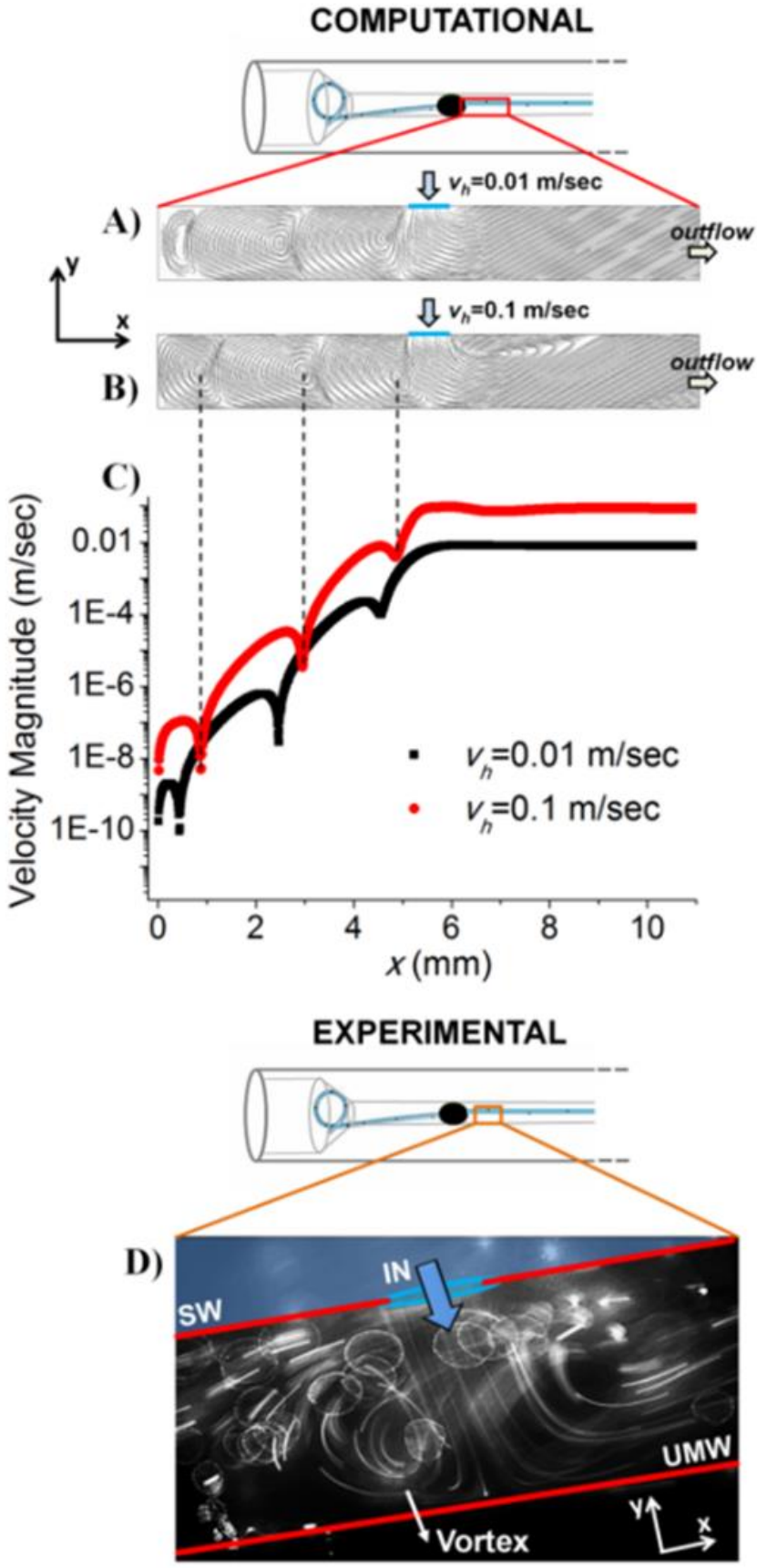

Figure 1-7 Numerical and experimental characterisation of the local fluid dynamic field in close proximity to a stent side-hole, showing formation of laminar vortices after the obstruction. The experimental and numerical investigation was performed using an

artificial model of a pig ureter. A-B) Fluid pathlines determined numerically, in a region of the Ureter Model (UM) located within the gap between the outer stent wall and the ureter model wall, distally to an obstruction of the ureter lumen. The mean velocity of the fluid exiting the first side-hole post-obstruction (v_h) was varied in these simulations; and results are reported for velocities of 0.01 m/sec (A) and 0.1 m/sec (B). C) Magnitude of fluid velocity along the centre line of the fluidic domain, for v_h = 0.01 m/s (black squares) and 0.1 m/s (red circles). D) Microscope image of fluorescent beads in a region of the fluidic domain located in close proximity to the first side-hole post-obstruction. Formation of laminar eddies can be appreciated. SW: Stent Wall; UMW: Ureter Model Wall. Image taken from [30].

Microfluidics has demonstrated to be a powerful tool for quantifying the transport of fluids and chemical species within confined and highly controlled fluidic domains. Coupling with analytical and optical instruments allows monitoring the spatiotemporal evolution of physico-chemical and biological processes at high resolution and sensitivity. Furthermore, the use of rapid prototyping microfabrication methods, together with the low priming volumes required, significantly reduce associated experimental costs [56-58].

Microfluidic technologies have been extensively applied to a variety of biological and biomedical problems. For instance, microfluidic platforms have been developed to replicate key physical and biological characteristics of physiological systems (from individual cells to organs), and employed as an investigational platform to evaluate the performance of numerous therapeutic techniques. One of such areas of application involves the modelling of segments of the human vasculature [59], vascular biological structures [60], human lungs [61], and other organs or tissues.

Recently, Clavica *et al.* [30] employed this technology to replicate the architecture of animal ureters, and to study the flow dynamics in the obstructed and stented ureter. This technological and modelling approach is developed further in this study, in order to allow for quantitative evaluation of flow and encrustation processes in stents.

1.6 Research Hypothesis

Despite significant efforts have been devoted to the bulk material and surface properties of ureteric stents, it appears as the flow performance of stents has not been designed or optimised (either theoretically or experimentally) in order to reduce encrustation rates. Designing for

material- and coating-independent stent architectures with improved flow dynamic performance would therefore represent a cost-effective route to increase the lifetime of ureteral stents, with potential for easier commercial translation and implementation within existing industrial processes.

Towards this end, a deeper understanding of the relationship between deposition rates and fluid dynamic processes in stents represents an important pre-requisite of this study. As for other bio-fluid dynamic phenomena [62-68], the underlying hypothesis of this study is that by increasing/decreasing the magnitude of wall shear stress acting over the stent surface, it is possible to decrease/increase the deposition and growth rate of encrusting particles, respectively. If verified, this principle can then be employed to inform the design of new stent architectures promoting increased levels of wall shear stress at regions of the stent suffering from encrustation.

1.7 Aim and Objectives

The main aim of this study is to develop a novel and simple-to-fabricate stent design that allows mitigating encrustation rates by altering the hydrodynamics of the stent-ureter system.

The following specific objectives have been undertaken in order to achieve the main aim of this study (the corresponding method's rationale is summarised in Figure 1-8):

- Identification, from previous studies and state-of-the-art developments, of the key determinants of ureteral stent encrustation, and the rationale behind previous and current technological solutions against encrustation (addressed in Chapter 2).
- Investigation of the relationship between fluid dynamics (and specifically wall shear stress) and deposition of encrusting particles in the stented and occluded ureter, and identification of critical hydrodynamic regions of the stent prone to encrustation. Towards this, microfluidic-based models (referred to as 'stent-on-chip' devices) will be designed and fabricated to mimic relevant hydrodynamic regions of a stented ureter, including intra- and extra-luminal compartments, drainage side-holes, and the cavity formed by a ureteric obstruction. Numerical simulations and experiments will be conducted to quantify relevant flow metrics and the growth of encrusting deposits, respectively, and a correlation between the two will be determined. This objective is addressed in Chapter 3.
- Full-scale 3D verification of the findings obtained using microfluidic-based models, particularly in terms of the location of critical regions of the stent prone to encrustation. As for the

microfluidic investigations, both experiments and simulations will be performed using full-scale artificial models of the urinary system. This objective is addressed in the Chapter 4.

- Design and verification of novel stent architectures capable of reducing encrustation rates. Based on the findings reported in Chapters 3&4, stent-on-chip models will be employed as a platform to iterate changes to the stent architecture, and investigate their effect on the flow performance and thus the deposition of encrusting particles in stents. Changes will specifically target those critical hydrodynamic regions of the stent identified in Chapter 3, and will be limited to those that are easy-to-implement within current industrial constraints. An optimal stent architecture will be identified, and both experiments and numerical simulations will be performed to compare the standard (commercial) design *vs.* new prototypes. This objective is addressed in Chapter 5.

- Design and characterisation of a manufacturing method for the fabrication of a full-scale prototype of a novel ureteric stent, which contains some of the optimised geometrical features identified in Chapter 5. This objective is addressed in Chapter 6.

Optimisation of the design of medical devices has often been performed using experimental design approaches, such as those based on the Design of Experiment (DoE) theory [69-71]. These approaches have proven to be particularly efficient when dealing with a large parametric space, as they provide a systematic determination of the relationship between multiple design variables (input variables) and performance indicators (output or response variables).

A different design approach was employed in this study, which is based on the evaluation of discrete values of relevant design parameters, at increasing dimensional scales (from microfluidic to full-scale models). Values of design parameters for stents were selected within a range that is compatible with manufacturing constraints. A schematic of the design method adopted in this study is reported in Figure 1-8. Microfluidic-based models were first employed to identify regions of the stent suffering from particle deposition, and to evaluate the effect of changing the geometrical characteristics of these regions. Microfluidic-based observations were then verified at a larger dimensional scale, using full-scale models of the stented ureter. Upon verification, the best performing stent architecture was manufactured to generate a full-scale stent prototype.

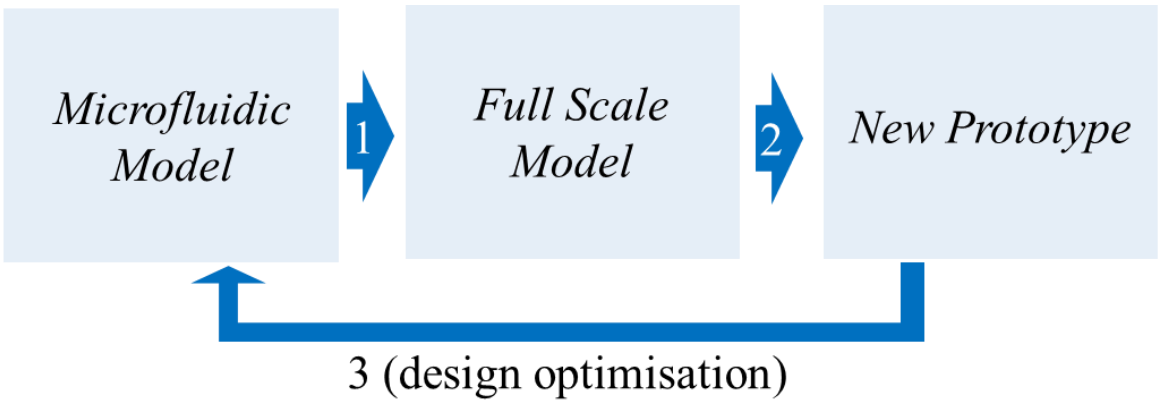

Figure 1-8. Flow chart outlining the method's rationale followed in the present study. It comprises a 3-step design optimisation approach, involving microfluidic and full-scale models, to generate a novel stent prototype capable of reducing encrustation rates.

1.8 Novelty

The work presented in this thesis contains several aspects of novelty, including:

- A microfluidic device replicating relevant hydrodynamic regions of a stented and occluded ureter has been developed. The device allows for *in situ* monitoring of transport phenomena involving fluid and chemical species, which are relevant to urine flow in the stented ureter.
- A systematic, experimental and computational characterisation of the fluid dynamic field within 2D and 3D models of the occluded and stented ureter has been performed.
- A quantitative correlation between wall shear stress and the growth of encrusting deposits in stents has been determined, and critical regions of the stent which are more susceptible to encrustation have been identified.
- A systematic study of the effect of changing some architectural features of the stent on the formation/growth of encrusting deposits has been performed, leading to the identification and design of a novel stent architecture capable of reducing encrustation rates.
- A full-scale prototype of a novel stent design has been fabricated, and a novel fabrication method suitable for generating triangular side-holes in stents has been developed.

Chapter 2 Literature Review

2.1 Outline

There are three technological parameters that play a key role on the performance of an ideal stent. These are its material, design and surface coating. This chapter highlights some fundamental developments that took place in these three areas of stent's technology, in order to contribute to the identification of an ideal stent. In addition to technological developments concerning stent's material, design and surface coating, the flow dynamic performance of stents has recently attracted increasing attention. Notably, it has been postulated that the local flow field in a stent is correlated with the deposition of crystals and microorganisms. These findings could potentially revolutionise future stent's designs, and complement developments made on materials and coatings. The most relevant changes in materials, designs and surface coatings of ureteric stents are reviewed in this chapter. These are described in the context of a specific cause of stent's failure they aim to address, with a particular focus on encrustation and biofilm formation.

2.2 Introduction

As introduced in Chapter 1, ureteral stents have been widely utilised in the last few decades as a measure for achieving temporary or permanent drainage in the occluded upper urinary tract. The underlying rationale is to allow the urinary flow to bypass intrinsic or extrinsic obstructions, which impair its drainage.

Nonetheless, there are few side effects associated with stents that complicate their use and management, particularly when deployed as a long-term treatment option. Bacterial colonisation and encrustation [72-74] over the stent surface are two of the most common causes of stent-related infections and obstruction, potentially resulting in its functional failure. Given that these issues profoundly affect the therapeutic outcome, patient's quality of life and associated costs for healthcare providers, further efforts should be put in place to address them effectively [75-80].

2.3 Materials and Methods

In this chapter, the main functional properties of stents are reviewed, including their architecture, operating principle, constitutive material, and surface coating. Side effects and complications

associated with ureteral stenting are subsequently discussed, with particular emphasis on particle deposition (i.e., as a leading cause of encrustation and biofilm formation).

In order to identify publications relevant to ureteral stent development, PubMed search from 1970 to 2017 was conducted. The keywords more extensively used for the search were “ureteral stents”, “stent encrustation”, “stent biofilm”, “stent bacterial colonisation”, “stent design”, “stent material”, “stent coating” and “UTI”.

2.4 Historical Perspective

According to Bareeq *et al*. [81] the history of ureteral stents goes back to ancient Egypt. The first procedure of ureteral catheterization, which involved insertion of a tube inside the urinary system *via* open bladder surgery, was performed by Gustav Simon in 1900 [82]. The first ureteral stent with an architecture comparable to the ones currently used was introduced by Joaquin Albarrano in the early 1900s [81]. Since then, technological advancements have had a significant impact on the design and material properties of stents. Each of these developments aimed to address a specific failure or cause of morbidity. They are discussed in the following pargraphs, together with the issues they attempted to resolve.

2.5 Constitutive Materials

Over the last few years, engineers and scientists have worked on identifying optimal constitutive materials for ureteral stents, focusing specifically on mechanical strength, flexibility, biocompatibility, surface roughness, and cost-effectiveness.

There are two main types of biocompatible materials [83-85] that are generally used for fabricating ureteral stents: polymers and metals.

The first ureteral stents were constituted of polyethylene, a synthetic polymer [86]. However, rigidity and tendency to break limited their usage in the clinical setting. To overcome these limitations, Gorman *et al*. [87] introduced a mixture of polyethylene and polyurethane as a more resistant material option against encrustation.

Silicone is widely employed for manufacturing ureteral stents, thanks to its flexibility against bending and lubricious properties. However, the rigidity of this material can potentially become a disadvantage during the insertion of the stent within a guidewire [88, 89].

Different polymeric materials also present a variable tendency to encrustation. A study performed by Tunney *et al*. [88] compared stents made of five different polymeric materials against

encrustation, over a period of 14 weeks of suspension in an artificial urine. Notably, due to its smoother surface, silicone appeared to have the best performance in the long term, showing 30% less encrustation at 10 weeks. Moreover, this study demonstrated that silicone was the least prone to calcium deposition [88].

Limited work has been conducted to test the effect of constitutive materials on the mechanical strength of the stent. For instance, Hendlin *et al*. investigated the strength and rigidity of 12 commercially available stents, before and after exposure to artificial urine (30 days) in static conditions [90]. They evaluated coil strength (defined as the maximal force required to pull the proximal coil through an artificial tissue) and rigidity (Young's modulus). The stiffest and softest stents were Cook® C-Flex (a copolymer from silicone family) and Cook® Black Silicone, respectively. Moreover, Applied Vertex® and Cook® Endo-Soft AQ had the highest and lowest coil strength, respectively.

Christman *et al*. [91] also compared the radial compression of different stents and concluded that wire reinforced stents, such as resonant stents, can withstand greater compression (i.e., such as the one caused by malignant urinary tract compression), without a significant reduction of the stent's inner lumen.

There have been few studies evaluating the effect of stent's rigidity on patients' quality of life. Some of these studies, such as those by Bregg *et al*. [92], Pryor *et al*. [93] and Joshi *et al*. [94], have demonstrated almost no correlation between patients' quality of life and the material composition of the stent. On the other hand, a study by Lennon *et al*. [95] on 155 patients revealed that the softness of the stent has a direct influence on patients' tolerability, and that softer materials were associated with higher incidence of dysuria and pain [96, 97].

Metallic stents were introduced by Gort *et al*. [98]. Their purpose was to reduce stent associated morbidity, and increase their ability to oppose deformation caused by extrinsic/intrinsic ureteric obstruction. However, in an *in-vivo* study on 50 patients by Liatsikos *et al* in 2009, metallic stents (specifically Resonant® metallic stent by Cook® medical) suffered from encrustation, as observed upon removal, and therefore did not provide a significant reduction in encrustation rates [99].

Kirby *et al*. performed a study on 30 patients to examine the performance of a titanium stent as a treatment modality for bladder blockade due to benign prostatic hyperplasia (BPH) [100]. Their results showed effective urinary flow re-establishment in 25 patients. In another study, Song *et al*. employed an expandable stent made by Nitinol (nickel-titanium) with the purpose of managing urethral strictures [101], and the result demonstrated the viability of nitinol stent in urethral strictures' treatment.

The current metallic stents are made of nickel/titanium mixed alloys. These materials have a specific memory that allows them to soften at temperatures below 7-13°C, and retrieve their shape upon increasing the temperature above 55°C. This property is highly advantageous in the process of stent deployment and removal [102].

2.6 Stent Design

'Double-J' refers to the most common type of stent design that was initially introduced by Finney in 1978 [103]. As described in Chapter 1, the term 'double-J' refers to the 'J' shape of each end of the stent, which is designed to anchor the stent and prevent its displacement. Since then, different biomedical companies have fabricated stents that have different architectures with the main aim of decreasing the impact of encrustation and infection, as well as improving urine drainage and lessen the impact on patients' quality of life. Some of the most commonly used designs are reported and discussed in the following paragraphs [81, 104].

Grooved stents***,*** having external grooves along the stent lumen, were introduced by Finney in 1981 [105] (see Figure 2-1). This design was developed specifically as a post-lithotripsy treatment option, in order to improve the stone clearance by introducing multiple pathways for urine drainage [106]. Grooved stents have been manufactured by Olympus® (USA) under the name of LithoStent™.

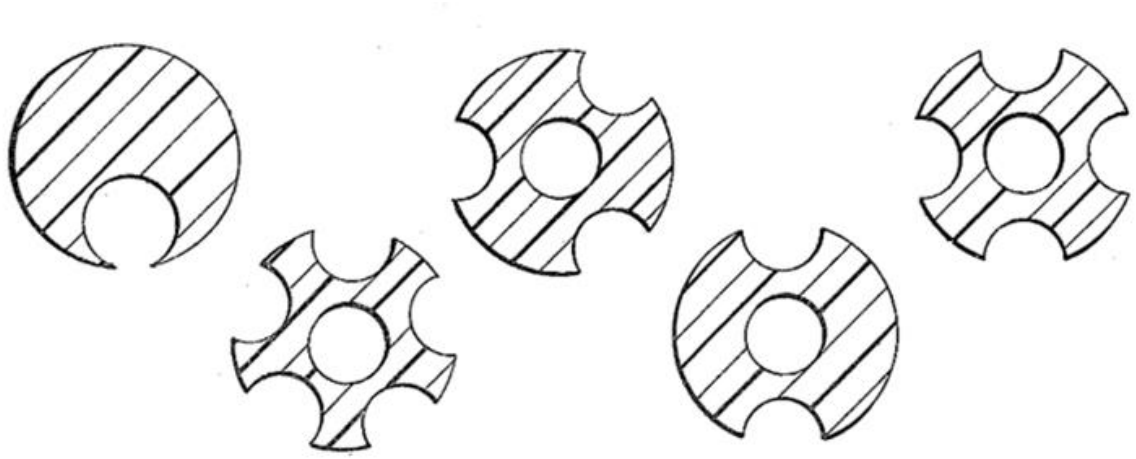

Figure 2-1 Grooved ureteral stent patented by Finney. The figure shows different types of grooves along the cross section of the stent (taken from [105]).

Spiral stents were initially introduced by Anderson *et al*. in 1987 [107] (see Figure 2-2). This design had a metal wire within the stent to maintain it into a spiral shape, and was believed to improve

urine drainage in case of extrinsic blockage, by providing a stable and durable opening of the ureteric lumen. In 2000, Stoller *et al*. employed the spiral design to evaluate urine flow in an *in vitro* model. Results from this study demonstrated increased flow in the model using a spiral stent as opposed to the traditional design (Double-J stent with straight lumen) [108]. The spiral shape was then improved to the next generation called *spiral-cut*, where the stent itself looked like a tube while its wall had a spiral cut. An *in-vivo* study on 12 swines performed by Mucksavage *et al*., however, found no statistically significant difference between spiral-cut and other stent models, in terms of encrustation rate, infection or stent migration. The spiral design demonstrated superior ability to conform to the ureter shape [109]. Percuflex Helical™ (Boston® scientific, USA) represents a commercially available spiral stent model.

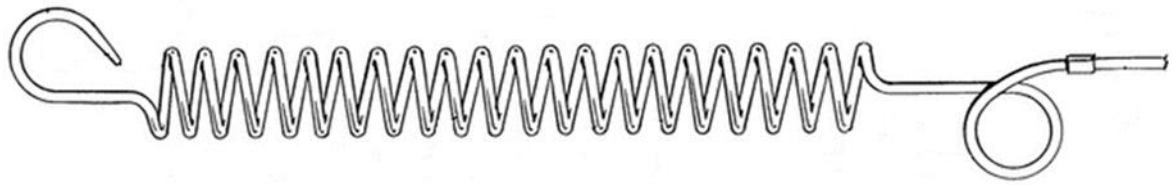

Figure 2-2 Spiral ureteral stent patented by Anderson et al. with hook shapes at both proximal and distal ends for preventing stent migration (taken from [107]).

Self-expanding meshed ureteral stents were developed with the aim of decreasing the irritation of the urinary tract and increasing urine flow within the stent, by taking advantage of the meshed structure (see Figure 2-3) to reduce the likelihood of clogging [97, 110]. A few studies assessed the performance of this design. For instance, the work of Olweny *et al.* revealed increased flow through the stent in comparison to traditional stents, which also reduced reflux towards upper tract and flank pain [111].

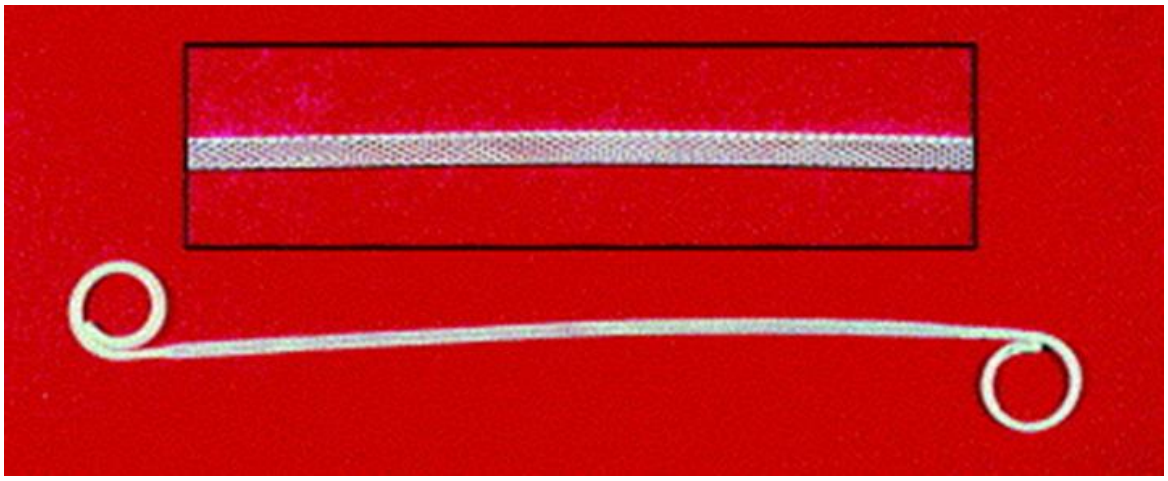

Figure 2-3 Metallic self-expandable mesh stent. A magnified view of the expanded stent is shown in the inset (taken from [111]).

Other advantages associated with meshed stents are their limited influence on the mechanical properties (i.e., distensibility) of the ureter, and potential for elution of bioactive compounds using the mesh structure as a drug reservoir [112]. Drug-eluting mesh stents have been reported, i.e. for delivery of anticancer drugs (Paclitaxel) [113] or anti-inflammatory agents. Examples of this application can be found in the work of Lugmayr and Pauer (1992), Barbalias, Siablis *et al*. (1997), Burt and Hunter (2006), and Wang and Burgess (2010) [114-116].

Despite the aforementioned advantages, mesh stents suffer from complex insertion procedures [111] and higher cost [81].

Tail stents are very similar to the traditional double-J stent. The main architectural difference is at the distal end of the stent, where there are loops of polymer instead of the classical pigtail (see Figure 2-4). The rationale behind this design was to decrease the bladder irritation that the standard stents caused. A randomized study on 60 patients performed by Dunn *et al.* revealed lower levels of irritation and obstructive urinary symptoms by using this stent compared to a traditional pigtail stent. However, incidence of flank or renal symptoms did not show a significant difference between the two types of stent [117]. Yew *et al.* [118] demonstrated that stent insertion and removal caused minimal pain on patients treated with tail stent. Companies have employed different materials in manufacturing tail stents, with the aim of improving patients' acceptability and comfort [119]. However, the work of Davenport *et al*. [25] using two different stent models, namely Inlay® (Bard® medical, USA) and Polaris™ (Boston® scientific, USA), demonstrated that there was no significant difference using either of these stents in 98 patients.

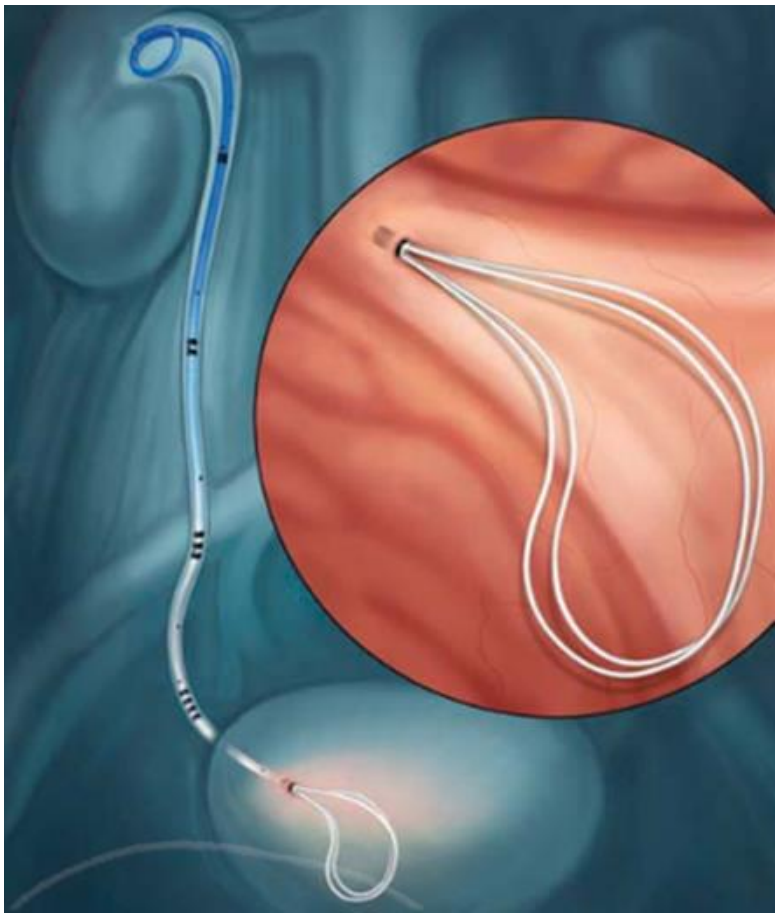

Figure 2-4 Tail stent fabricated by Boston® scientific, USA. The stent is characterised by two different designs at the proximal and distal ends. The proximal end (kidney) has a pigtail architecture, while the distal end (bladder) a loop tail shape (taken from [120]).

Dual-durometer stents have a similar architecture to that of tail stents. The main difference is in the mechanical properties of the stent body, which transitions from harder at the proximal end (kidney) to softer at the distal end (bladder). This design was introduced with the purpose of decreasing irritation due to its soft composite tail and therefore increasing the tolerability of the stent [81]. Boston® Scientific (USA) has employed this architecture in the Percuflex® ureteral stent series.

Magnetic-tipped stent (see Figure 2-5) was first introduced by Maculuso *et al*. in 1989 [81, 104], and was developed mainly to decrease additional costs associated with stent removal. Based on a study by Netto *et al*. in 1997-2000, this design had the potential for decreasing removal-associated costs by over £1,000 per patient [121]. Taylor *et al*. presented a more recent version of

this design, that confirmed successful removal of the stent in 29 of 30 patients [122]. This type of stent design also does not require cystoscopy for stent removal.

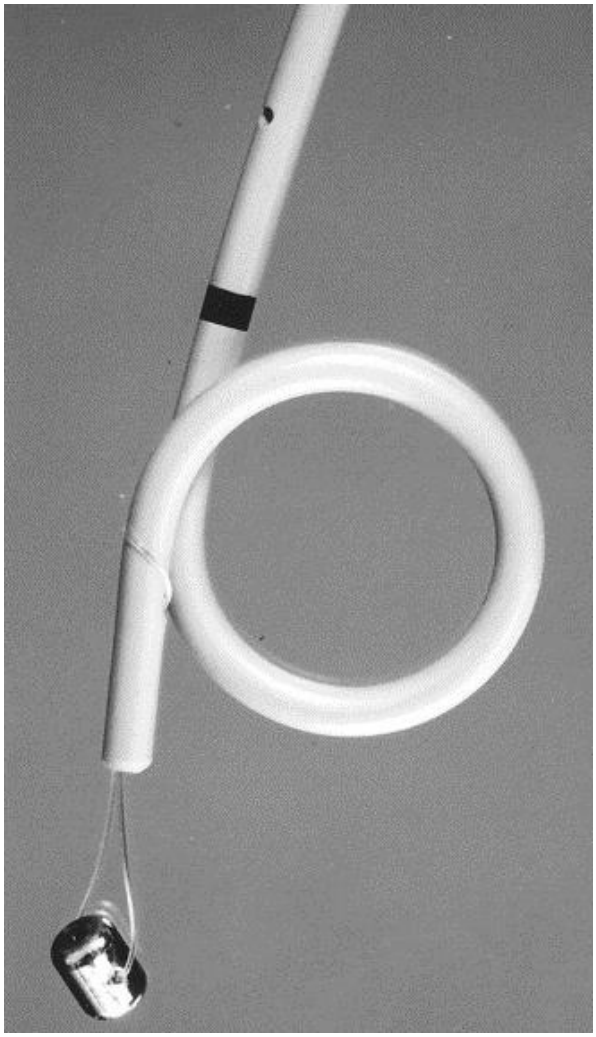

Figure 2-5 Distal end of a magnetic tipped ureteral stent. A magnet is connected to the distal end of the stent through a side-hole (taken from [122]).

Modifications of the previously discussed stent designs have led to other types of ureteral stents. One example is the so-called dual lumen stent, which has two drainage pathways to provide compensation in case of stent obstruction. This design was tested in an *ex-vivo* kidney model by J. Hafron *et al.* [123], who reported improved urine drainage over time compared to single lumen stents.

Another, more recent design is the resonance metallic stent [124] (see Figure 2-6), which consists of a compressed spring without side-holes, introduced by Cook© Medical with the aim of indwelling stents lasting up to 12 months or longer. Although the upfront cost of this stent is

higher compared to polymeric stents, the overall economic impact becomes less significant considering that polymeric stents often require removal and replacement. Moreover, initial tests performed by Wah *et al*. [125] on 15 patients showed improved urine drainage in comparison to traditional double-J ureteral stents, over a period of one year.

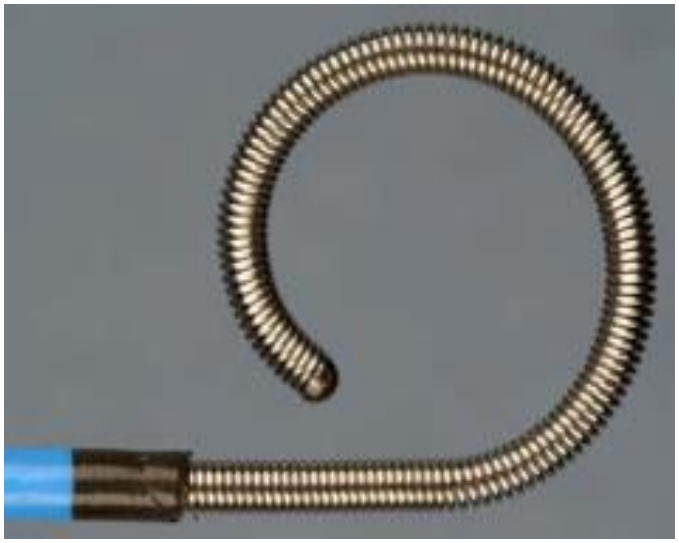

Figure 2-6 Resonance stent (produced by Cook© Medical) and its introducer sheet, which is used for placing the stent inside the urinary tract (taken from [125]).

2.7 Complications and side effects associated with ureteral stenting

Placement of ureteral stent sometimes lead to localised inflammation, which can cause haematuria and bladder pain. Elevated bladder pressure can potentially cause pain due to urine reflux towards the kidney. Abdominal and intestinal pain may be associated with these undesired side effects [32, 126]. Insertion of a stent can also cause stone retropulsion towards the kidney [29, 30, 108]. It has also been demonstrated that ureteral stents have a direct effect on ureteral peristalsis, which in turn impacts on urine flow and kidney pressure, thereby increasing patients' discomfort during urination. Reduced ureteric peristalsis has also been shown to cause renal pelvis inflammation [28, 108, 127, 128]. Bladder irritation has been associated with stenting, and may cause urinary urgency and other urinary symptoms [129, 130].

Stent migration from its primary site is recognised to be another major complication. However, its occurrence has been significantly reduced since the introduction of 'J ends' (or pigtail ends), which have an anchoring effect minimising stent's displacement over time. In addition,

polyurethane is recognised to have better shape memory (and thus to more effectively conform to the urinary tract) compared to silicone, reducing the likelihood of ureteral stent migration along the urinary tract. On the other hand, stents made by softer materials have been found to be more prone to migration [32, 131-133].

Since ureteral stents are foreign to the urinary system, their surfaces create an environment for colonisation by bacteria that may potentially form biofilms. This complication could lead to premature removal or replacement of the ureteral stent. For example, in a study performed by Paick *et al*. [134] using Percuflex® (Boston® Scientific, USA) stents, bacterial colonisation occurred in about half of 52 patients, after 2 weeks from stent insertion.

Encrustation is another complication that may affect indwelling of ureteral stents. It occurs in association with the presence of bacteria (such as *Proteus mirabilis*), which are known to produce urease. These bacteria cause an increase of urine pH, leading to crystals' formation [135, 136]. There are different factors that could affect stent encrustation, such as urine composition and pH, stent's material and surface properties, stent dwell time and urine flow dynamics [132]. These problems are discussed further in the following sections.

2.8 Current approaches to minimise encrustation and biofilm formation

Different stent material can cause variable levels of encrustations. Some of the common metallic alloys that have been used for producing ureteral stents (i.e., nitinol, superalloy titanium, and chromium cobalt) have shown different tendency to encrustations [137, 138]. A study by Tunney *et al*. [88] demonstrated that silicon and polyurethane had higher resistance to encrustation compared to other materials, after two weeks of stent insertion. At 10 weeks from insertion, silicon started to show superior performance than polyurethane.

Coating of the stent surface has been explored as a modality to decrease or ideally impede encrustation or biofilm formation over the stent surface [139]. This provides a convenient route for the industry, which may enable the use of conventional materials for constructing the stent body, followed by coating of their surface [104].

For instance, some of the coatings employed on polymeric stents increases surface smoothness, improve biological tolerability, and lower encrustation over longer time periods (up to one year) [140]. As an example, glycosaminoglycans (CAGs) [141, 142] - that are a component of urine - are employed as natural coating to prevent encrustation [143]. Heparin, a highly sulfated member of CAGs family and a blood thinner, has demonstrated potential for delaying surface encrustation for up to 12 months in a study performed on patients by Cauda *et al* [144]. Watterson *et al*.

employed stents coated with oxalate-degrading enzymes and showed reduced stent encrustation in 40 New Zealand white rabbits [145].

Diamond-like carbon (DLC) have also been used for coating stents, because of their physical and chemical properties [146]. Laube *et al*. perfomed a study on 10 patients (average duration of 14 weeks) and demonstrated the capability of DLC coating in reducing rates of encrustation and biofilm formation, resulting in improved stent's lifetime (see Figure 2-7) [147].

Figure 2-7 Cystoscopy results of (left) uncoated (at 45 days) and (right) carbon coated (at 90 days) samples. Images show the surface of the stent (taken from [147]).

Hydrogel coatings are used due to their hydrophilic porous structure that allows forming a thin hydrated layer over the stent surface. This layer was claimed to prevent biofilm growth, as it counteracts the formation of the conditioning layer that is often indicated as a primary cause of biofilm formation [136]. However a study performed by John *et al.* [148] showed that hydrogel coating on its own doesn't reduce bacterial adhesion, but instead performs better when it is combined with other chemicals, such as antibiotics. Their study included comparison of hydrogel-coated and uncoated stents dipped in antibiotic solutions, which were both suspended in *Escherichia coli* or *Enterococcus faecalis* solutions for 24 hours.

Phosphoryl-choline (PC), which is an essential component of erythrocytes aping lipid membrane, provides a hydrophilic environment that hosts water and protects the surface of the stent from proteins or other chemicals [41, 149]. The use of this coating has demonstrated a slight reduction in encrustation and biofilm formation, as shown by Stickler *et al*. in a clinical study on 44 patients over the period of 12 weeks [41]. Encrustation and biofilms were analysed using scanning electron microscopy in both coated and uncoated stents.

Antibiotic coating can either prevent growth of bacteria or kill them. It has been performed widely by either dipping the stent inside a solvent containing antibiotics and evaporating the solvent, or incorporating the antibiotics into biodegradable coatings for sustained release [150]. There are different types of antibiotics that have been used in stents, such as Daptomycin, Linezolid, Tigecycline, Rifampicin [151, 152], Temporin A, RNAIII-Inhibiting Peptide [153], Oxacillin, Cefotaxime, and Vancomycin [154]. Each of these were tested in different *in-vivo* and *in-vitro* models and demonstrated a reduction in bacterial growth. However, it has also been demonstrated that a combination of antibiotics often has a stronger effect against bacteria. For instance, Minardi *et al* [155] demonstrated such effect by deploying the combination of *tigecycline* and *rifampin* in 5 rat models against *Enterococcus faecalis*.

Polytetrafluoroethylene (PTFE), also known as Teflon™, is a material acknowledged for its low friction coefficient and resistance against Van der Waals forces, both factors that affects bacterial colonisation. This makes PTFE a promising candidate for stent's coating [156]. Chung *et al* [157] compared 14 PTFE coated *vs* uncoated metallic mesh stents in 7 dog models, over an average period of 15 weeks, and investigated the effectiveness of PTFE coating against tissue ingrowth, and found the coating to be effective against luminal occlusion caused by it.

Coating with antimicrobial agents is another strategy to reduce encrustation and/or biofilm formation. Two examples of such agents are Triclosan and Silver. A recent study on the use of Triclosan coating has been performed by Lange *et al* [158], comparing coated *vs* uncoated stents incubated in stationary conditions for 7-days. It confirmed the significant bacterial resistance of this agent. Despite offering resistance to biofilm formation, Triclosan did not get FDA (Food and Drug Administration) approval due to concerns over its potential for developing antibiotic resistance [150]. On the other hand, silver ions have shown to be capable of preventing bacterial replication [159], however their performance against biofilm formation in ureteral stents have been variable [153]. Additionally prolonged use of the coating could lead to argyria [150].

Chitosan is a non-toxic biopolymer that has also demonstrated potential for inhibiting bacterial growth. Its anti-biofilm properties are shown by Carlos *et al* [160], who tested this specific coating against bacteria over 54 hours, using a drip-flow biofilm reactor system. In another study Yang *et al* [161] combined chitosan and polyvinylalchohol (PVA) to successfully reduce the absorption of proteins and prevent bacterial growth in ureteral catheters made by segmented polyurethane in an static study.

2.9 The role of flow dynamics on stents' failure

It has been demonstrated that urine flow dynamics in a stented ureter has an important role in governing the formation and growth of encrusting particles and bacterial deposits. This relationship was investigated theoretically by Siggers *et al* [162] and Waters *et al* [163], suggesting a strong relation between the flow field and the transport of chemical species involved in crystals' formation. Using an artificial model of the stented ureter, Clavica *et al* observed the formation of vortices in the vicinity of a ureteric obstruction, which may trap particles suspended in the fluid promoting their deposition [164, 165]. The work reported in this thesis (particularly in Chapters 3, 4, and 5) demonstrates a direct correlation between accumulation of particles and wall shear stress in ureteric stents. These findings could open new avenues for improving the stent's design *via* fluid dynamic optimisation, potentially providing novel technological solutions that are complementary to existing materials and surface coatings.

2.10 Conclusion

Various advancements in materials, design and coating of ureteral stents have been discussed in this chapter and are summarised in Table 2-1. Each of these developments aims to address specific causes of stent's failure, especially encrustation and biofilm formation. Combining the most appropriate material, design and coating would thus allow the development of an optimal stent.

Currently, there is no ideal stent that does not experience encrustation. Different bulk materials and surface coatings have been investigated as a means to reduce encrustation rates in stents; however, this has not yet resulted in significantly improved clinical outcomes. Earlier studies have suggested that flow dynamics may also play a pivotal role in governing formation and deposition of encrusting particles. Earlier studies have however provided only a qualitative correlation between encrustation and flow processes in stents, which has hindered the design of stents with improved flow performance. Therefore, this correlation will be investigated quantitatively in the following chapter, utilising microfluidic-based models of the occluded and stented ureter.

Table 2-1 Different stent materials, designs and coatings with few key aspects of each and, where relevant (especially in the design section), an example of a commercial stent is provided

	The Change	*The Solution*	*Reference*
Material	Polyurethane	Better drainage efficiency compared to silicone	In-vitro model made by 9F polyvinyl tubing and ex-vivo model taken from a human cadaveric urinary system [166]
	Silicone	Better performance against encrustation compared to polyurethane	Ureteric stents were suspended for 15 weeks in Artificial Urine and the amount of encrustation was measured using Atomic Absorption Spectroscopy [88]
	C-Flex	A thermoplast polymer from the family of silicones. Its surface of friction was lower compared to polyurethane and PercuFlex™	Various stent materials' surface coefficient of friction were measured by Mardis et al [167]
	PercuFlex™	From the family of silicones. A biomaterial with a relatively long-term indwelling biodurability compared to polyurethane and silicone itself.	
	Titanium	Improvement in Begign Prostatic Hyperplasia in over 80% of patients	The performance of titanium stent was investigated on 30 patients in a study carried out by Kirby *et al* [100]

	Nitinol	A mixture of nickel and titanium that softens at temperatures below 10°C and hardens as the temperature increases and allows better stent insertion and removal	The performance of 22 nitinol stents was tested in 12 male patients between 19-67 years old [101]
	Stainless Steel	Does not have major insertion side effects and recognised as an operational tool in tumour associated hydronephrosis	23 patients (29 to 78 years old) with hydronephrosis being the main pathology [168]
	The Change	*The Solution*	*Reference*
Design	Grooves	Providing multiple pathways for urine drainage	LithoStent™ (Olympus®, USA)
	Spiral	Providing a stable and durable lumen	Percuflex Helical™ (Boston® scientific, USA)
	Self-expanding	Providing a wider pathway for urine compared to conventional stents	UVENTA™(TaeWoong ®, South Korea)
	Tail	Provides less bladder irritation compared to the conventional stents	Inlay® (Bard® medical, USA) and Polaris™ (Boston® scientific, USA)
	Dual-durometer	Provides less bladder irritation compared to conventional stents and better stability in the kidney	Percuflex® (Boston® scientific, USA)
	Magnetic-tipped	Provides an improvement towards stent removal and avoiding the use of cystoscopy	Magnetic Black-Star (Urovision, Germany)
	Resonant	Provides up to 12 months indwelling	Resonant ® (Cook® medical, USA)

	The Change	*The Solution*	*Reference*
Coating	CAGs and heparin	A natural component of urine that could potentially delay encrustation for up to 12 months	40 rabbits were tested over a 30 days period and encrustation was measured using Atomic Absorption Spectroscopy [145]
	DLC	With physical and chemical composition reduceing encrustation and biofilm formation	10 patients were treated for a period of 14 weeks [147]
	Hydrogel	Preventing biofilm via creating a thin layer of water on the surface	Coated and uncoated stents were suspended in bacterial solvents for 24 hours [148]
	PC	A natural component that provides a hydrophilic environment on the surface and as a result reduces encrustation and biofilm formation	Coated and uncoated stents were tested on 44 patients for a period of 12 weeks [41]
	Antibiotic	Disrupts bacteria formation and growth	Studied on 5 rat models against *Enterococcus faecalis* [155]
	PTFE	Has a low friction coefficient and resistance against van der Waals forces that prevents bacterial colonisation	This was studied by comparing coated vs uncoated 14 metallic mesh stents in 7 dog models for a period of 15 weeks [157]

Antimicrobial Triclosan and Silver	Triclosan has a significant bacterial resistance however it is not approved by FDA, because of concerns over antimicrobial resistance. Despite resistance against biofilms, a prolong use could lead to argyria.	Coated and uncoated stents were investigated for a period of 7 days in an stationary study [158]
Chitosan	It inhibits biofilm formation on the stent surface	Coated surface was exposed to different bacteria through a drip-flow biofilm reactor system for a period 54 hours [161]

Chapter 3 Particle accumulation in ureteric stents is governed by fluid dynamics: *in-vitro* study using a 'stent-on-chip' model

3.1 Outline

The objective of this chapter is to investigate the correlation between fluid dynamic processes and deposition of encrusting particles in ureteric stents. Microfluidic models (referred to as 'stent-on-chip' or SoC) were developed to replicate relevant hydrodynamic regions of a stented ureter, including drainage holes and the cavity formed by a ureteric obstruction. Computational fluid dynamic (CFD) simulations were performed to determine the wall shear stress (WSS) field over the solid surfaces of the model, and the computational flow field was validated experimentally. Artificial urine was conveyed through the SoCs to measure the temporal evolution of encrustation *via* optical microscopy. It was revealed that drainage holes located well downstream of the obstruction had almost stagnant flow and low WSS (average 0.01 Pa, at 1 mL/min), and thus suffered from higher encrustation rates. On the contrary, higher levels of WSS in holes proximal to the obstruction (average ~0.04 Pa, at 1 mL/min) resulted in lower encrustation rates in these regions. The cavity located nearby the obstruction was characterised by high levels of encrustation, due to the low WSS (average 1.6×10^{-4} Pa, at 1 mL/min) and the presence of flow vortices. Increasing the drainage flow rate from 1 to 10 mL/min resulted in ~1-order of magnitude lower encrustation. The present study thus demonstrated an inverse correlation between deposition of encrusting bodies and the local WSS in a stented ureter model. Critical regions with low WSS and susceptible to encrustation were identified, including 'inactive' side-holes (i.e., with minimal or absent flow exchange between stent and ureter) and the cavity formed by a ureteric occlusion. These findings can open new avenues for improving the stent's design *via* fluid dynamic optimisation.

3.2 Introduction

Ureteric stents are one of the most commonly used urological tools to provide urine drainage when this is impaired or blocked by obstructions, such as ureteral stones or tumors [46, 169, 170].

Since the introduction of the double-pigtail ureteric stent by Finney in 1978 [103], the stenting technology has undergone several developments [171]. However, stents still suffer from failures,

and the associated morbidities and complications significantly affect a patient's quality of life and cause financial burden on national healthcare services [171]. Incidence of these failures depends on several factors including indwelling time, patients' fluid intake, urinary stasis for extrinsic compression, and access to healthcare. Encrustation and biofilm formation over the stent surface have been identified as primary determinants of stents' failure, with incidence rates of 58% and 28%, respectively [40]. As outlined in Chapter 2, whilst studies have been conducted to identify or develop materials and surface coatings inhibiting encrustation and bacterial adhesion, the dominant processes governing encrustation dynamics in ureteric stents are still not entirely clear [172]. Among these, fluid dynamic processes have been largely overlooked although few studies have suggested that they may play a significant role on the initiation and growth of encrustation [49].

The present study attempts to fill this knowledge gap. It is herein hypothesised that encrustation rates are strongly correlated with a specific flow metrics called *wall shear stress* (WSS). In particular, it is argued that low and high levels of WSS are correlated with high and low encrustation rates, respectively. To test this hypothesis, 'stent-on-chip' (SoC) models were developed and employed in order to generate flow fields that resemble, in some measure, those encountered in a 'stented ureteric system'. Artificial urine was run into the SoCs and encrustation deposits (mainly in the form of crystals) were monitored over time. A computational fluid dynamic (CFD) model replicating the experiments was then implemented to compute WSS, so that it was possible to spatially correlate wall shear stress with the experimentally-observed encrustation maps, thus allowing the identification of regions prone to encrustation.

3.3 Materials and Methods

3.3.1 'Stent-on-chip' models: design rationale

SoC models were designed to replicate relevant flow domains of a stented and occluded ureter, including (Figure 3-1):

(i) A large (1.5 mm wide) and a narrow (0.5 mm wide) channel, replicating the intra- and extra-luminal compartments of a ureteric stent, respectively. Channels were separated by a 0.5 mm thick septum, mimicking the stent's wall.

(ii) An obstruction (or cavity), replicating an occlusion of the ureter lumen caused by either a ureteral stone (intrinsic obstruction) or a tumour (extrinsic obstruction). A

proximal, complete occlusion of the ureter lumen was modelled (ureter diameter at the occlusion site = 2.5 mm) [30]. This specific flow domain will be identified as 'cavity' or 'occluded cavity' from herein. The obstruction was modelled following a similar approach to the one reported by Clavica et al. [30]; in their study, the extra-luminal region of the stent at the obstruction site was fully occluded, forcing the fluid to flow into the intra-luminal compartment. Moreover, the occlusion was positioned between two adjacent side-holes of the stent.

(iii) Two drainage holes (0.8 mm wide), proximal (Hole 1) and distal (Hole 2) to the obstruction.

The above dimensional characteristics of SoC models were defined to replicate those of commercial double-J stents (Cook® Medical, USA), as illustrated in Figure 3-1. Two cylindrical chambers (5 mm in diameter) were also designed to act as inlet and outlet reservoirs.

The total width and length of the model were defined to comply with dimensional constraints imposed by the typical size of microscope stages; thus, the SoC architecture was designed to fit on a 50 mm × 70 mm microscopic glass slide, enabling monitoring of flow and encrustation processes *in situ*. For this reason, only a limited segment of the stented ureter was modelled in this study, which replicated key hydrodynamic regions of the stented ureter system (as described above). Taking into account the distance between adjacent side-holes in a commercial double-J stent (Cook® Medical, USA), only two side-holes could be accommodated to fit within the SoC model length. Models with two different architectures were designed, to replicate areas proximal to the obstruction (referred to as 'occluded') and distal to the obstruction (referred to as 'unoccluded'), respectively.

There are many clinical and physiological variables that need to be considered when approaching the design of a model of the stented ureter. The following assumptions were made in this study:

- the patient, and thus the stent-ureter system, is lying horizontally;

- the stent is resting on one side of the ureter, resulting in only one gap (or extra-luminal compartment) between the stent and the ureter.

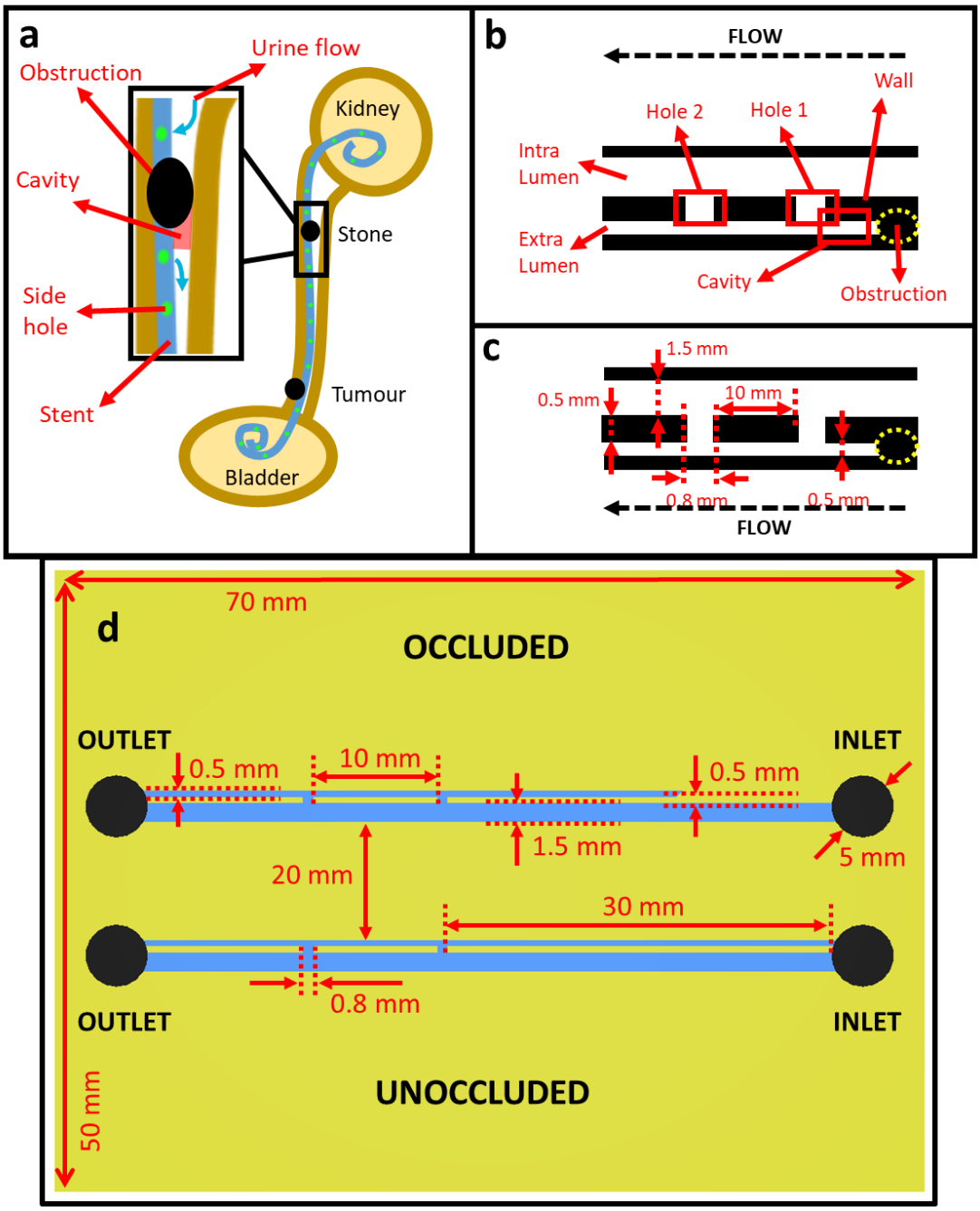

Figure 3-1 (a) Two-dimensional (2D) schematic of the urinary system, with a simplified representation of extrinsic (e.g. tumour) or intrinsic (e.g. stone) causes of ureteric obstruction. (b) Schematic representation of key hydrodynamic regions within a stented ureter, located in the vicinity of an obstruction. These include two drainage holes (Hole 1 and Hole 2), the intra- and extra-luminal compartments of the stent,

and the cavity formed by a complete obstruction of the ureter lumen. This is also highlighted in red in (a). Stent-on-chip models were designed to replicate these hydrodynamic regions. (c) Key geometrical properties of SoC models. The latter were taken from a commercial double-J stent (Cook® Medical, USA), which has an extended length of 40 cm, inner diameter of 1.5 mm, wall thickness of 0.5 mm, and side-hole diameter of 0.8 mm. (d) CAD drawing (top view) of the all model, with relevant dimensional properties, including both occluded and unoccluded SoCs.

Moreover, the length of the stent compartment at the inlet side of the device was defined to be greater than the entrance length (L_e), allowing the flow to fully develop before reaching side-hole 1. L_e was determined from $0.06 \times \mathrm{Re} \times D_h$, where D_h and Re correspond to the channel's hydraulic diameter and Reynolds number, respectively. The Reynolds number is defined as $\rho V D_h / \mu$, where ρ, μ, and V correspond to the fluid density, dynamic viscosity, and mean velocity, respectively. The mean velocity was determined from the ratio between the volumetric flow rate (Q) and the inlet channel's cross-sectional area. Values of inlet volumetric flow rate investigated in the present study were 1 mL/min and 10 mL/min, following a previous study by Tofft et al. [173].

Although these models fail to make an exact replica of a stented ureter, they do capture relevant flow features, including a laminar vortex in the cavity formed by the obstruction and the lateral drainage through side-holes (Figure 3-1b,c). Furthermore, they provide a hydrodynamically rich environment - particularly in terms of its WSS field - which includes both regions of low and high WSS. Thus, they represent a useful investigational tool that, while maintaining the essential flow features encountered in stented ureteric systems, also allows for high-resolution mapping of encrustation rates at key hydrodynamic regions of interest.

3.3.2 'Stent-on-chip' models: fabrication protocol

SoC models were fabricated using a cost-effective technique developed in-house, combining micromilling with replica moulding [174]. The fabrication process comprised the following steps (Figure 3-2): (i) computationally assisted design (CAD) of the model geometry using SolidWorks (Dassault Systèmes Solidworks Corp., France) (Figure 3-2a). (ii) Generation of a negative mould by micromilling of the model architecture onto a layer of poly (methyl methacrylate) (PMMA) (Figure 3-2b). (iii) Pouring of a liquid epoxy resin (yellow dual cartridge, RS Components Ltd., UK, at 1:1 weight ratio between components) on the negative mould. (iv) Curing of the epoxy layer at room temperature (~21 °C, for ~100 min), and removal from the PMMA negative mould (Figure 3-2c). This layer contained a positive replica of the SoC architecture (positive mould). (v) Pouring of

liquid poly (dimethylsiloxane) (PDMS, Sylgard® 184, Dow Corning Corporation, USA) over the positive mould. PDMS was produced at a curing agent: monomer ratio of 1:10 (by weight), degassed using a vacuum chamber, and then cured overnight at ambient temperature. (vi) Removal of the cured PDMS layer from the positive mould, and bonding to a 1 mm thick glass layer (Corning® microscope slides, Sigma Aldrich, UK) by plasma treatment (Tepla300, Oxford Instrument, UK). A photograph of a finished stent-on-chip model is illustrated in Figure 3-2d.

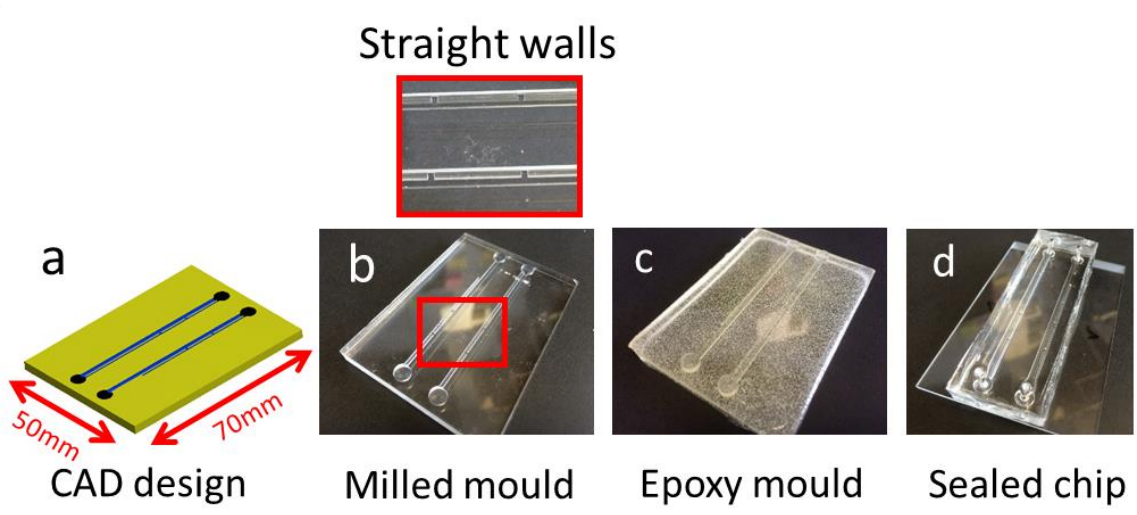

Figure 3-2 Combined micromilling-replica moulding process for fabricating SoC models. Images show (a) a CAD design of the device, with an inset to illustrate key dimensional properties of both occluded and unoccluded models; (b) the micromilled, PMMA-based negative mould (with a zoomed-in view of side-holes); (c) the epoxy-based positive mould casted from the micromilled mould; and (d) the PDMS channel architecture bonded to a glass slide, upon treatment with oxygen plasma.

3.3.3 Experimental characterisation of flow and encrustation processes

Flow visualisation experiments were performed to visualise the flow streamlines within the SoC models, and compare them with those calculated numerically. The experimental setup comprised a syringe pump (Harvard ®, apparatus pump33) loaded with a 50 mL plastic syringe (BD® Plastic). Polytetrafluoroethylene (PTFE) tubing (inner diameter: 1/32" and outer diameter: 1/16", Cole-Palmer®, UK) connected the syringe to the microfluidic device inlet, and the device outlet to a reservoir. The microfluidic device was placed horizontally on the stage of a fluorescent microscope equipped with laser illumination (Nikon ®, USA), for visualisation of fluorescent flow tracers. Tracers were 5.6 μm diameter polystyrene beads (at a concentration of 2×10^4 beads/mL) loaded with a fluorescent dye excitable at 633 nm and emitting at 680 nm. Images were acquired

using a CCD camera (ORCA-R2, Hamamatsu Photonics K.K., Japan), with an exposure time of 10 sec to reveal the flow streamlines. Experiments were performed at a fixed flow rate of 1 mL/min.

Experiments were also conducted to quantify the formation of encrusting deposits. A supersaturated artificial urine (AU) was employed to investigate deposition and growth of encrusting crystals, and each microfluidic device was only used once. The surrogate fluid was produced following a protocol designed by Keevil *et al.* [175], with minor modifications; related chemical constituents are reported in Table 3-1 and were purchased from Sigma Aldrich® (UK). The AU solution was prepared at 37ºC and under continuous stirring; it had a pH of 6.8, and was kept at 37ºC during experimentation.

Table 3-1 List of chemicals used for producing the artificial urine (AU), including corresponding molecular weight and concentration in the final AU solution. The chemical composition of the urine surrogate was taken from Keevil et al. [175], with minor modifications.

Component	*Molecular Weight*	*Concentration (mmol/L)*
Lactic acid	90.08	1.1
Citric acid	192.12	2
Sodium bicarbonate	84.01	25
Urea	60.06	170
Calcium chloride dihydrate	147.00	2.5
Sodium chloride	58.44	90
Magnesium sulphate heptahydrate	246.47	2
Sodium sulphate decahydrate	142.05	10
Potassium dihydrogen phosphate	136.09	7
Ammonium chloride	53.49	25

Experiments were performed at inlet flow rates of 1 mL/min and 10 mL/min [165, 173, 176], and five independent repeats were performed at each flow rate. In each experimental run, artificial urine was pumped using a peristaltic pump (MINIPULS3, Gilson, Inc., France) into the microfluidic device for 90 minutes. The device was placed horizontally on the stage of an inverted optical

microscope (Wilovert 30, Helmut Hund GmbH, Germany). Tubing (PTFE, Cole-Parmer®) connected the device to both the reservoir and the pump (see Figure 3-3), and microscope images at 4x magnification were acquired at intervals of 15 minutes, using a CCD camera (exposure time = 1 ms). Imaging was performed through the glass slide, and the optical focus was set at the bottom glass surface of the model. ImageJ software (NIH, USA) was employed to process the images and quantify the time evolution of encrustation at selected locations within the devices. The area used for the calculation of encrustation rate was 500 μm × 800 μm (height × width), and is identified in Figure 3-5c by red boxes. The image processing steps were as follows: (i) bright field images were converted to 8-bit format, and areas of interest within the image were manually selected (cropped). (ii) Images were thresholded in to a black-and-white binary image format, where values equal to 255 corresponded to encrusting deposits; and (iii) the percentage area occupied by encrustation was quantified. Values are reported as average ± standard deviation, and are compared for statistical significance.

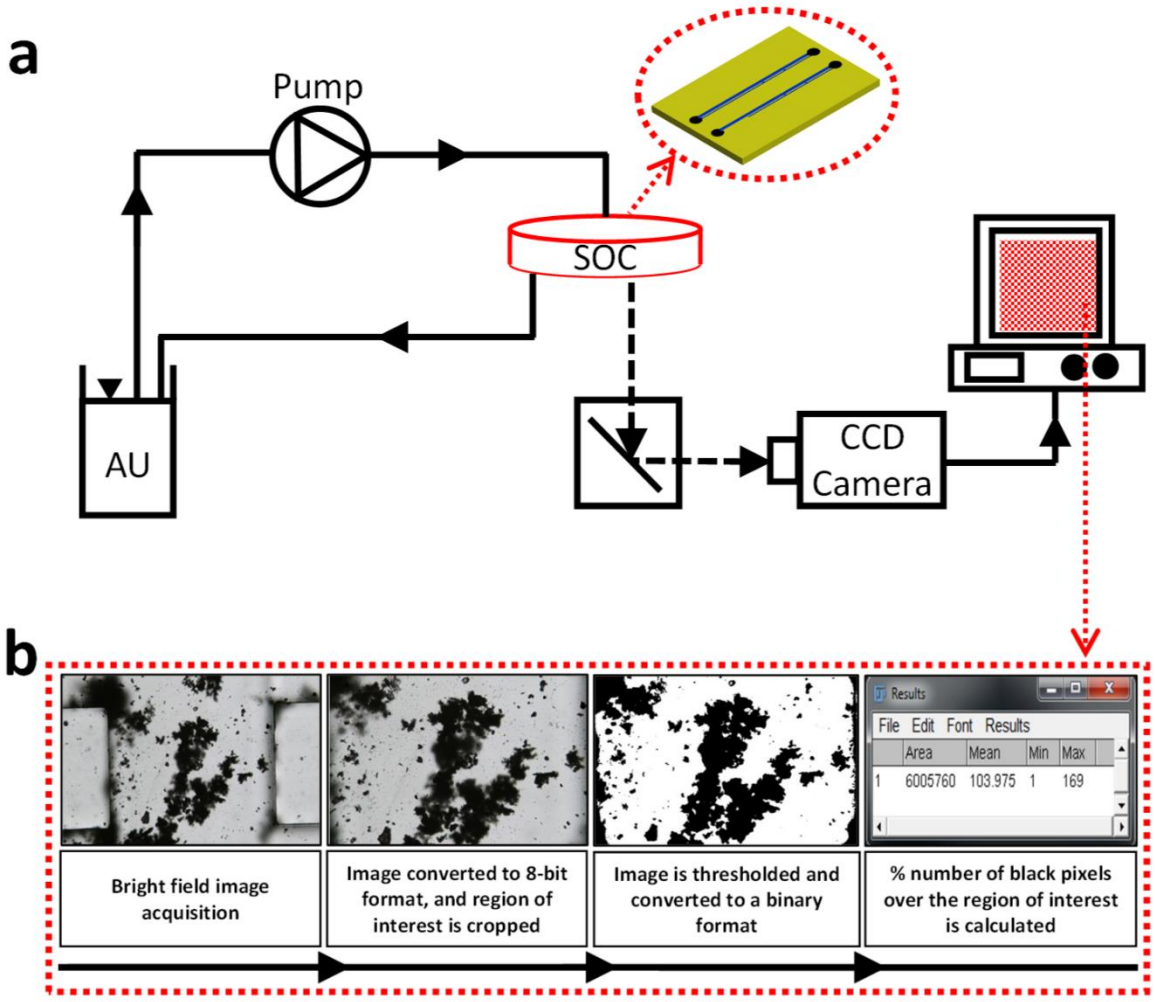

Figure 3-3 (a) Experimental setup employed for visualising encrustation in-situ. It comprised a reservoir containing artificial urine (AU), a peristaltic pump (Minipuls3, Gilson Inc.,

France), the SoC device placed on an inverted microscope stage (Wilovert 30, Helmut Hund GmbH, Germany) equipped with a 4x magnification lens and a CCD camera (GXCAM-HICHROME SII, GT-Vision Ltd., UK) connected to a PC for image acquisition. Imaging was performed through the glass layer of the device, and the optical focus was set at the bottom glass surface of the channel. (b) Flowchart outlining the image processing steps performed to quantify encrustation within selected regions of the SoC model. ImageJ software (NIH, USA) was employed for image processing. The image frames had a size of 1 mm X 1.4 mm.

3.3.4 Simulation of the flow field

Computational fluid dynamics (CFD) simulations were performed to characterise the flow field within SoC models and - most importantly - to determine flow metrics (in the form of wall shear stress contours) that complement the experimental particle deposition data. In this method, the governing equations describing the interaction of liquids with physical boundaries are solved computationally. In a first step, the device geometry was constructed using ICEM CFD 17.0 (Ansys Inc., USA). The volume occupied by the fluid was then discretised in finite volumes of tetrahedral shape. The number of mesh volumes (17,770,735) and their size (0.1 mm) were defined subject to a compromise between solution robustness and computational cost. In other words, the 0.1 mm size was defined after carrying out a mesh dependence study (see Figure 3-4). Ansys® Fluent 17.0 (Ansys Inc., USA) was subsequently employed to define the relevant physical models and boundary conditions, and to solve for mass and momentum conservation equations. A mass flow boundary condition was set at the model inlet, while atmospheric pressure was imposed at the outlet. A no-slip boundary condition was imposed at the ureter and stent walls.

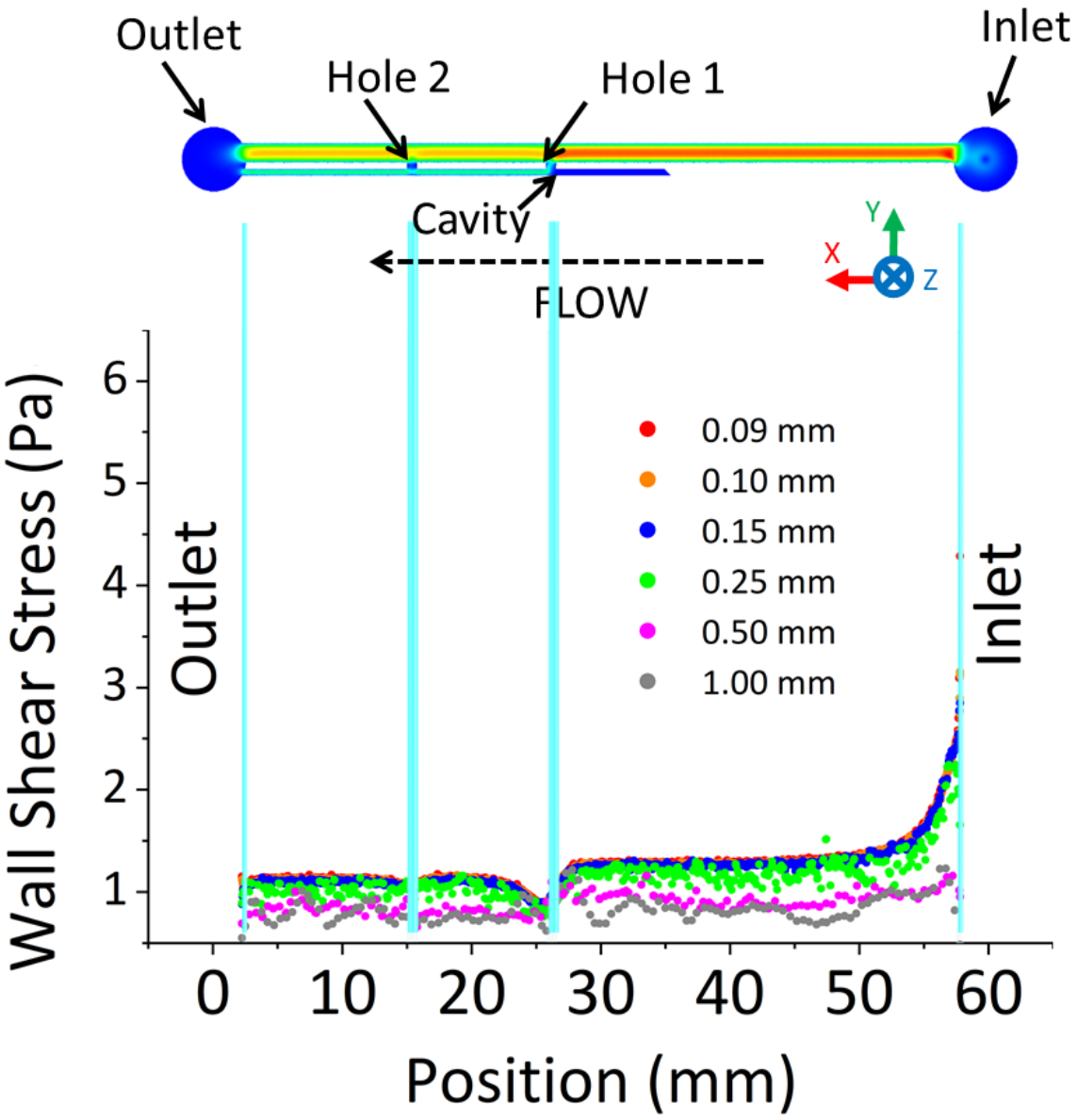

Figure 3-4 Magnitude of shear stress (in Pa) along the wall centreline of the stent compartment, calculated numerically at different mesh volume sizes, namely 0.09, 0.1, 0.15, 0.25, 0.5 and 1 mm. The light blue lines correspond to the device inlet, outlet and side-holes of the stent. The contour of fluid velocity magnitude over the model midplane (i.e., in the z-direction) is also reported (top).

A steady state, laminar flow model was employed to solve for mass and momentum conservation equations, given that the inlet Reynolds number was estimated to vary from 1.6 to ~330. Urine (which has comparable density and dynamic viscosity to water [177]) was assumed to be a Newtonian and incompressible fluid, with density of 997.044 kg/m^3 and dynamic viscosity of 0.001 Pa·s.

Simulations were performed at varying inlet flow rates. Particular attention was devoted to the fluid velocity magnitude ($|\boldsymbol{v}|$) and the wall shear stress (***WSS***), as potential determinants of the formation and growth of encrusting deposits. These were defined as follows:

$$|\boldsymbol{v}| = \sqrt{|\boldsymbol{v_x}|^2 + \left|\boldsymbol{v_y}\right|^2 + |\boldsymbol{v_z}|^2} \quad \text{(Eq 3-1)}$$

where $\boldsymbol{v_x}$, $\boldsymbol{v_y}$, and $\boldsymbol{v_z}$ represent the components of the velocity vector in the *x*-, *y*- and *z*-direction, respectively. And

$$\boldsymbol{WSS} = -\mu \frac{\partial \boldsymbol{v}}{\partial \boldsymbol{n}} \quad \text{(Eq 3-2)}$$

where ***n*** is the unit vector normal to the wall.

3.3.5 Statistical Analysis

The experimental data are presented as the mean ± standard deviation. Differences between particle deposition in Hole 1, Hole 2, and Cavity (for occluded SoC) and Hole 1 and Hole 2 (for unoccluded SoC) were evaluated using an unpaired Welch's *t*-test. The correlation between the variables of time and mean coverage area was evaluated by conducting a linear regression analysis (see Table 3-2). RStudio (RStudio®, USA) and XLSTAT (XLSTAT®, USA) software were used to conduct the analyses. The null hypothesis statement was "the data are the same and there is no difference between them", while the alternative hypothesis statement was "A series of data has a lower value than the other". The significance level (Alpha) was set to 0.05 (i.e., differences were considered to be statistically significant for $p < 0.05$).

Table 3-2 List of fixed elements and variables used for the linear regression model, for both occluded and unoccluded SoCs.

	Fixed element	*Variable*	*Fixed element*	*Variable*

Occluded	*1 mL/min*	Hole 1 Hole 2 Cavity	*1 0 mL/min*	Hole 1 Hole 2 Cavity
Unoccluded	*1 mL/min*	Hole 1 Hole 2 Cavity	*1 0 mL/min*	Hole 1 Hole 2 Cavity

3.4 **Results**

3.4.1 Experimental validation of the simulations

Figure 3-5a shows a comparison between the experimental and simulated (computational) flow streamlines, at three regions of interest within the model. All experimental repeats showed strong qualitative agreement with the numerical simulations in describing the flow field, in both proximal and distal side-holes and the occluded cavity. Figure 3-5a demonstrates a quantitative comparison between computational and experimental pathlines, with measurement of (i) the distance between the centre of the vortex and the stent wall, and (ii) the position of the interface between intra-luminal and extra-luminal streamlines within Hole 2.

3.4.2 WSS influences formation and growth of encrusting deposits in stents

Simulations revealed the spatial distribution of WSS over the solid surfaces of the modelled SoCs. The contour of WSS over the bottom-wall is reported in Figure 3-5b,c. Hole 2 (i.e. located well downstream of the obstruction) represents a fairly stagnant flow region and is therefore characterised by low WSS (average WSS = 1.6×10^{-4} Pa). On the contrary, in Hole 1 (i.e. right in proximity to the obstruction), the flow diversion caused by the obstruction imposes higher levels of WSS (average WSS = 0.038 Pa). The occluded cavity, where the laminar vortex was observed, is also characterised by low levels of WSS (average WSS = 0.010 Pa). It is therefore anticipated that regions potentially susceptible to the formation and growth of encrusting bodies include: side-holes of the stent interested by negligible inter-compartmental flow exchange (i.e. Hole 2) and the cavity formed by the obstruction.

This is confirmed in Figure 3-5c, which shows accumulation of encrusting deposits within side-holes and the occluded cavity, at an inlet flow rate of 1 mL/min (up to 90 min). As anticipated, on the one hand, the side-hole characterised by low WSS (Hole 2) suffered from significant deposition of encrusting bodies. On the other hand, the side-hole characterised by higher levels of WSS (Hole 1) had a much lower degree of encrustation compared to Hole 2. Notably, encrustation appeared to grow unevenly within a single side-hole, with lower shear stress regions characterised by greater encrustation rates (see Figure 3-5c, for direct comparison between WSS and encrustation maps). The occluded cavity, characterised by low WSS, also experienced significant accumulation of encrusting bodies.

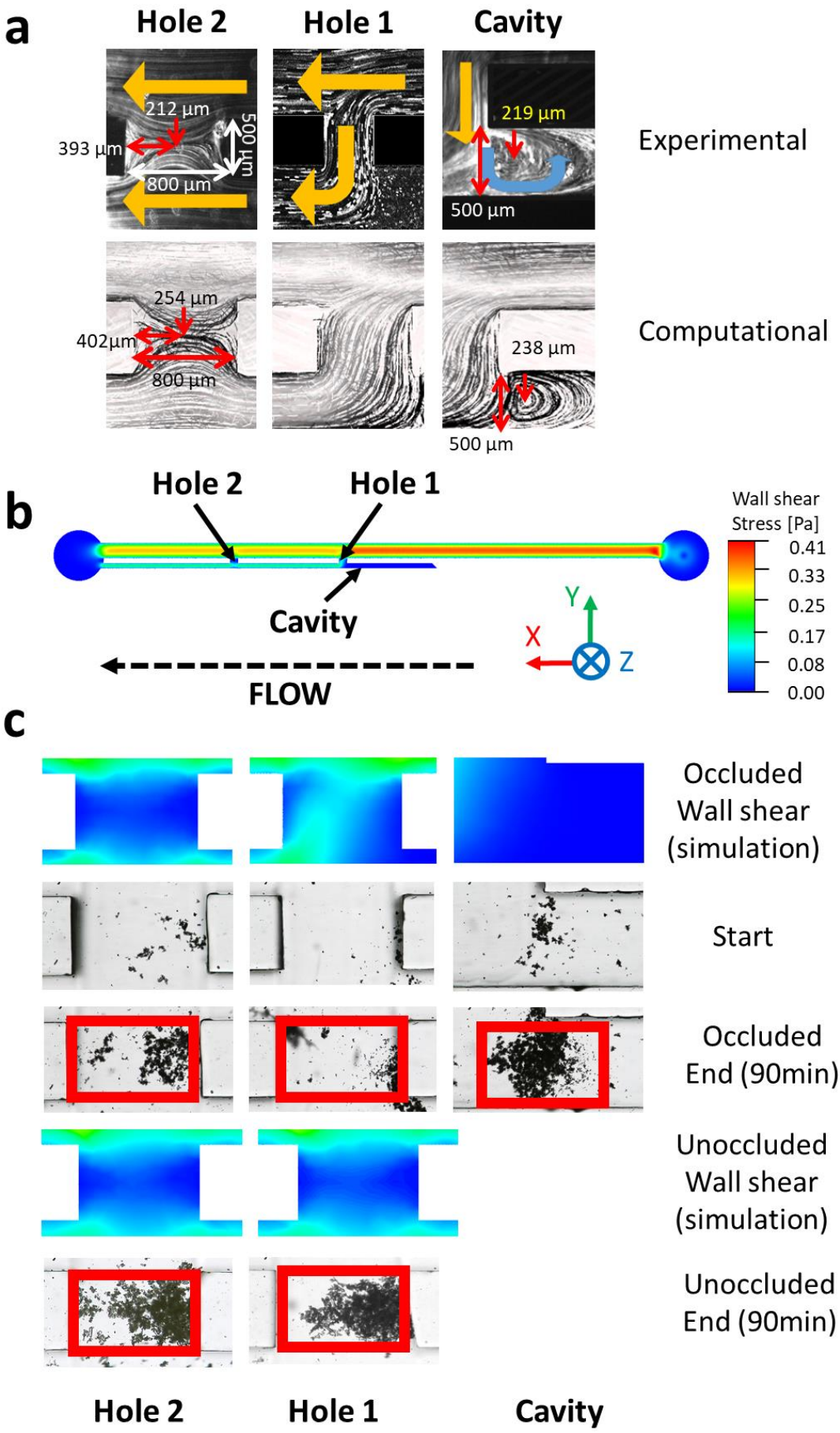

Figure 3-5 (a) Experimental fluid streamlines obtained from flow visualisation tests, and corresponding streamlines determined from CFD simulations. Results were taken at a

fixed volumetric flow rate of 1 mL/min, and arrows indicate the flow direction. A quantitative comparison between experimental and numerical streamlines has also been performed, by measuring (i) the distance between the centre of the vortex and the stent wall and (ii) the position of the interface between intra-luminal and extra-luminal streamlines within Hole 2. (b) Contour of WSS magnitude at the bottom plane (bed) of the SoC model, computed numerically. Blue and red colours correspond to low and high levels of WSS, as indicated in the coloured scale bar. (c) Contours of WSS at key hydrodynamic regions within the occluded model (Hole 1, Hole 2, and the cavity) and unoccluded model (Hole 1 and Hole 2) and the corresponding microscope images showing encrusting deposits, at an inlet flow rate of 1 mL/min. Images were taken at 0 min and 90 min from the beginning of the experiment (n = 5). Red boxes correspond to the regions of interest, over which the % coverage area occupied by encrustation was calculated. Please refer to the scale bar in (b) for WSS values.

Figure 3-6 and 3-7 provide a further quantitative analysis of encrustation, as described in the methodology paragraph 3.3.3. As shown in Figure 3-6a for the occluded model, at a flow rate of 1 mL/min, Hole 1 had a lower coverage area compared to Hole 2, which was characterised by lower WSS. The mean % coverage area after 90 min was equal to 7.6 ± 0.8 % (Hole 1) and 13.8 ± 3.8 % (Hole 2), respectively; however, their difference was not statistically significant (P = 0.1831, see Figure 3-8a). The time evolution of encrustation in both Hole 1 and Hole 2 followed a linear function, as demonstrated by the linear regression of the mean coverage area *vs.* time data point (Hole 1: R^2 = 0.914, P = 0.0030, growth rate (gradient) = 3.06 min^{-1}; Hole 2: R^2 = 0.976, P = 0.0002, growth rate = 2.90 min^{-1}). Both Hole 1 and Hole 2 presented lower encrustation compared to the cavity region, which was characterised by mean % coverage area of 26.9 ± 6.0 % after 90 min (Figure 3-6a) . Results showed a significantly lower % coverage area at Hole 1 compared to the Cavity (P = 0.0328; see Figure 3-8a), but a non-significantly lower value in Hole 2 compared to the Cavity (P = 0.1114; see Figure 3-8a).

Increasing the inlet flow rate to 10 mL/min resulted in a significant (approximately 1-order of magnitude) decrease in the % coverage area (Figure 3-6b). The decrease between mean % coverage area at 10 mL/min and at 1 mL/min (after 90 min) was statistically significant, for both side-holes and the occluded cavity (Hole 1 (very significant): P = 0.0082; Hole 2 (significant): P = 0.0427; Cavity (significant): P = 0.0204; see Figure 3-8a).

At 10 mL/min, the % coverage area in Hole 1, Hole 2 and the Cavity (after 90 min) was equal to 0.34 ± 0.13 %, 2.86 ± 1.74 % and 4.77 ± 1.16 %, respectively. There wasn't a statistically significant difference between Hole 1 and Hole 2 (P = 0.2214, see Figure 3-8a). However, Hole 1 had a statistically lower coverage area compared to the Cavity (P = 0.01857, see Figure 3-8a), while encrustation at Hole 2 was not statistically different compared to the cavity (P = 0.3937, see Figure 3-8a).

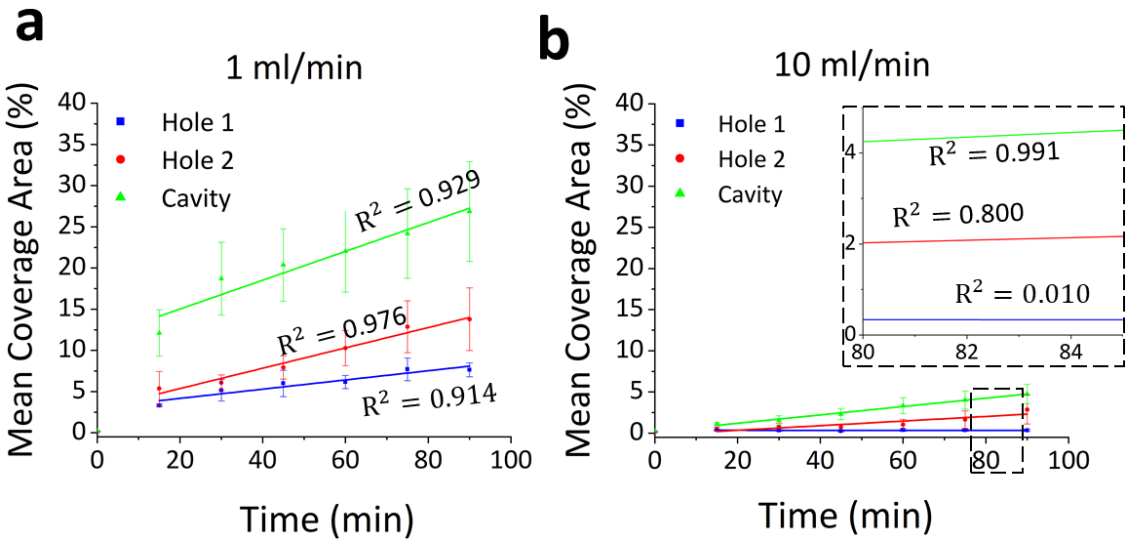

Figure 3-6 Time evolution of the % area covered by encrustation, at specific regions of interest within the SoC models (occluded with two side-holes and a cavity). Results are reported for inlet flow rate of (a) 1 mL/min and (b) 10 mL/min, and are expressed as the mean ± standard deviation of five independent repeats. Linear regression models for the time period 15 minutes to 90 minutes are plotted and R^2 value are mentioned above linear fits.

As shown in Figure 3-7a, in the unoccluded model Hole 1 and Hole 2 had comparable levels of particle deposition at both 1 mL/min and 10 mL/min (Figure 3-7a). In other words, both holes were characterised by low WSS levels (see Figure 3-5c). The mean % coverage area after 90 min was equal to 17.6 ± 7.7 % (Hole 1) and 19.7 ± 9.4 % (Hole 2) at 1 mL/min, and 1.0 ± 0.6 % (Hole 1) and 1.0 ± 0.2 % (Hole 2) at 10 mL/min, respectively. Values taken at 10 mL/min had significantly lower values (statistically) compared to those taken at 1 mL/min, and the difference was statistically significant at both side-holes (Hole 1: P = 0.0463; Hole 2: P = 0.0421).

It should be noted that Hole 1 and Hole 2 of the unoccluded model present a similar functional behaviour to those in Hole 2 of the occluded model. Values of mean coverage area at both flow

rates of 1 mL/min (Hole 2 Occluded *vs.* Hole 1 Unoccluded: P = 0.8672, Hole 2 Occluded *vs.* Hole 2 Unoccluded: P = 0.8385) and 10 mL/min (Hole 2 Occluded *vs.* Hole 1 Unoccluded: P = 0.8227, Hole 2 Occluded *vs.* Hole 2 Unoccluded: P = 0.4092) didn't show a statistically significant difference.

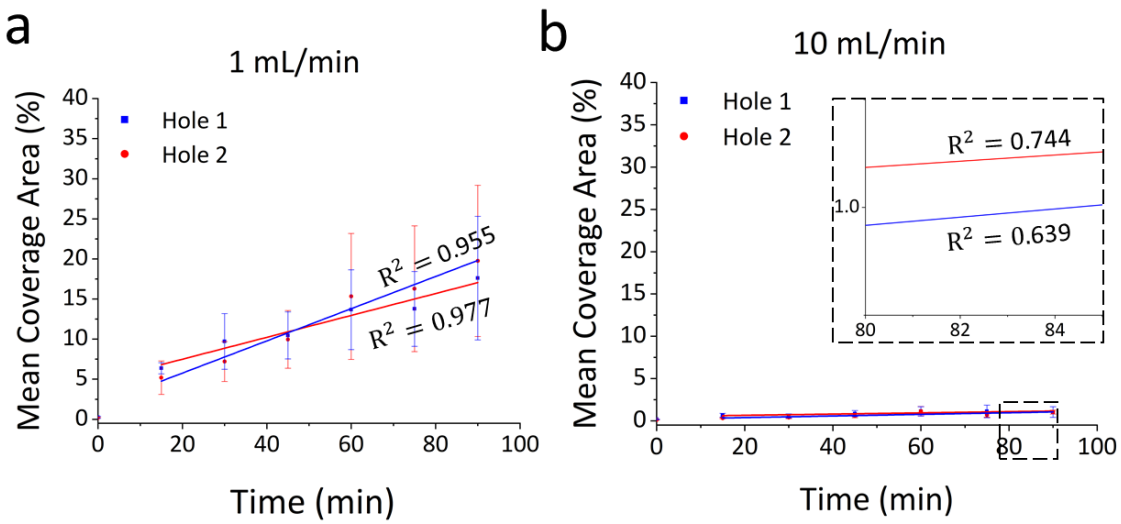

Figure 3-7 Time evolution of the % area covered by encrustation, at specific regions of interest within the SoC model (unoccluded, with two side-holes). Results are reported for inlet flow rate of (a) 1 mL/min and (b) 10 mL/min, and are expressed as the mean ± standard deviation. Linear regression models for the time period 15 minutes to 90 minutes are plotted and R^2 value are mentioned above linear fits.

Figure 3-8a shows the mean % coverage area (determined experimentally) measured over different regions of interest, for both flow rates of 1 mL/min and 10 mL/min. Additionally, Figure 3-8b shows the mean % coverage area (determined experimentally) *vs.* mean WSS (determined computationally), measured over the three regions of interest within SoCs, at both 1 and 10 mL/min. Results demonstrate an inverse and non-linear correlation between size of encrusting deposits and WSS.

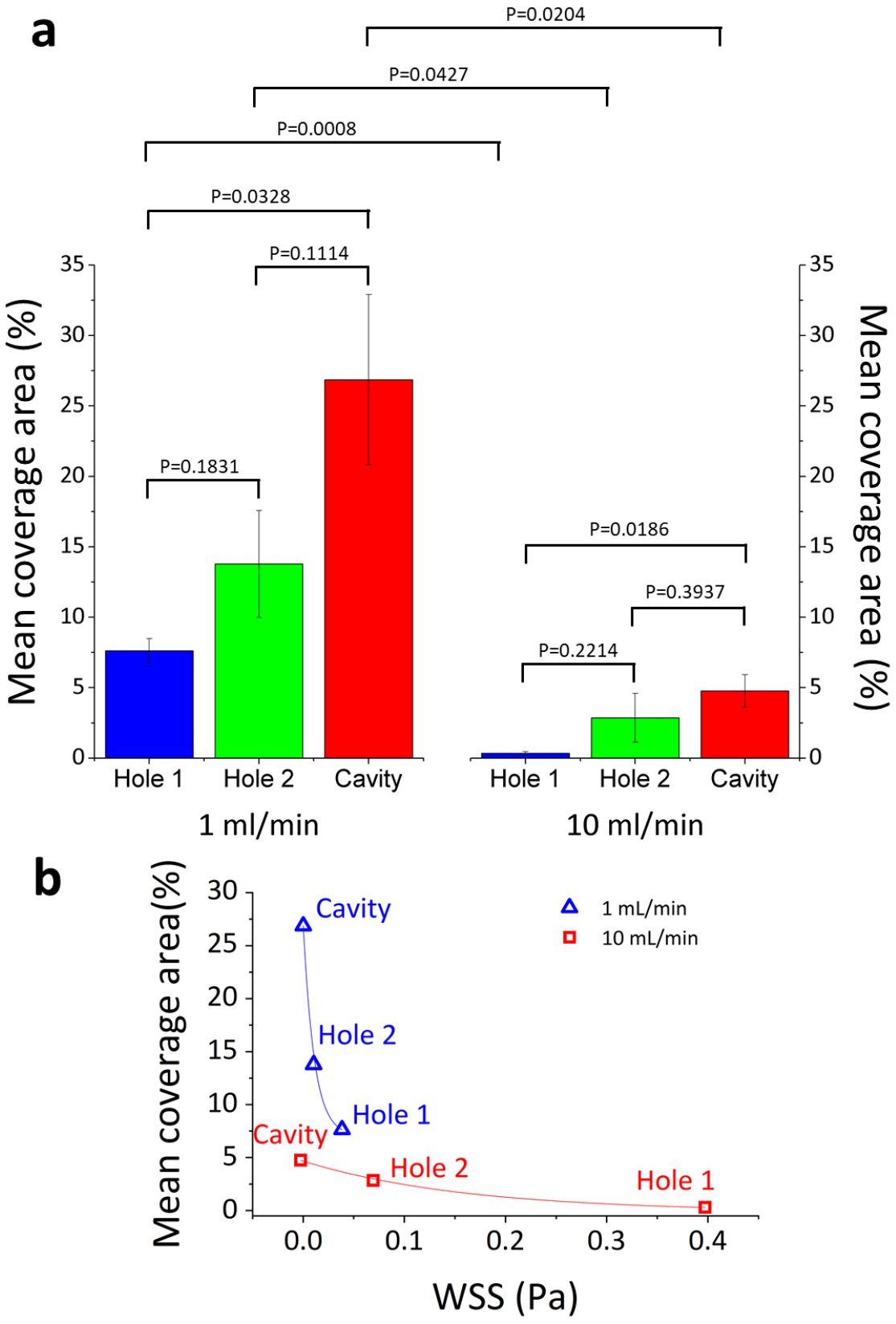

Figure 3-8 (a) Mean % coverage area after 90 min, at both 1 mL/min (left) and 10 mL/min (right), measured in Hole 1, Hole 2, and the occluded cavity. (b) Mean % coverage area plotted as a function of mean WSS, at both 1 and 10 mL/min. Values were measured in Hole 1, Hole 2, and the occluded cavity.

3.5 Discussion

Ureteric stents are frequently employed in the clinic to restore drainage in the occluded ureter. Despite their clinical success, stents suffer from complications and side effects. Formation and deposition of encrustation over the stent surface is widely recognised as a primary cause of complications, and is likely to be affected by the flow distribution in the stented ureter.

A few experimental models have been developed and employed to investigate flow processes associated with ureteric stents, either *in-vitro* or *ex-vivo* [30, 87, 178-181]. Using an artificial dynamic model, Gorman and co-authors measured lower levels of encrustation in stents exposed to dynamic flow conditions as opposed to static conditions, suggesting a significant "cleaning" action of the bulk flow [180]. Moreover, some studies revealed that side-holes of the stent are often associated with higher deposition of encrustation, and suggested that holes may act as initial anchoring sites for encrustation [87, 182]. This is also confirmed to some extent by the inspection of stents retrieved from patients, where it was observed that the majority of side-holes were plugged with crystals [183]. It is also well known that proximal and distal coils of a ureteric stent often suffer from encrustation, as reported in clinical studies [184, 185]. This is likely due to the stagnant nature of the flow in those regions, resulting in low WSS levels over the inner and outer surface of the coil.

Moreover, Clavica *et al.* [165] argued that laminar vortices forming in the vicinity of obstructions may also be considered as encrustation "hot spots", as they are effective in entrapping particles suspended in the fluid and therefore in promoting their deposition.

Waters *et al.* [49, 162] employed a theoretical model to study the flow field and its relation to biofilm and crystal deposition in stented ureter models. They concluded that differences in the crystal structure, chemical composition and localisation of encrustations could depend strongly on the local flow environment.

The studies cited above suggest that, despite the very low-flow regime (i.e. akin to almost static conditions) normally encountered in stented ureteric systems, flow processes may dictate where, and at which rate, encrustations can grow over the stent surface. This is extremely relevant because, if confirmed, it can open new avenues for improving the stent's design *via* fluid dynamic optimisation. For instance, earlier computational studies have shown that increasing the number of side-holes could increase the drainage flow rate [186], although this effect was minimal in the absence of a ureteric occlusion. In a prospective randomized clinical study by Damiano *et al.* [187], no differences in quality of life, urinary symptoms, and pain were found when using stents

with different diameter, suggesting that further efforts should be devoted to more effectively improve the flow dynamic performance of stents.

Unfortunately, the literature is inconclusive on this specific issue as it lacks of systematic studies addressing the direct correlation between flow metrics and encrustation rates. The microfluidic-based models of a stented ureter developed in this study allowed to reveal, for the first time, a robust inverse correlation between deposition of encrusting bodies and the local WSS in a stented ureter model.

Importantly, the flow features in the SoC models were in agreement with previous studies where more accurate replicas of stented ureters were employed [165, 188]. In the presence of a ureteric obstruction, inter-compartmental fluid exchange occurred only in the first side-hole post-obstruction, coherently with earlier numerical studies [188], and a laminar vortex formed within the obstructed cavity as previously observed by Clavica *et al.* using a full-scale artificial ureter model [165].

Moreover, critical regions susceptible to encrustation were identified in this study, which included 'inactive' side-holes (i.e., with minimal or absent flow exchange between stent and ureter) and the cavity formed by a ureteric occlusion. In the cavity, encrustation occurred due to the generally low WSS levels and perhaps the trapping effect caused by the laminar vortex. Increasing WSS resulted in a significant reduction in particle deposition rates in all regions of the model investigated. Increased WSS levels in these critical regions could be achieved by altering the architecture of the stent locally, to promote fluid drainage through side-holes.

3.6 Conclusion

The microfluidic devices developed in this study provide a fast, cost-effective to fabricate (compared to conventional microfabrication techniques), and reliable screening platform for investigating the interplay between flow processes and encrustation dynamics in stents.

As a result of this study, it could be speculated that the majority of side-holes in a real stented ureter system can act as stagnation sites, and therefore represent potential "hot spots" for the anchoring and deposition of encrusting deposits. These hydrodynamic regions can then provide an environment for the growth of larger crystals and the entrapment of bacteria to form a complex bio-chemical layer, as described in previous studies [189]. Occlusion of side-holes can significantly affect urine drainage in the stented ureter, as they are an important functional component of the stent. Therefore, the following chapters will discuss attempts to modify the stent architecture in those critical regions, in order to reduce deposition of encrusting particles.

However, some considerations have to be made relating to the relevance of 'stent-on-a-chip' models with respect to the clinical and physiological scenario, and to the approximations made using this modelling approach. In a full-scale stent, there are several factors than can potentially affect the flow and wall shear stress distribution over a stent, including stent's thickness and inner diameter, and the number, size and shape of its side-holes. These parameters will be investigated in the future, using both SoC and full-scale numerical models of the stent. The effect of patient's posture (i.e. orientation of the stent) on crystals' deposition will also be investigated. Notably, a qualitative verification of the findings reported in the present study on a full-scale is reported in the next chapter.

Moreover, stent encrustation is a complex process involving several physical, chemical and micro-biological factors, each occurring at different temporal scales. The main focus of this study was on the deposition of encrusting crystals - a process that is likely to play an important role in stent encrustation, given the low-flow regime encountered in a stented ureter. Future work will however investigate the effect of changing the fluid chemical composition and pH on the formation and growth of crystals. For this purpose, microfluidic devices could be integrated with micro-Computed Tomography or Raman scattering technologies to investigate crystals structure and chemical composition *in situ*.

Despite they replicate relevant features of the flow field in a stented ureter, SoC models do not mimic some characteristic behaviours of a physiological ureter, including distensibility of the ureteral wall, ureteral peristalsis, and ability to adapt to pelvic pressures in case of obstruction. Moreover, whilst different levels of ureteric occlusion may occur *in-vivo* (encompassing total and partial obstruction), only a complete occlusion of the lumen was replicated in this study. Furthermore, images of particle deposition have been limited to the bottom surface (or bed) of the SoC model. Future work may focus on a three-dimensional determination of encrustation, which may be achieved by using different imaging techniques.

Chapter 4 3D simulation of the flow field in a stented and occluded ureter

4.1 Outline

The aim of this study is to verify some of the key findings obtained using stent-on-chip models (described in Chapter 3) on a full-scale. If successful, this verification would further demonstrate the validity of the developed stent-on-chip models in replicating relevant flow features of a stented and occluded ureter model. Particular attention will be devoted to (i) the correlation between WSS at side-holes and the deposition of encrusting particles; (ii) the WSS distribution at side-holes along the stent; and (iii) the effect of a ureteric obstruction on the WSS field. Numerical simulations and experiments were performed on a full-scale model of the stented ureter to evaluate a spatial correlation between WSS and encrusting deposits. Upon verification of this correlation, the computational model was employed to investigate the flow field within a full-scale occluded and stented ureter.

4.2 Introduction

Theoretical and experimental models have been developed to investigate the flow dynamics in the upper urinary tract, both in the presence and in the absence of ureteral stents. Some of these studies are discussed below, particularly in terms of the physical assumptions made to model a specific compartment of the urinary system or a physiological/pathological condition.

In 1970, Lykoudis *et al.* [190] developed a fluid mechanical model to study the function of the healthy ureter. By imposing physiologically relevant boundary conditions, they demonstrated that the theory of lubrication was able to accurately describe the flow dynamics in the ureter to the extent that the Reynolds number was ~1. Notably, authors designed an approximate equation for urine flow, and a universal relation between maximum pressure, urine flow, and kinematic behaviour of the ureter. It was found that pressure in the ureter during contraction increased by 25 mmHg compared to its resting state. Reflux or other pathological conditions (i.e., occlusions or flow restrictions) were not modelled in this study.

In 2004, Cummings *et al.* employed theoretical fluid dynamics to study the effect of a ureteral stent on the flow field in the ureter, focusing specifically on the occurrence of reflux. They established an axisymmetric model of the stent in order to study the effect of side-holes on drainage [190]. Due to the loss of peristalsis in a stented ureter, urine flow was assumed steady

and governed by pressure differences between the upper urinary tract (kidney) and the lower urinary tract (bladder), whilst the bladder pressure was assumed constant. Authors concluded that occurrence of reflux as a result of increased bladder pressure could be controlled by increasing the stent porosity (by up to 30%). Holes were also proven to have a positive effect in decreasing reflux [50].

Waters *et al.* [49, 50, 191] developed an axisymmetric theoretical model to investigate urine flow in a stented ureter, and its potential implications on encrustation. As for previous studies, they neglected ureter peristalsis. The renal pelvis was modelled as an elastic compartment, with a linear dependence between pressure and urine reflux at the uretero-pelvic junction (UPJ). Results from this study showed an increase in reflux due to increased bladder pressure. The study also suggested that encrustation could happen in the absence of bacteria [49, 50, 191], and that differences in the crystal structure and chemical composition of encrustation could depend on the local urine composition. However, no experimental evidence was provided to support this hypothesis.

In 2007, Tong *et al.* carried out a numerical study using computational fluid dynamics (CFD) to investigate how urine flow would be influenced by (i) the number of side-holes and their location along the circumference of the stent, (ii) the distance between stent and ureter wall, and (iii) the presence of a flow blockage. Seven different stent architectures were designed for this purpose. Water was selected as the working fluid in this study, and the pressure difference between kidney and bladder was kept constant (at 48.9 Pa). The study revealed that presence of holes along the stent had no effect on flow distribution, in the absence of ureteral occlusions. This observation was confirmed by changing the number of blockages, as well as their size and location. Furthermore, it was demonstrated that only the holes located just before and after the blockage were interested by fluid flow (i.e., fluid exchange between the stent and the ureter) [192]. This may have important implications on the spatiotemporal dynamics of encrustation.

Recently, Gomez-Blanco *et al*. conducted a study to understand the interaction between urine flow and a stented ureter (using a double-J stent). A Fluid-Structure Interaction (FSI) computational model was designed for this purpose. It comprised of a cylindrical tube (ureter) with isotropic hyperelastic quasi-incompressible walls, mimicking a pig ureter connecting the uretero-pelvic junction (UPJ) to the vesicoureteric junction (VUJ). The stent was co-axial with respect to the ureter, and was modelled as a rigid body. Data obtained from *ex vivo* and *in vivo* mechanical tests on ureters were used to fit the above-mentioned models. Results from this study showed a negligible mechanical interaction between the stented ureter and urine flow. Authors

therefore concluded that the flow dynamics in a stented ureter can be faithfully described using a more computationally efficient CFD modelling approach [193].

In addition to mathematical and computational modelling, studies have focused on understanding the role of fluid dynamics through experimental models. For example, Choong *et al.* performed a study to measure encrustation in ureteral stents, by developing an artificial model of the urinary system. It comprised of two reservoirs, replicating kidney and bladder compartments respectively, and a rigid tube replicating the ureter. The stent was placed within the tube and the system primed using human urine. To prevent bacterial growth, antibiotics (vancomycin and gentamicin) were added to the urine. Authors investigated encrustation rate over the stent surface and compared two commercially available ureteral stents made of different materials (Silicon - Cook® Medical C-Flex vs Polyurethane - Cook® Medical Soft Flex). Results showed lower encrustation on silicon compared to polyurethane [54].

A recent study by Clavica *et al*. investigated the flow dynamics within an artificial model of occluded and stented ureter. A polydimethylsiloxane (PDMS) ureter model was fabricated by replica moulding, utilising a 3D-printed mould. Using this model, authors quantified the relation between the renal pelvic pressure and urine physical properties (i.e., viscosity), degree of obstruction, and volumetric flow rate. The study demonstrated that, at certain physical conditions, the kidney pressure may increase up to pathological levels because of ureteric occlusion and stenting. Numerical simulations were also performed to understand the local fluid dynamic field nearby the obstruction, and the presence of laminar vortices was revealed for the first time [30]. Authors concluded that vortices might act as trapping sites for encrusting deposits and therefore be a primary site for encrustation. However, an experimental validation of their hypothesis was not provided.

The aim of the present study was to further verify the findings obtained using the stent-on-chip models (outlined in Chapter 3), that (i) demonstrated an inverse correlation between WSS and deposition of encrustation, and (ii) suggested that the large majority of side-holes in a stent were inactive (i.e. not interested by inter-compartmental fluid exchange) and thus prone to encrustation. Validating these findings at a full-scale is a critical step of the present study, as the novel stent designs presented here primarily aim at increasing the WSS field in those regions of the stent.

4.3 Materials and methods

The ureter model used in this study was designed based on the model geometry proposed by Clavica *et al.* [165], which was reconstructed from pig ureters. The present study employed this

model in order to perform *in-vitro* experiments on a commercially available double-J stent (Model: Universa®, Cook® Medical, USA) to identify regions of the stented ureter suffering from deposition of encrustation. Computational fluid dynamic (CFD) simulations were then carried out to investigate the flow field within regions of interest of the stented ureter, and numerical results were correlated with the experimental observations.

4.3.1 Simulation of the flow field

CFD simulations were performed to investigate the flow dynamic field within a stented ureter, and the computational model was defined to replicate the experimental conditions. A CAD drawing of the ureter model was initially constructed using Autodesk® Inventor Pro 2018 (Autodesk®, USA), based on the geometrical data provided in a previous study by Clavica *et al.* [165]. The fluidic domain was then derived by subtracting the stent model (built based on the specifications of the commercial stent Universa®, manufactured by Cook® Medical) from the urinary system model, which was then converted to a format compatible with ANSYS Workbench 18.1 (Ansys Inc., USA). The urinary system model comprised of the ureter model described earlier, and included a renal pelvis and bladder. In order to resolve the wall shear stress (WSS) distribution over the surface of the stent, the fluidic domain was meshed using tetrahedral volumes (25,695,349 to 27,308,086 volumes were used for occluded and non-occluded stented urinary system models, respectively). The minimum and maximum mesh sizes were set to 0.001 mm and 0.1 mm, respectively, based on a compromise between computational cost and solution stability (see Figure 4-1). 1 mL/min was selected as the inlet volumetric flow rate, following previous studies [173, 176]. The simulation parameters were defined based on the procedure described in Chapters 3.

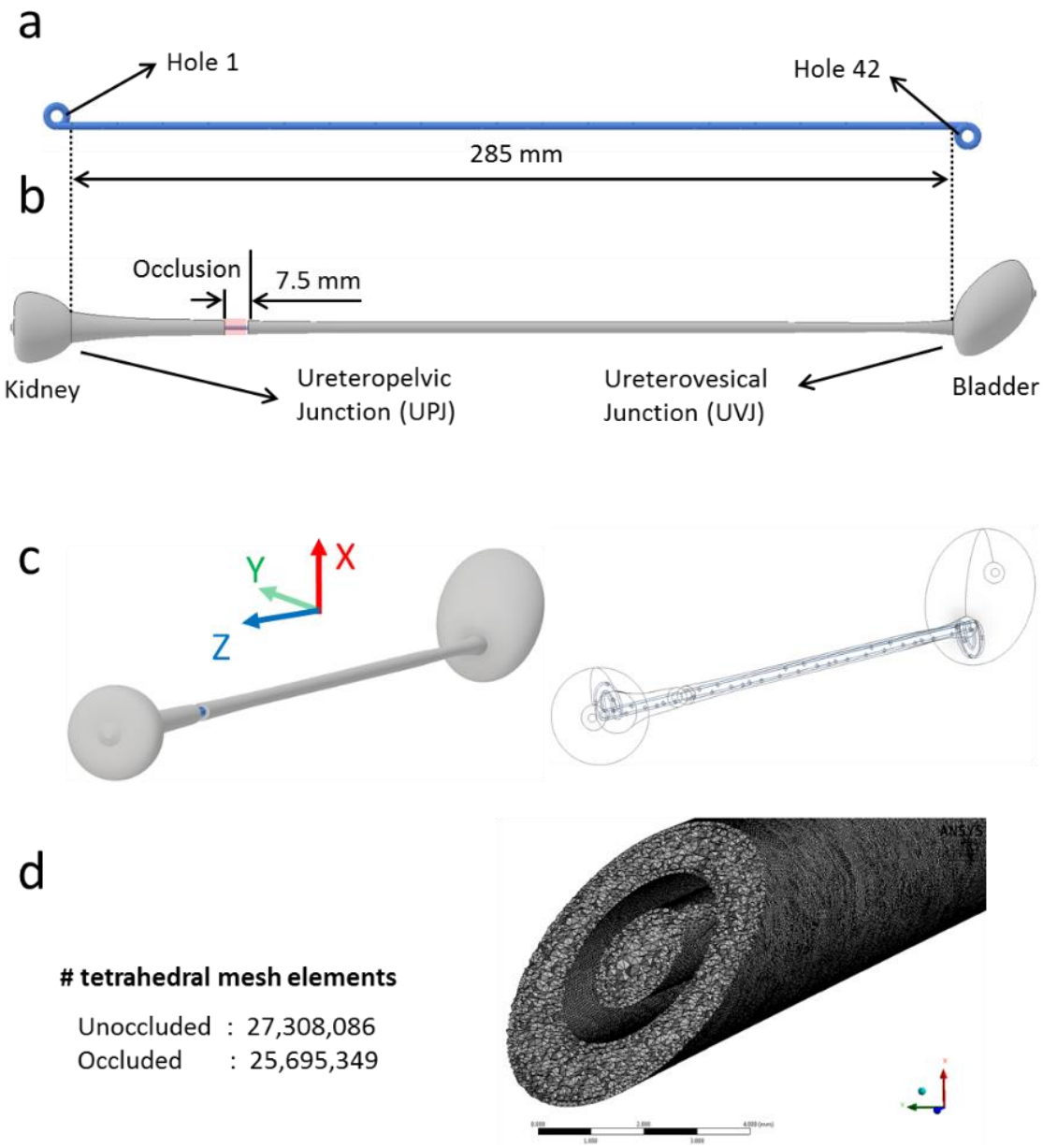

Figure 4-1 CAD drawing of the stent, where the geometrical properties are taken from the commercial double-J stent Universa® (Cook® Medical, USA). The stent has a wall thickness of 0.5 mm, a length of 28.5 mm (excluding coils), an internal diameter of 1.5 mm, and a total number of 42 side-holes that are placed at intervals of 3 to 4, with an average spacing of about 7.5 mm. b) Model of urinary system, including kidney, ureter and bladder. The geometrical properties required to construct this model were taken from Clavica *et al.* [165]. The image also demonstrates a model of ureteric occlusion (highlighted in red). The non-occluded model would have the same geometrical characteristics, without the occlusion. c) Symmetric view of the stented urinary system (obstructed), including its wireframe view and the reference coordinate system. d) Zoomed-in view of the tetrahedral meshing performed on the occluded model. The number of mesh volumes for both non-occluded and occluded models is also reported.

4.3.2 Experimental protocols

In order to investigate deposition of encrusting particles in the stented ureter model, a supersaturated artificial urine (containing calcium chloride) was employed. The urine surrogate composition was taken from Brooks *et al.* [194], with minor modifications. The temperature of the solution during the experiment was kept to the constant value of 37°C, and the pH was equal to 6.8 (measured using a pH meter, Accumet™ AE150 pH, Fisher Scientific™, USA). A reservoir stored the artificial urine during experiments, and a peristaltic pump (Minipuls3, Gilson®) was employed to convey a 1 mL/min flow rate into the stented ureter model (see Figure 4-2). The reservoir was placed on a hot plate stirrer (Stuart® Hot Plate Stirrer) to reduce crystals' precipitation. A camera (EOS 600D, Canon®, Japan) was employed to acquire optical images of encrusting deposits. The camera was placed above the model, and images were acquired at fixed locations along the ureter model (as shown by the labels in Figure 4-2a).

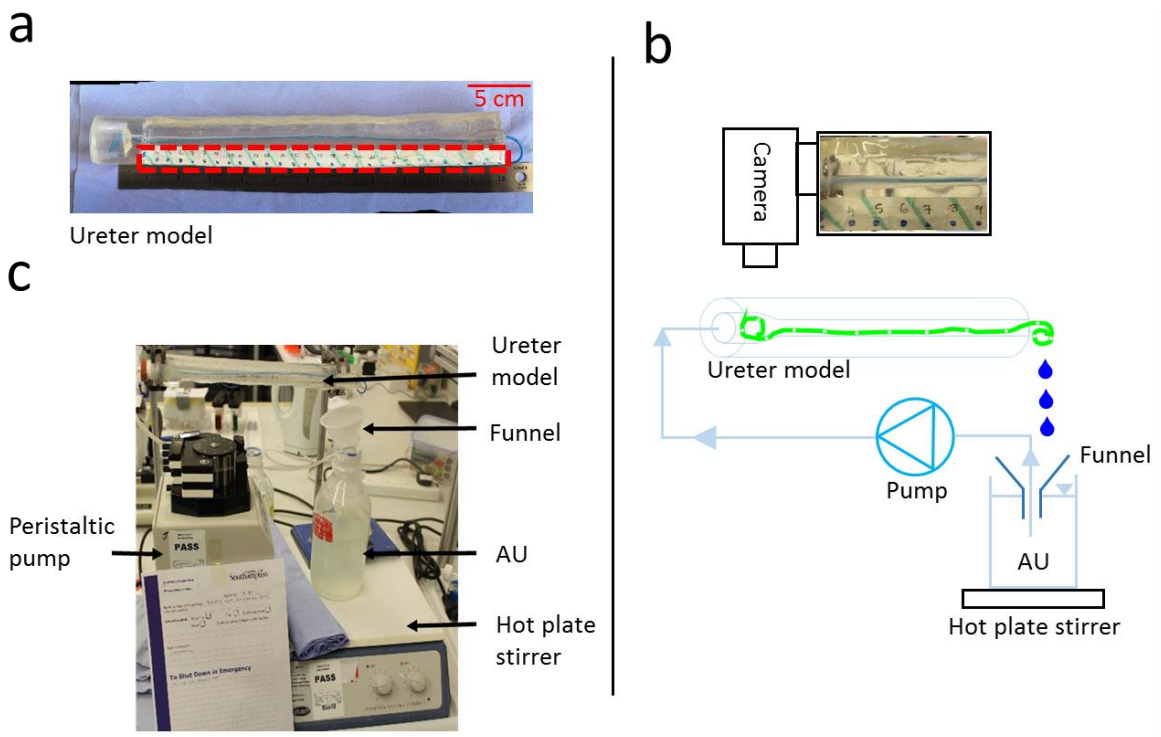

Figure 4-2 Photograph of the *in vitro* ureter model. A more detailed description of the model is provided in [165]. The red dashed box indicates the location of the tape used for labelling positions along the model. (b) Experimental setup adopted in this study to carry out *in-vitro* encrustation tests. It included a reservoir containing supersaturated artificial urine (AU), a peristaltic pump (Minipuls3, Gilson®), a funnel, an hot plate stirrer (Stuart® Hot Plate Stirrer) to reduce crystals' precipitation, the ureter model (with the stent shown in green), and a camera (EOS 600D, Canon®, Japan). A photograph of the setup is reported in (c).

4.3.3 Procedures of the study

In this study, both CFD simulations and experiments were performed to demonstrate a correlation between WSS and deposition of encrusting particles within a full-scale stented ureter. Results were analysed at two different spatial scales: global (i.e. through the whole length of the ureter, from UPJ to UVJ), and local (i.e. at drainage side-holes, from Hole 1 to Hole 42; see Figure 4-1). The first part of the study was conducted on the non-occluded stented ureter model. Following a comparison between numerical and experimental results, the *in silico* model was then employed to investigate the flow field within the occluded stented ureter model.

4.4 Results and discussion

4.4.1 Non-Occluded (NO) model: simulations and experiments

Numerical simulations

Figure 4-3 shows the velocity magnitude determined from CFD simulation in the non-occluded (NO) stented ureter model, taken over the model mid-plane. Results demonstrate higher velocity magnitude in side-holes located at the distal segment of the model, i.e. in the vicinity of the bladder (i.e. 8.13 mm/s, 7.22 mm/s, 2.56 mm/s, 11.18 mm/s, 19.08 mm/s for Hole 33, Hole 34, Hole 35, Hole 36, Hole 37, respectively) compared to those located closer to the proximal end of the model, i.e. in the vicinity of the kidney (i.e. 0.39 mm/s, 0.59 mm/s, 1.01 mm/s, 1.08 mm/s, 1.77 mm/s, 2.45 mm/s, 3.84 mm/s, 4.18 mm/s, 5.06 mm/s, 5.84 mm/s, 4.18 mm/s for Hole 5, Hole 6, Hole 7, Hole 8, Hole 9, Hole 10, Hole 11, Hole 12, Hole 13, Hole 14, Hole 15, Hole 16, respectively). Results indicate that distal side-holes experience a higher degree of inter-compartmental flow exchange compared to the more proximal side-holes. This is likely due to a reduction of the ureter lumen diameter in the region closer to the VUJ, which diverts part of the flow from the ureter lumen into the stent.

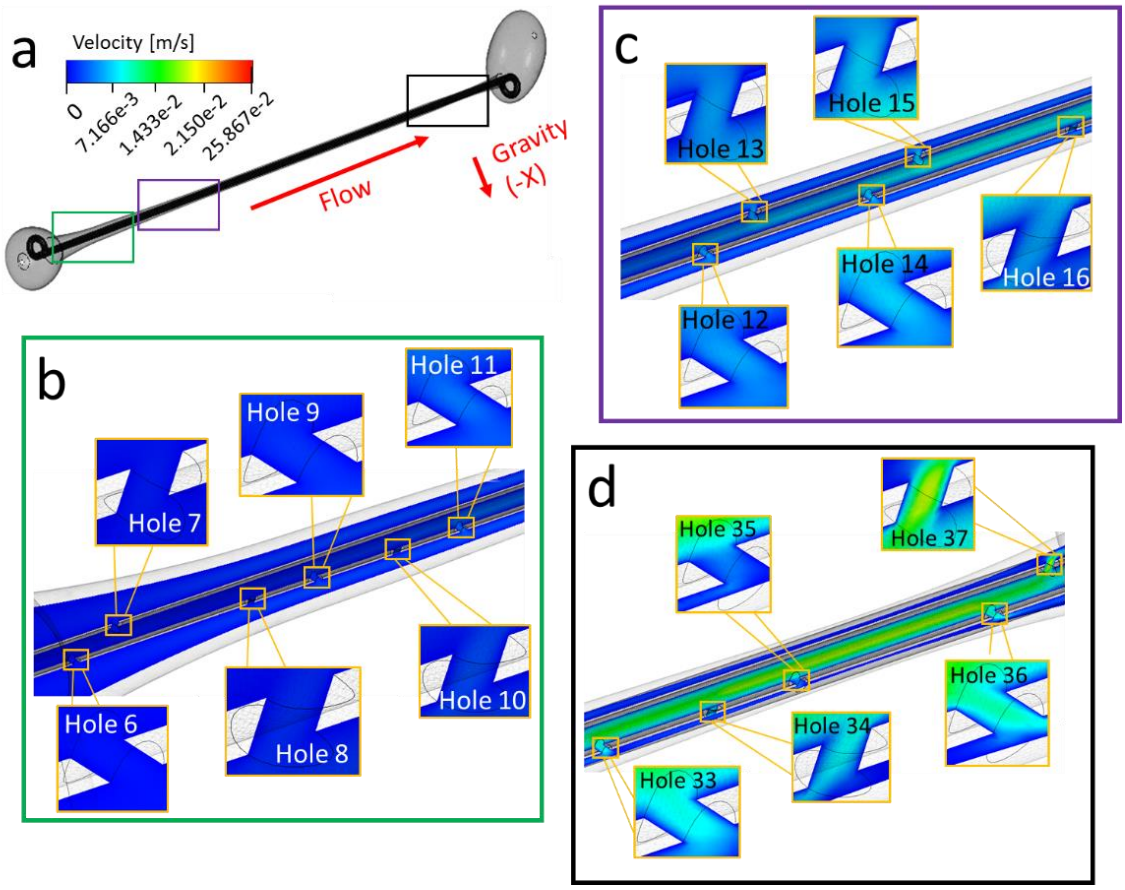

Figure 4-3 (a) Contours of velocity magnitude (in m/s) along the whole model, computed numerically over the model mid-plane. Insets show zoomed-in views of the contours of velocity magnitude at different regions along the ureter (from proximal to distal). These include (b) Holes 6-11, (c) Holes 12-16, and (d) Holes 33-37. Both intra- and extra-luminal compartments nearby a side-hole are shown. Results refer to the non-occluded (NO) model.

Figure 4-4 shows the spatial distribution of WSS magnitude in the non-occluded ureter model, determined from numerical simulations, and plotted over the stent internal wall (SIW). Results demonstrate that the lowest WSS magnitude is acting over the lateral wall of side-holes located in the kidney pelvis (e.g. 3.45e-5 Pa, 1.24e-4 Pa, 2.90e-4 Pa, 5.01e-4 Pa at Hole 1, Hole 2, Hole 3 and Hole 4, respectively). This is coherent with earlier studies showing enhanced encrustation at the proximal coil of the stent [45]. The WSS over the SIW and the side-holes slightly increased from Hole 6 to Hole 12, although it was still lower than 0.04-0.05 Pa. It then reduced to about 0.009 Pa until Hole 31, and increased only in the more distal region (e.g. WSS was equal to 0.049 Pa, 0.046 Pa, 0.023 Pa, 0.069 Pa in Hole 33, Hole 34, Hole 35 and Hole 36, respectively). The distal coil of the stent also suffered from low WSS levels. The box plot in Figure 4-4c shows that the maximum, minimum and mean WSS magnitude over the SIW were 0.14340 Pa, 0.00002 Pa, and 0.01999 Pa,

respectively. The WSS and velocity distributions confirm that holes characterised by inter-compartment flow exchange (referred to as 'active' holes) experience higher levels of WSS, coherently with the microfluidic findings outlined in Chapter 3. Flow exchange occurred in regions of the model that were characterised by a reduction of the ureter lumen, and particularly in proximity to the VUJ. Notably, the large majority of side-holes experienced WSS levels that are anticipated to favour significant deposition of encrusting deposits (based on the results reported in Chapter 3). Notably, WSS values are also in the range of those obtained in the stent-on-chip models previously reported.

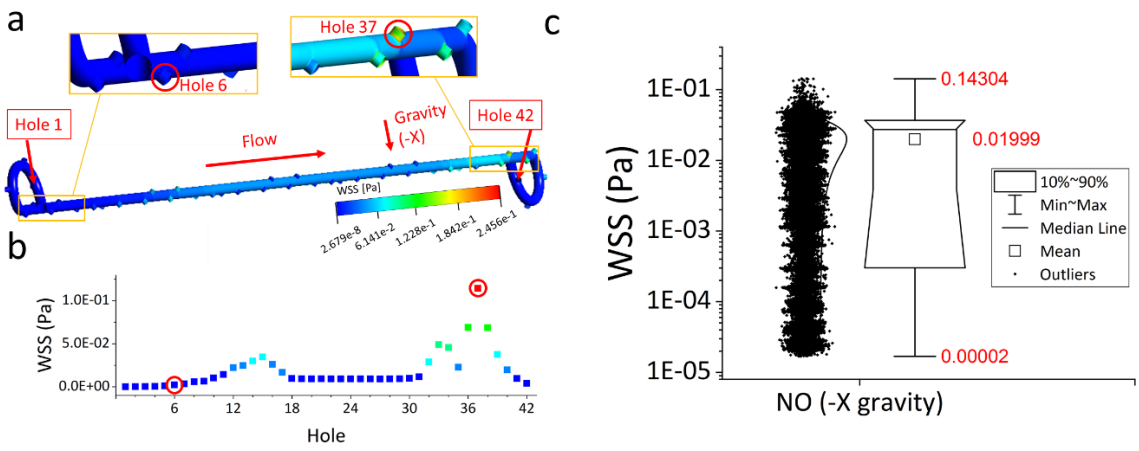

Figure 4-4 (a) Contours of WSS magnitude (in Pa) over the stent internal wall (SIW), computed numerically, as well as the zoomed-in views of WSS contours for both the proximal and distal regions (NO model). (b) Mean values of WSS magnitude (in Pa) calculated numerically for each individual side-hole, from Hole 1 to Hole 42. (c) Distribution of WSS values over SIW plotted in the form of a box plot, covering the ranges of 10%, 25%, 50%, 75% and 90% of the total distribution. Additionally, individual data points are reported next to the box plot. The minimum, maximum, and mean values of WSS magnitude are highlighted in red, next to the corresponding whisker and pointer location in the box plot.

The stent external wall (SEW) was subsequently evaluated. Figure 4-5 shows the spatial distribution of WSS magnitude over the SEW, in the non-occluded model, together with a box plot to illustrate the distribution of WSS values. The maximum, minimum and mean WSS magnitude along the SEW were 0.1116 Pa, 1.1895e-6 Pa, and 0.0131 Pa, respectively. Values were lower than those taken over the internal wall of the stent, at corresponding locations (FigureA-3a),

suggesting that the external surface of the stent may be more susceptible to deposition of encrusting particles.

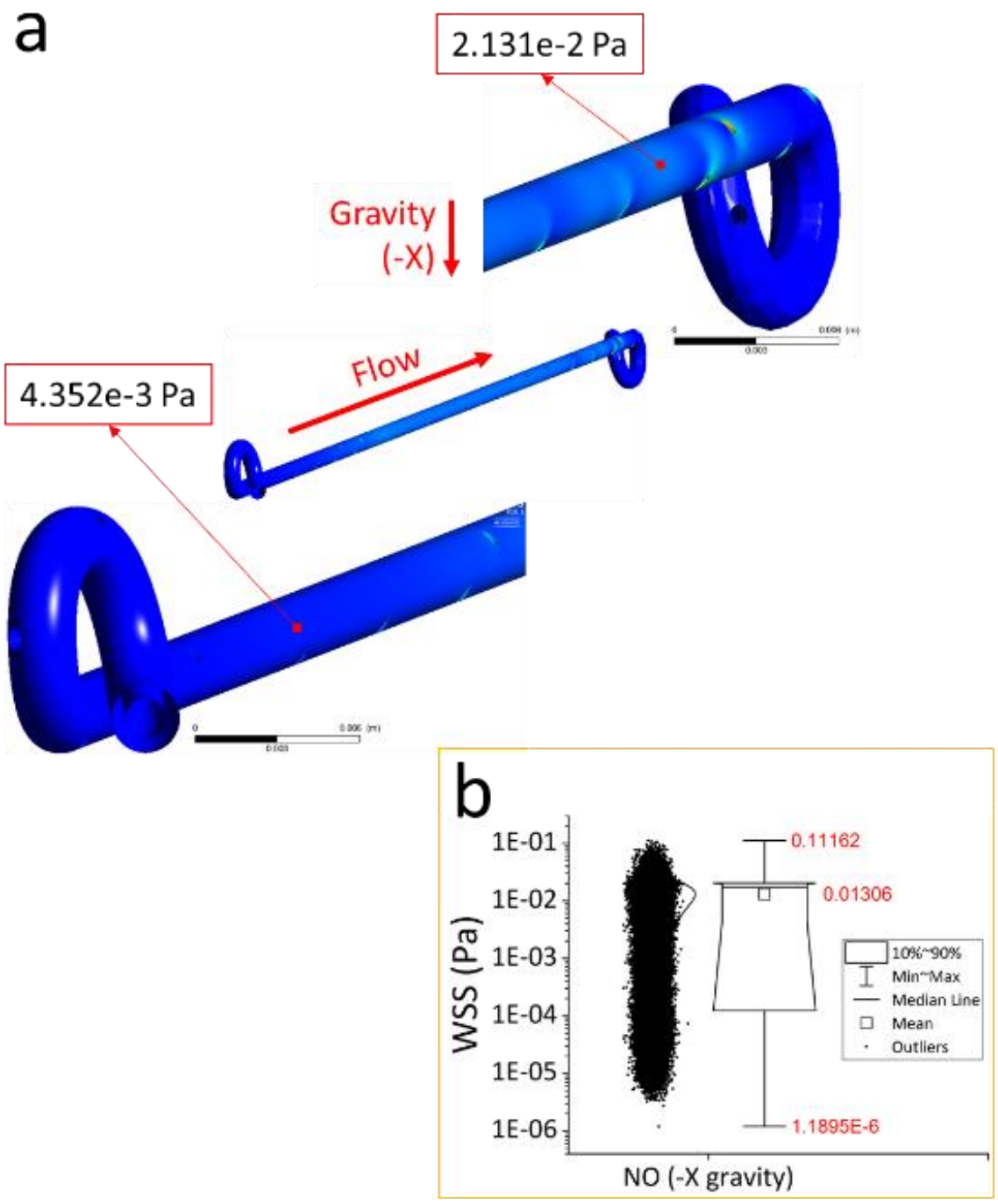

Figure 4-5 (a) Contours of WSS magnitude (in Pa) over the stent external wall (SEW) model, computed numerically, as well as inset zoomed-in views of the contours of WSS magnitude at both the proximal and distal regions (NO model). (b) Distribution of the WSS values over the SEW, illustrated in the form of a box plot covering the ranges of 10%, 25%, 50%, 75% and 90% of the total distribution. Additionally, individual data

points are reported next to the box plot. The minimum, maximum, and mean values of WSS magnitude are highlighted in red, next to the corresponding whisker and pointer location in the box plot.

Experimental analysis

In order to evaluate a correlation between WSS and the deposition of encrusting particles, an experiment was conducted employing the model presented in Figure 4-2. Figure 4-6 shows quantitative values representing the mean % area covered by encrusting bodies, taken at selected side-holes within the model. Measurements were performed at different regions along the model, corresponding to different WSS values. Notably, an inverse correlation was demonstrated between the WSS at side-holes and the % encrusted area, coherently with the findings reported in Chapter 3. Hole 6, Hole 7, Hole 15, Hole 37 and Hole 38 had 91.5%, 89%, 30%, 1.13% and 4.76% mean coverage area, and a WSS of 0.0022 Pa, 0.0034 Pa, 0.0345 Pa, 0.1144 Pa, and 0.0685 Pa, respectively. The results also indicate that the large majority (>~60%) of side-holes suffer from encrustation, with only a limited number of active side-holes still maintaining their functional role.

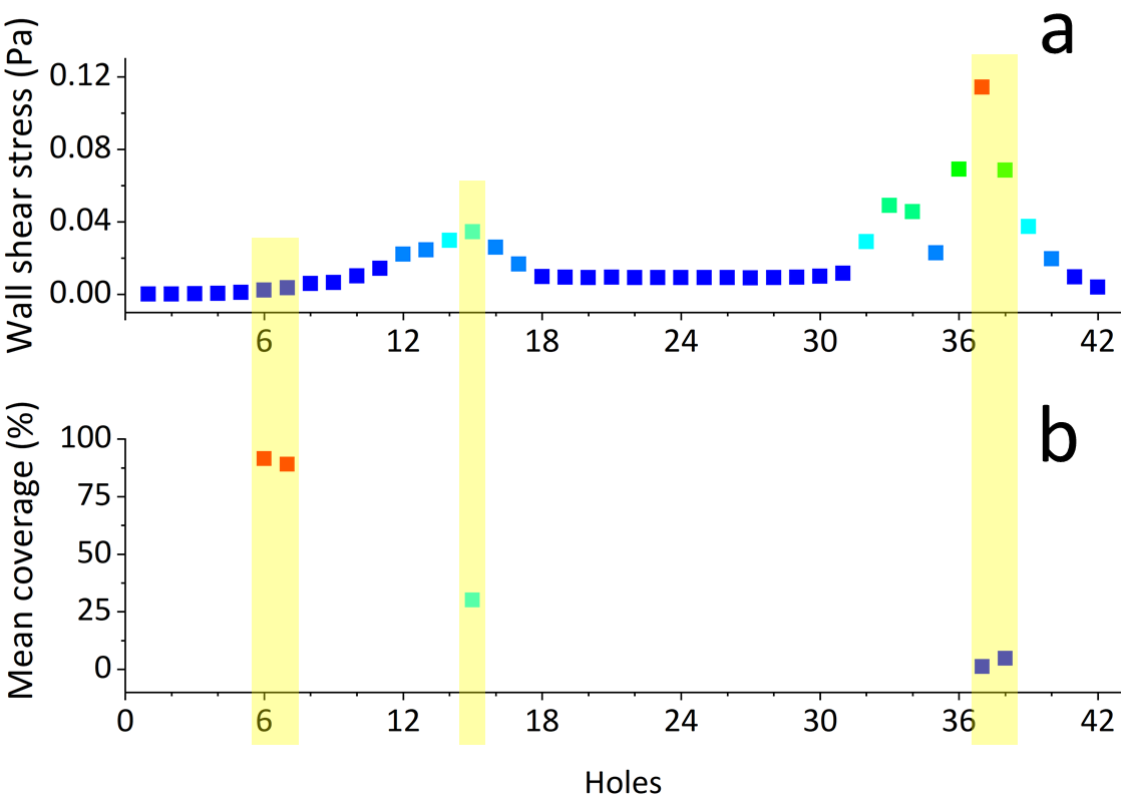

Figure 4-6 (a) Mean values of WSS magnitude (in Pa), calculated numerically, for each individual side-hole (from Hole 1 to Hole 42). (b) % coverage area occupied by encrusting bodies, at specific regions of interest within the model (i.e. Hole 6, Hole 7, Hole 15, Hole 37, and Hole 38).

Figure 4-7 shows quantitative values representing the mean % area covered by encrusting bodies, reported as an average over three spatial domains of the model: proximal, middle and distal. Notably, an inverse correlation was demonstrated between the WSS at side-holes and the % encrusted area, coherently with the findings reported in Chapter 3. Proximal, middle and distal domains had 86.87%, 7.67% and 3.16% coverage area, respectively, and a mean WSS of about 3.44e-5 Pa, 0.03452 Pa, and 0.11437 Pa, respectively. This demonstrates that the proximal region of the stent is significantly more susceptible to deposition of encrustation compared to the distal region.

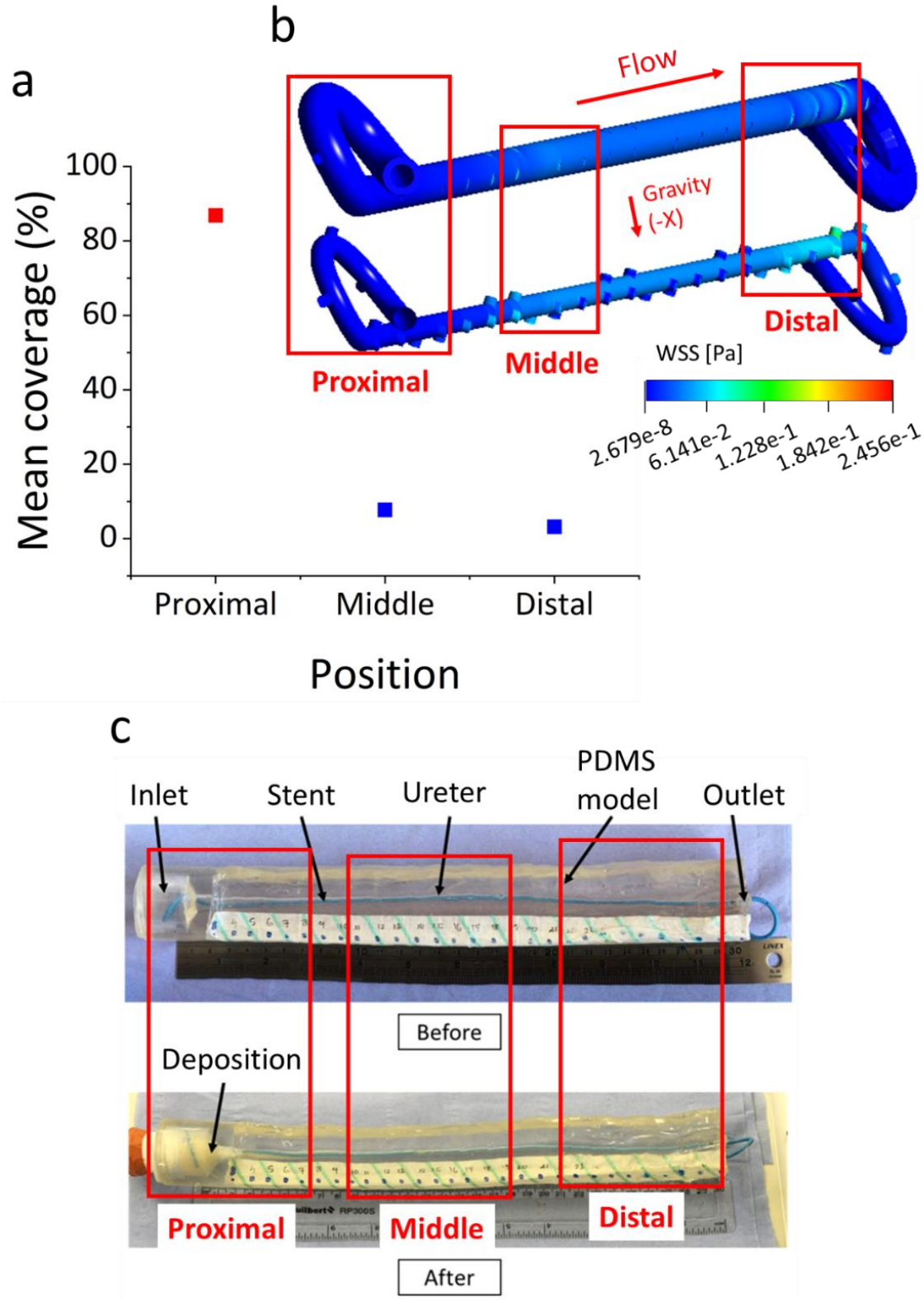

Figure 4-7 (a) the mean % coverage area occupied by encrusting bodies, at specific global regions (or domains) of interest within the model (i.e. proximal, middle, and distal). (b) The top view of the model before and after encrustation experiments. Red boxes indicate the regions of interest over which the mean % encrusted area was taken.

In conclusion, the results of this first part of the study provided a full-scale verification of the inverse correlation between WSS magnitude (determined from CFD simulations) and the deposition of encrusting bodies. This provides confidence in employing the CFD model to investigate different hydrodynamic conditions or architectural properties of the ureter or stent. In the next section, the flow dynamic field in an occluded model of the stented urinary system is investigated.

4.4.2 Occluded (O) model: simulations

The CFD model was employed to investigate the effect of a ureteric obstruction within a stented urinary system, on the WSS field acting over the stent surface. Results are present in the following paragraphs.

Numerical simulations

Figure 4-8 shows the velocity magnitude determined from CFD simulation in the occluded (NO) stented ureter model along the model mid-plane. Similarly to the unoccluded model, results demonstrate higher velocity magnitude in side-holes located at the distal segment of the model, i.e. in the vicinity of the bladder (i.e. 7.99389 mm/s, 7.13489 mm/s, 2.5558 mm/s, 11.0577 mm/s, 18.9105 mm/s for Hole 33, Hole 34, Hole 35, Hole 36, Hole 37, respectively) compared to those located at the proximal segment of the model, i.e. in the vicinity of the kidney. Higher velocity in side-holes before and after obstruction was observed (i.e. 0.8989 mm/s, 1.5063 mm/s, 4.3706 mm/s, 6.8048 mm/s, 17.0785 mm/s, 27.4882 mm/s, 22.2096 mm/s, 11.7042 mm/s, 0.5487 mm/s, 2.7181 mm/s, 3.4678 mm/s for Hole 5, Hole 6, Hole 7, Hole 8, Hole 9, Hole 10, Hole 11, Hole 12, Hole 13, Hole 14, Hole 15, Hole 16 respectively). Results thus confirm that there is a higher degree of fluid exchange rate through side-holes located in the vicinity of the obstruction (before and after) allowing the urine to by-pass the source of obstruction, and also in the vicinity of the narrowing of the ureter lumen located nearby the VUJ.

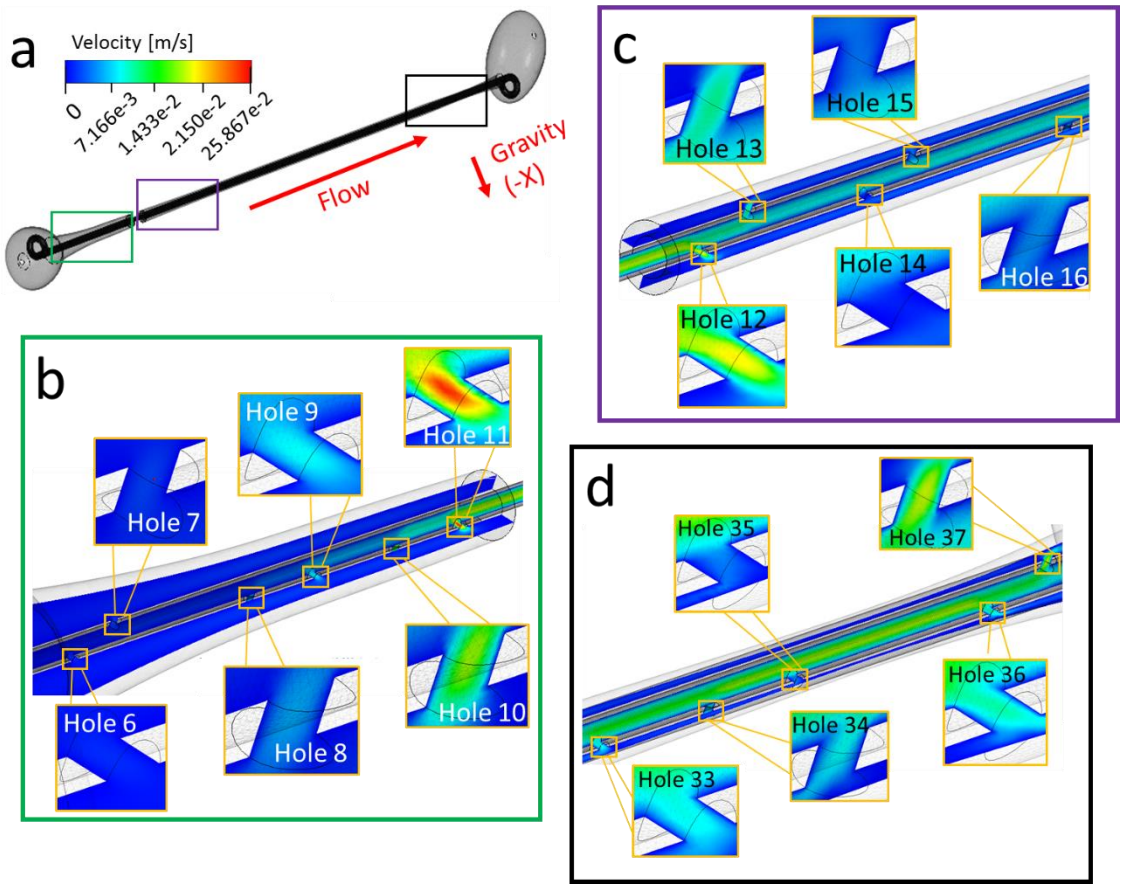

Figure 4-8 (a) Contours of velocity magnitude (in m/s) along the whole model, computed numerically over the model mid-plane. Insets show zoomed-in views of the contours of velocity magnitude at different regions along the ureter (from proximal to distal). These include (b) Holes 6-11, (c) Holes 12-16, and (d) Holes 33-37. Both intra- and extra-luminal compartments nearby a side-hole are shown. Results refer to the occluded (N) model.

Figure 4-9 shows the spatial distribution of WSS magnitude in the occluded ureter model, determined from numerical simulations, and plotted over the stent internal wall (SIW). Results demonstrate that the lowest WSS magnitude is at the lateral walls of side-holes located in the kidney pelvis (e.g. 7.07163e-5 Pa, 2.57285e-4 Pa, 5.59648e-4 Pa, 0.00104 Pa on Hole 1, Hole 2, Hole 3 and Hole 4, respectively). This is coherent with earlier studies showing enhanced encrustation at the proximal coil of the stent [45]. The WSS over both the SIW and side-holes significantly increased from Hole 6 to Hole 18 (located before and after the obstruction) within the range between 0.00517 Pa and 0.16528 Pa. It then reduced to about 0.00954 Pa – 0.00987 Pa until Hole 31, and increased only in the more distal region (e.g. WSS was equal to 0.04893 Pa, 0.04537 Pa, 0.02282 Pa, 0.06878 Pa and 0.11407 Pa in Hole 33, Hole 34, Hole 35, Hole 36 and

Hole 37, respectively). The distal coil of the stent also suffered from low WSS levels. The box plot in Figure 4-9c shows that the maximum, minimum and mean WSS magnitude over the SIW were 0.19461 Pa, 0.00003 Pa, and 0.02344 Pa, respectively. WSS and velocity distributions confirm that holes characterised by inter-compartment flow exchange (referred to as 'active' holes) experience higher levels of WSS, coherently with the microfluidic findings outlined in Chapter 3 and with the full-scale simulations on the non-occluded model. Flow exchange occurred in regions of the model that were characterised by a reduction of the ureter lumen, and particularly in proximity to the obstruction and the VUJ. Notably, the large majority of side-holes experienced WSS levels that are anticipated to favour significant deposition of encrusting deposits (based on the results reported in Chapter 3). WSS values are also in the range of those obtained in the stent-on-chip models previously reported.

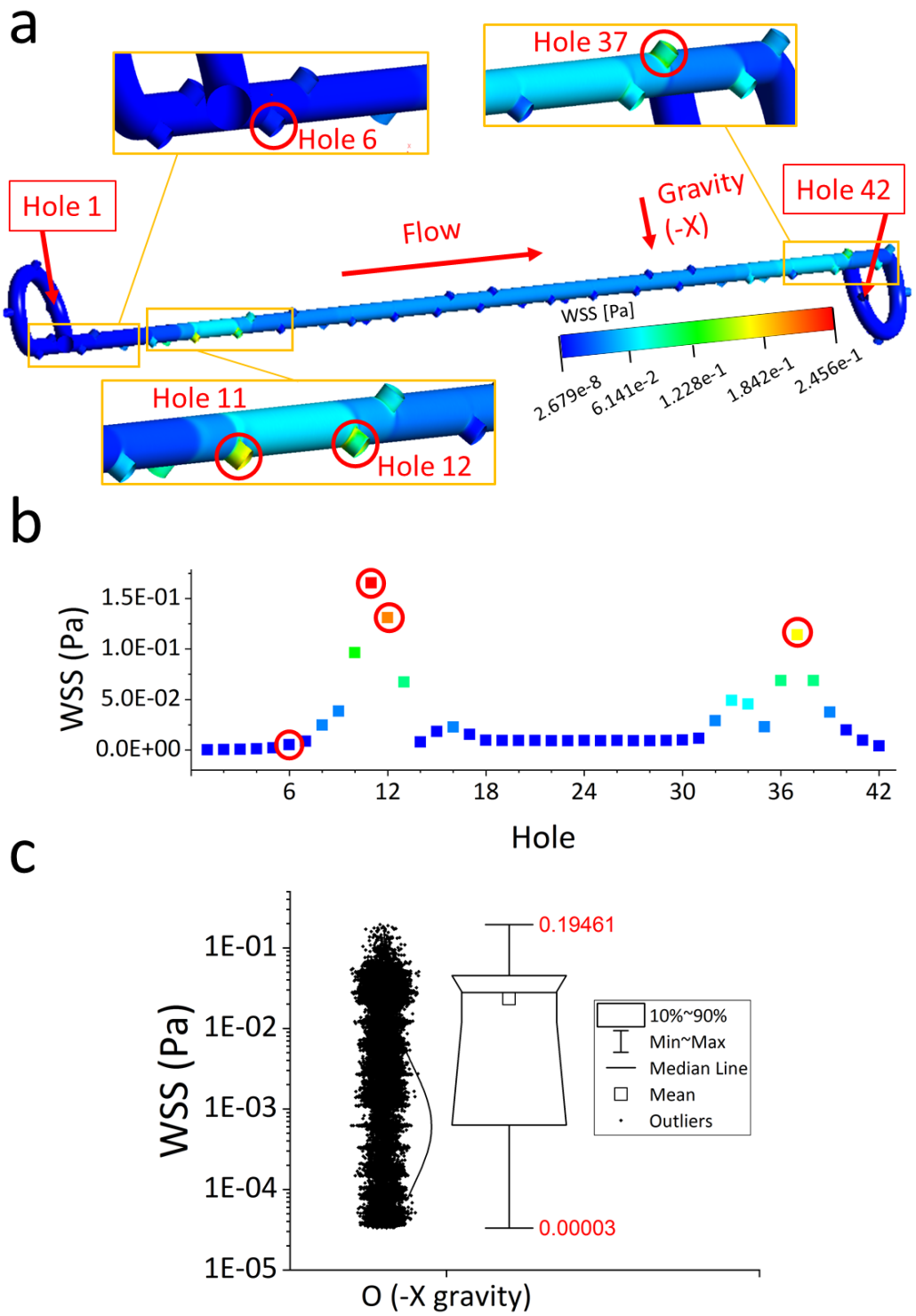

Figure 4-9 (a) Contours of WSS magnitude (in Pa) over the stent internal wall (SIW), computed numerically, as well as zoomed-in views of WSS contour for both proximal and distal regions (O model). (b) Mean values of WSS magnitude (in Pa) calculated numerically for each individual side-hole, from Hole 1 to Hole 42. (c) Distribution of WSS values over SIW reported in the form of a box plot, covering the ranges of 10%, 25%, 50%, 75% and 90% of the total distribution. Additionally, individual data points are

reported next to the box plot. The minimum, maximum, and mean values of WSS magnitude are highlighted in red, next to the corresponding whisker and pointer location in the box plot.

The stent external wall (SEW) was subsequently evaluated. Figure 4-10 shows the spatial distribution of WSS magnitude over the SEW, in the occluded model, together with a box plot to illustrate the distribution of WSS values. The maximum, minimum and mean WSS magnitude along the SEW were 0.1788 Pa, 1.9376e-6 Pa, and 0.1269 Pa, respectively. As observed in the non-occluded model, values were lower than those acting over the internal wall of the stent, at corresponding locations (Figure 4-8a). Results suggest that, in the non-occluded model, the external surface of the stent may be more susceptible to deposition of encrusting particles.

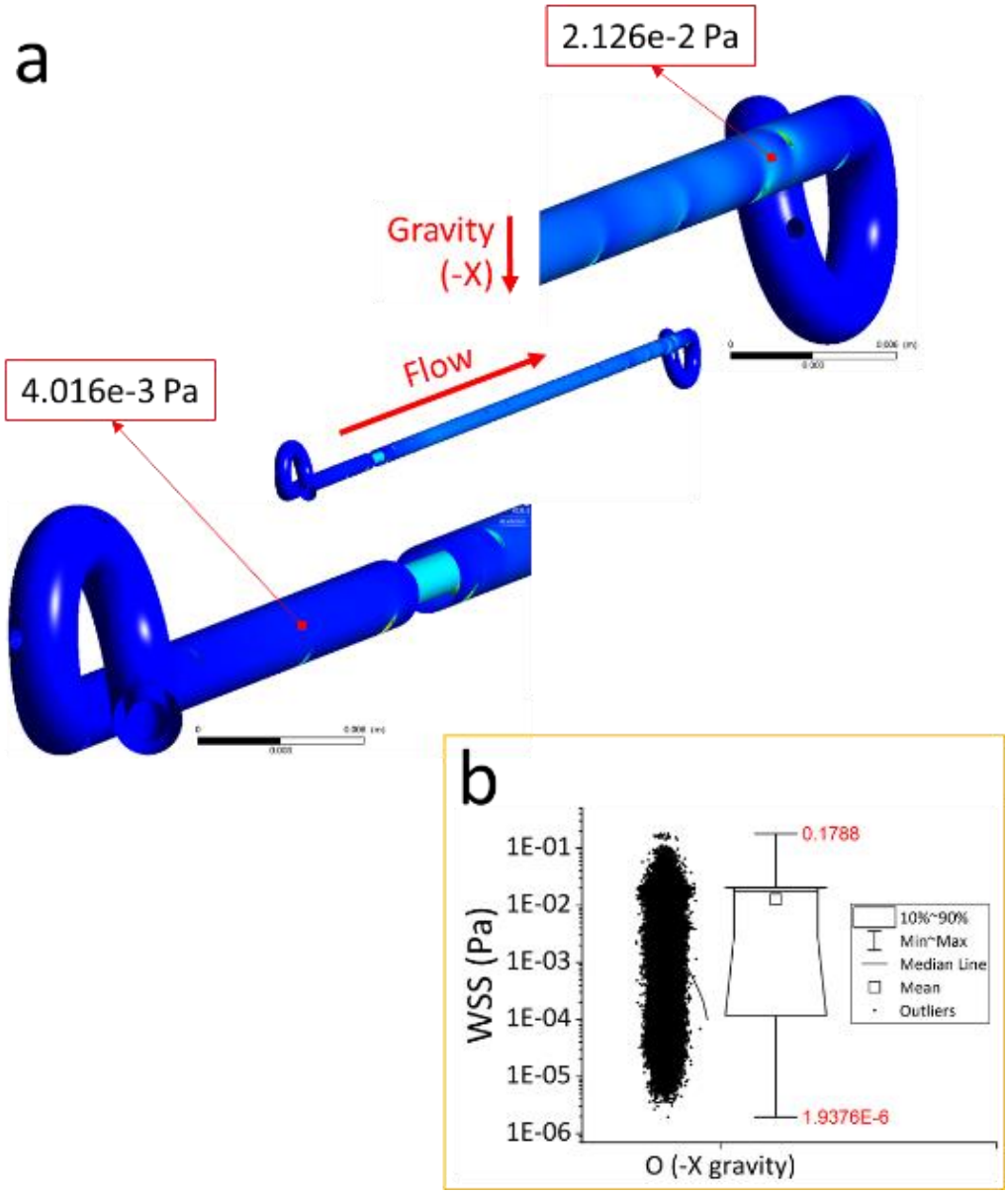

Figure 4-10 (a) Contours of WSS magnitude (in Pa) over the stent external wall (SEW), computed numerically, as well as inset zoomed-in views of WSS contour at both the proximal and distal regions (O model). (b) Distribution of the WSS values over the SEW, reported in the form of a box plot covering the ranges of 10%, 25%, 50%, 75% and 90% of the total distribution. Additionally, individual data points are reported next to the box plot. The minimum, maximum, and mean values of WSS magnitude are highlighted in red, next to the corresponding whisker and pointer location in the box plot.

4.5 Conclusions

Both *in-vitro* experiments and CFD simulations conducted in this study highlighted the correlation between wall shear stress over a stent and the deposition of encrusting crystals. Results also confirmed that the majority of side-holes suffer from low WSS, and are thus prone to the deposition of encrusting bodies.

Moreover, side-holes with higher WSS were those characterised by inter-compartmental fluid exchange. These were located either nearby ureteric obstructions, or in regions characterised by a reduction of the ureter lumen (i.e. close to the VUJ). Results from this study thus support the microfluidic observations, which revealed that side-holes proximal to the occlusion experienced lower encrustation rates due to the higher WSS in these regions.

In summary, this study confirms the underlying hypothesis of this research and the findings reported in Chapter 3. It also supports the ability of SoC models to replicate key hydrodynamic features of a stented and occluded ureter, and thus their utility as a platform for investigating future stent design modifications.

Chapter 5 Decreasing deposition of encrusting particles in stents using material- and coating-independent designs

5.1 Outline

As described in Chapter 3, an inverse correlation has been identified between WSS and deposition rates of encrusting particles in models of the occluded and stented ureter. Based on this correlation, critical regions of the stent prone to the accumulation of encrusting particles have been identified, including 'inactive' side-holes and the cavity formed by a ureteric occlusion. Obstruction of side-holes due to encrustation is particularly critical to the functioning of the stent, since side-holes provide a path for urine to by-pass the occlusion. This Chapter thus investigates changes to the architecture of the stent, with the aim of increasing WSS within inactive side-holes and improving the overall drainage performance of the stent. Changes included modifications to (i) the stent's thickness and (ii) the shape of the side-hole. The stent's thickness was varied in the range 0.3-0.7 mm, whilst streamlined side-holes of triangular shape were evaluated, with vertex angle in the range 45-120°. Reducing the thickness of the stent increased the WSS (and thus reduced encrustation rates) within side-holes. A further improvement in performance was achieved using side-holes with triangular shape; holes with a 45° vertex angle showed superior performance compared to the other angles investigated, resulting in a significant increase in WSS within 'inactive' side-holes. In conclusion, by combining the optimal stent thickness (0.3 mm) and hole vertex angle (45°) resulted in a ~90% reduction in encrustation rate within side-holes and the occluded cavity, compared to a standard design. If translated to a full-scale ureteric stent, this optimised architecture has the potential for significantly increasing the stent's lifetime.

5.2 Introduction

Several studies have investigated strategies for reducing the rate of encrustation and biofilm formation over the surface of ureteric stents. As discussed in the earlier chapters, these studies mainly focused on the bulk or surface material properties of stents, i.e. by changing the constitutive materials or chemically functionalising their surface. Some attempts have also been made to alter the design of the stent with the aim of improving urine drainage; i.e. by introducing surface grooves or changing the shape and size of the stent lumen [75, 105]. There is however, a

limited understanding of how - and to which extent - flow dynamics governs encrustation within the stented ureter [49, 75, 172]. This has often hindered the translation of new designs into the clinical environment. Moreover, the architectural complexity and high fabrication costs of novel designs often limit their adoption from stent manufacturers.

In Chapter 3, it was demonstrated that fluid dynamics (and especially wall shear stress) is correlated with the deposition rate of encrusting bodies. Critical regions of the stent suffering from low WSS, and thus prone to the accumulation of encrusting particles, were also identified. These included 'inactive' side-holes and the cavity formed by a ureteric occlusion, coherently with earlier investigations [41, 165]. These findings were qualitatively confirmed on a full-scale, using an artificial model of the stented ureter, showing that the large majority of side-holes in a stent suffer from low WSS levels (as reported in the Chapter 4).

Obstruction of side-holes due to encrustation is particularly critical to the functioning of the stent, since (i) side-holes provide a path for urine to by-pass the occlusion, and (ii) flow exchange through side-holes can reduce the pelvic pressure, by increasing the effective hydraulic diameter of a stented ureter system.

Thus, the aim of the present chapter is to investigate means for improving the hydrodynamic performance of the stent, with a particular focus on increasing the WSS within inactive side-holes. The stent-on-chip platform described in Chapter 3 will be utilised here as a design tool to iterate changes to the stent architecture, and compare their efficacy with a standard design. Architectural changes will be limited to those that can be easily implemented on a full-scale stent, at relatively low-cost. In particular, the thickness of the stent and the shape of its side-holes will be altered, and an optimal combination of the two identified.

Being independent from the material and surface properties of the stent, the developed stent design could be employed as an adjuvant strategy against encrustation to further improve the efficacy of current approaches.

5.3 Materials and methods

The design and fabrication of SoC models have been detailed in Chapter 3. In the present study, these models are employed as a platform to evaluate the effect of different side-hole shapes on the fluid exchange between intra- and extra-luminal compartments of a stent. In the first part of the study, changes in the size of the septum separating intra- and extra-luminal compartments were investigated, where the septum is employed as a model of the stent's wall. Upon

identification of an optimal wall thickness, different side-hole shapes were subsequently investigated.

A similar statistical analysis approach to the one described in Chapter 3 was employed in this section of the study. Briefly, the experimental data are presented as the mean ± standard deviation. Differences between particle deposition in Hole 1, Hole 2, and Cavity (for occluded SoC) were evaluated using an unpaired Welch's *t*-test. The correlation between the parameters of time and mean coverage area was evaluated by conducting a linear regression analysis. Rstudio (RStudio®, USA) and XLSTAT (XLSTAT®, USA) software were used to conduct the analyses. The null hypothesis statement was "the data are the same and there is no difference between them", while the alternative hypothesis statement was "A series of data has a lower value than the other". The significance level (Alpha) was set to 0.05 (i.e., differences were considered to be statistically significant for $P < 0.05$). Additionally, a Kolmogorov Smirnov test (KS-test) was employed to evaluate the significance of the effect of flow rate (in Hole 1, Hole 2 and Cavity) for a fixed SoC design, and to statistically evaluate the significance of the effect of stent design (in Hole 1, Hole 2 and Cavity) for a fixed flow rate.

5.3.1 Stent-on-Chip (SoC) models: design rationale

The SoC model used in this study was designed to replicate relevant hydrodynamic regions of an obstructed and stented ureter. Briefly, the model included two main flow channels mimicking intra- and extra-luminal domains of a stented ureter system, respectively (Figure 5-1). These two channels were separated by a septum, which modelled the stent's wall. The septum contained two side channels connecting the stent's lumen to the extra-luminal compartment, and designed to model side-holes of a ureteric stent. In addition, two reservoirs were positioned at the inlet and outlet of the model. It should be noted that the channel replicating the extra-luminal compartment was not directly connected to the inlet reservoir. The dead end of this channel was designed to model the cavity [165] generated by a complete occlusion of the ureter, where the cavity is distal to the occlusion (see red region in Figure 5-1a). The dimensions of the features described above were defined according to a commercially available double-J stent (Model: Universa®, Cook® Medical, USA).

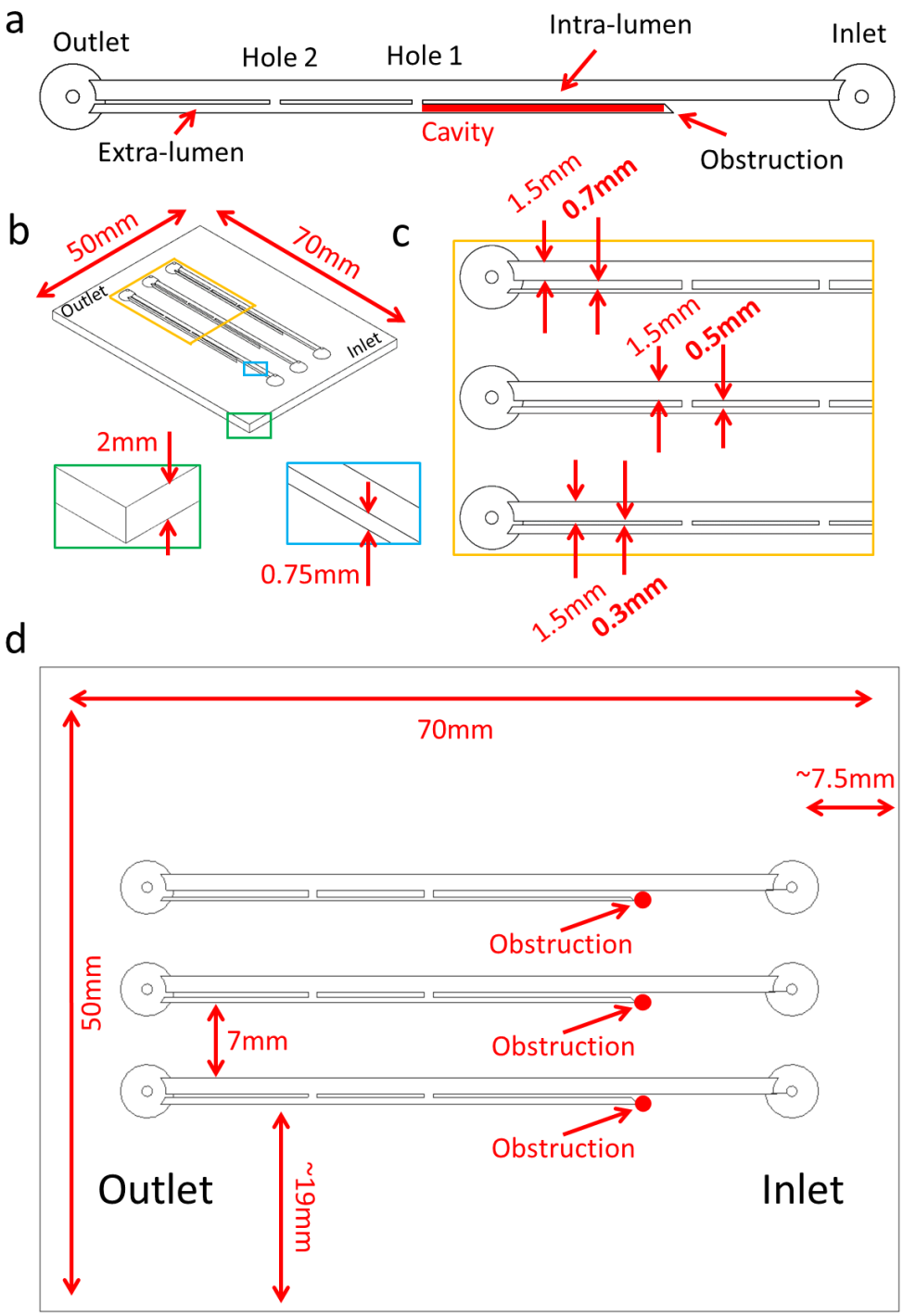

Figure 5-1 (a) Schematic design of the SoC model, illustrating a typical architecture of the model and its relevant hydrodynamic regions (i.e. Inlet, Outlet, Hole 1, Hole 2, Cavity, Intra-/Extra-lumen). (b) Asymmetric view of the SoC device. The blue and green boxes provide a zoomed-in view of the channel height and the SoC base thickness, respectively. The yellow box provides a zoomed-in view of the proximal region of the SoC model. This is illustrated in (c), and comprises models with different septum's thickness (in bold) of 0.3 mm, 0.5 mm and 0.7 mm, and a constant intra-luminal

width of 1.5 mm. (d) Top view of the model, with additional dimensions of relevant features.

5.3.2 Procedures of the study

As outlined in the Introduction section, the rationale behind the present investigation relies on the existence of an inverse correlation between WSS and deposition of encrusting particles over the stent's surface. This has been validated and is described in Chapter 3. It is employed here to inform the design of novel stent architectures capable of reducing encrustation rates. Thus, both numerical CFD simulations and experiments were carried out to determine the distribution of WSS and encrustation within multiple stent geometries, respectively.

The study was articulated into three main phases. In the first phase, simulations and experiments (using artificial urine) were performed on SoC models with three different septum thicknesses, namely: 0.5 mm (which is a stent wall thickness commonly used, and is herein referred to as "standard" or "0.5S"), 0.3 mm (which corresponds to a thinner stent wall currently employed by Boston® Scientific in the USA [49], and is herein referred to as "0.3S"), and 0.7 mm (which corresponds to a thicker stent wall compared to the standard ones [162], and is herein referred to as "0.7S"). The intra-luminal width was kept constant in this first phase of the study. This first series of experimental and computational analyses allowed: (i) the identification of a stent wall thickness resulting in the lowest rate of encrustation; and (ii) validating whether the WSS field obtained from CFD simulations correlated with the distribution of encrustation over the stent walls (even for these different stent architectures). Point (ii) provided confidence that the CFD model could be used as a reliable tool for researching hydrodynamically-optimized stent geometries. Therefore, in a second phase of the study, CFD simulations were used to identify a side-hole shape that reduced the presence/magnitude of stagnant (low-WSS) areas, and consequently decreased encrustation rates. Finally, in a third phase of the study, additional CFD simulations and experiments were performed to quantitatively assess the performance of the new optimized stent design against the standard design (0.5S).

5.3.3 Simulation of the flow field

Numerical simulations were performed to resolve the flow field within regions of interest of SoCs. Modelling parameters and boundary conditions in the numerical model were defined to replicate

the experimental conditions. Following previous studies [173, 176], the inlet volumetric flow rate was set to 1 mL/min.

The device design was initially built using Autodesk® Inventor Pro 2018 (Autodesk®, USA). Then, 3D drawings (in STEP format) were imported into ICEM CFD 18.1 (Ansys Inc., USA), where the fluidic domain was discretised in finite volumes of tetrahedral shape. When defining the numerical mesh, particular attention was devoted to the resolution of the wall shear stress (WSS) distribution over the bottom wall-surface (or bed) of the SoC models. A mesh volume edge length of 0.05 mm was selected as a trade-off between computational cost and solution robustness. Different SoC designs were simulated in this study, and the number of mesh volumes was selected 13,975,780 for the mesh size 0.1 mm (see Figure 5-2). The fluid dynamic field was computed in Fluent® 18.1 (Ansys Inc., USA) by solving for steady-state mass and momentum conservation equations, following the approach described in Chapter 3.

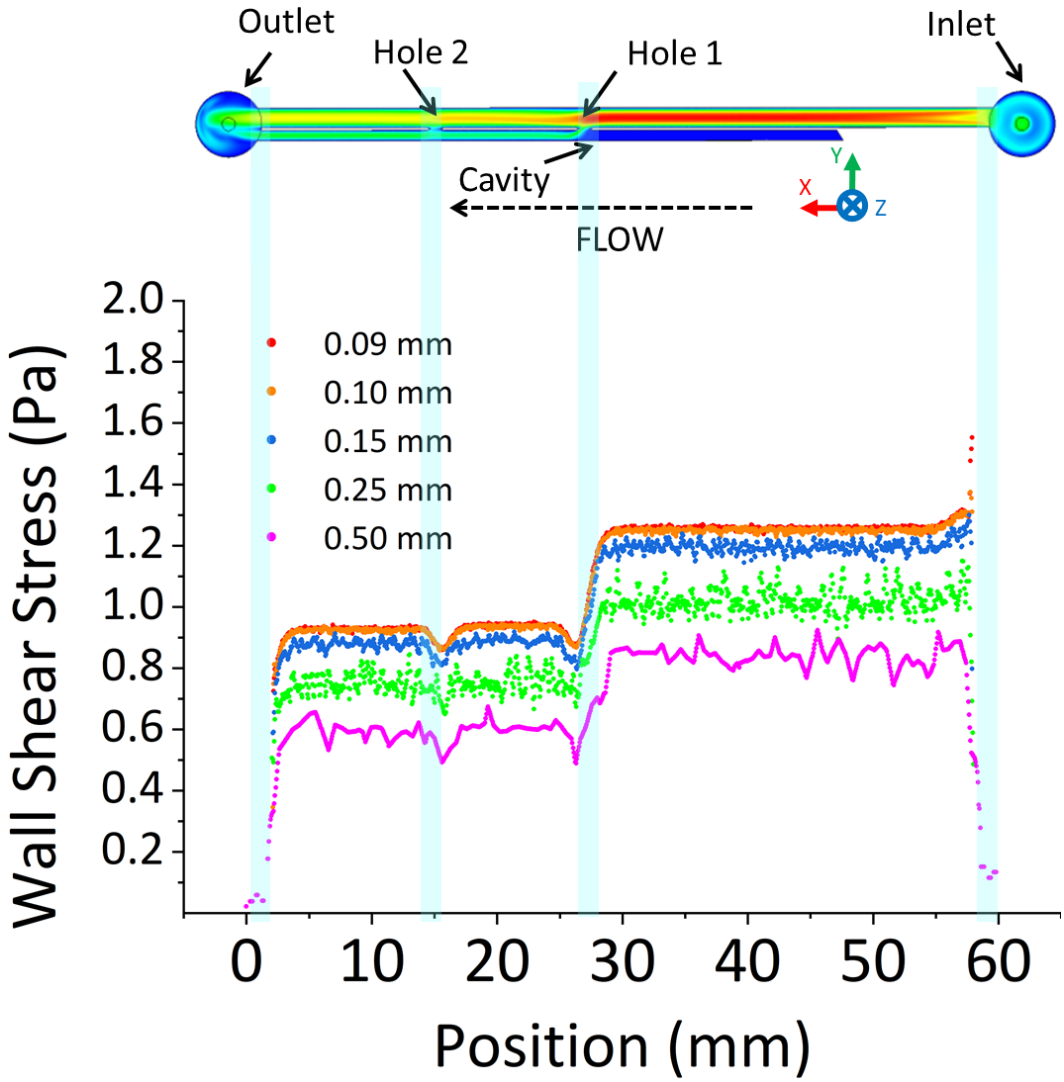

Figure 5-2 Magnitude of shear stress (in Pa) along the wall centreline of the stent compartment (intra-luminal), calculated numerically at different mesh volume sizes, namely 0.09,

0.1, 0.15, 0.25 and 0.5 mm. The light blue lines correspond to the device inlet, outlet and side-holes of the stent. The contour of WSS over the model bottom surface (bed) (i.e., in the z-direction) is also reported (top), in a device with a decreased wall thickness and streamlined side-holes with wall thickness of 0.3 mm and side-hole vertex angle of 45°.

5.3.4 Fabrication of Stent-on-Chip devices and experimental setup

The fabrication of SoC devices used in this study was performed using the μMi-REM procedure described in an earlier publication [195]. Briefly, an epoxy-based positive mould was first created from a milled negative mould, followed by casting of polydimethylsiloxane (PDMS, Sylgard® 184, Dow Corning Corporation, USA) on the positive mould. PDMS was produced using a 10:1 weight ratio between monomer and curing agent. The PDMS sheet containing the channel architecture was then permanently sealed to a microscope glass slide (70 mm × 50 mm, Sigma-Aldrich®, UK), upon treatment with oxygen plasma (plasma asher TePla 300, PVA-TePla®, Germany).

The experimental setup is shown in Figure 5-3; it consisted of two main units:

i. **The fluidic control unit, to deliver a urine surrogate within the SoC models.**

The preparation of the surrogate fluid was carried out following a protocol designed by Keevil *et al.* [175], with minor modifications. Related chemical constituents were supplied by Sigma Aldrich® (UK) and are reported in Table 3-1. The AU solution was kept at 37ºC (under continuous stirring) and pH of 6.8, during experimentation. Tubing (PTFE, Cole-Parmer®, UK) connected the device to a reservoir containing the AU solution, and to a peristaltic pump (Minipuls3, Gilson®, UK) used to pump AU through the microfluidic models (at a physiologically relevant flow rate of 1 mL/min [165, 173, 176]). The experiment was run for 90 minutes, and the SoC device was placed horizontally on the stage of an optical microscope (see below).

ii. **The optical unit for monitoring deposition of encrusting particles *in-situ*.**

An inverted optical microscope (Wilovert 30, Helmut Hund GmbH, Germany) and a CCD camera GXCAM-HICHROMESII (GT-Vision®, UK) with exposure time set to 1 ms, were employed to acquire high-resolution images of encrusting deposits within SoC models. Images were acquired every 15 minutes a were then processed using ImageJ software (NIH, USA), to quantify the time evolution of encrustation at selected locations (Hole 1, Hole 2 and Cavity) within the models. The image processing followed the same procedures described in Figure

3-3b (in Chapter 3), and allowed quantifying the % area occupied by encrusting deposits at selected locations.

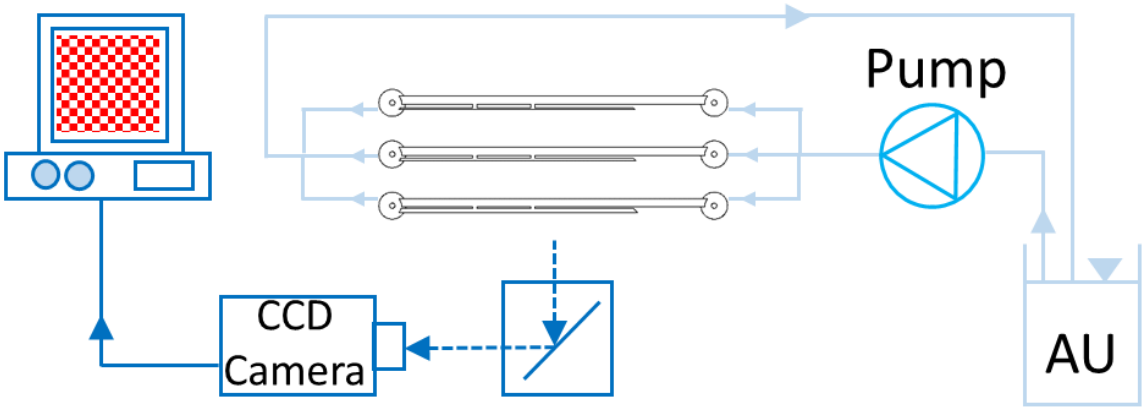

Figure 5-3 Experimental setup employed to analyse deposition of encrusting deposits *in-situ*, within SoC models. It includes a reservoir containing artificial urine (AU), a peristaltic pump (Minipuls3, Gilson®, UK), the SoC device placed horizontally on a microscope (Hund® Wilovert 30) stage, a CCD camera GXCAM-HICHROMESII (GT-Vision®, UK) for capturing microscope images, and a PC for image acquisition, storage and processing.

5.4 Results and discussion

5.4.1 Effects of stent wall thickness

5.4.1.1 Characterisation of the flow field

Figure 5-4 shows the WSS spatial distribution over the bottom-wall (bed) in both Hole 1 and Hole 2, at three different stent wall thicknesses investigated. Hole 2 (i.e. located in proximity to the outlet) was associated with a lower mean WSS (0.0207 Pa, 0.0150 Pa and 0.0102 Pa for wall thicknesses of 0.3 mm, 0.5 mm and 0.7 mm, respectively), as a result of the partially stagnant flow in this region (see dark blue regions in Figure 4-3b). On the other hand, in Hole 1 (i.e. located near the obstruction), the inter-luminal flow exchange caused by the obstruction enforced a significant increase in mean WSS (0.0535 Pa, 0.0295 Pa and 0.0119 Pa for wall thicknesses of 0.3 mm, 0.5 mm and 0.7 mm, respectively). Since the postulated function of side-holes in stents is to promote fluid drainage, we will refer to Hole 1 and Hole 2 as ‘active’ and ‘inactive’ side-holes, respectively.

Results also demonstrated an increase in WSS with reducing the stent wall thickness, in both side-holes, as shown by the WSS spatial distribution reported in Figure 5-4. Importantly, the numerical results in Figure 5-4 were in agreement with the earlier numerical study by Tong *et al.* [188], showing that the first hole right after the obstruction was interested by the largest proportion of inter-compartmental fluid exchange.

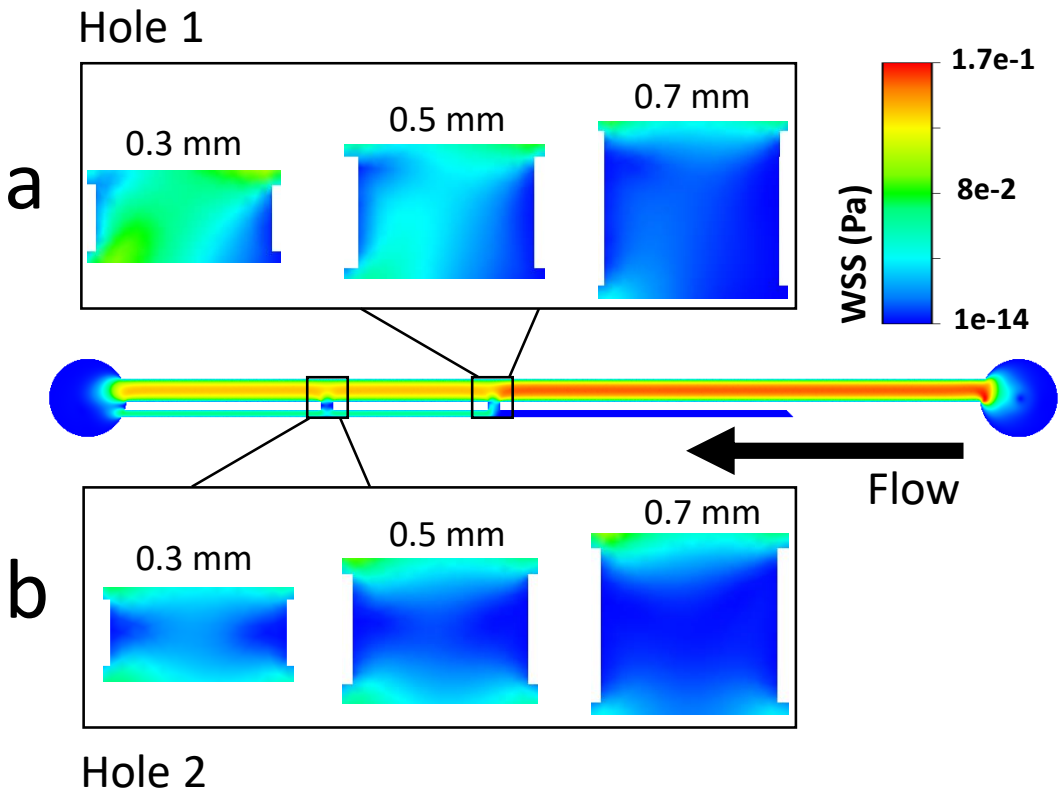

Figure 5-4 Contours of WSS magnitude at (a) Hole 1 and (b) Hole 2, taken at the bottom wall (bed) of the SoC model (i.e., in the *z*-direction), for wall thicknesses of 0.3 mm, 0.5 mm, and 0.7 mm.

Figure 5-5 show box plots of WSS in both Hole 1 and Hole 2, determined from the computational simulations performed on three different stent wall thicknesses of 0.3 mm, 0.5 mm (standard), and 0.7 mm (see Figure 5-1). Results confirm that there are very significant reduction in WSS mean values at Hole 1, when increasing the stent wall thickness; i.e. of 0.7 mm *vs* 0.5 mm ($P < 0.0001$), 0.7 mm *vs* 0.3 mm ($P < 0.0001$) and 0.5 mm *vs* 0.3 mm ($P < 0.0001$). A similar observation was made for Hole 2, when comparing WSS for different wall thicknesses; i.e. 0.7 mm *vs* 0.5 mm ($P < 0.0001$), 0.7 mm *vs* 0.3 mm ($P < 0.0001$), and of 0.5 mm *vs* 0.3 mm ($P < 0.0001$).

Additionally, the mean WSS *vs.* stent wall thickness for both Hole 1 and Hole 2 (Figure 5-5) revealed that the active Hole 1 was affected by changes in the wall thickness to a greater extent, when compared to the inactive Hole 2. This is likely due to the absence of flow exchange through the more distal ('inactive') Hole 2, which reduces its sensitivity to changes of the global architecture of the stent.

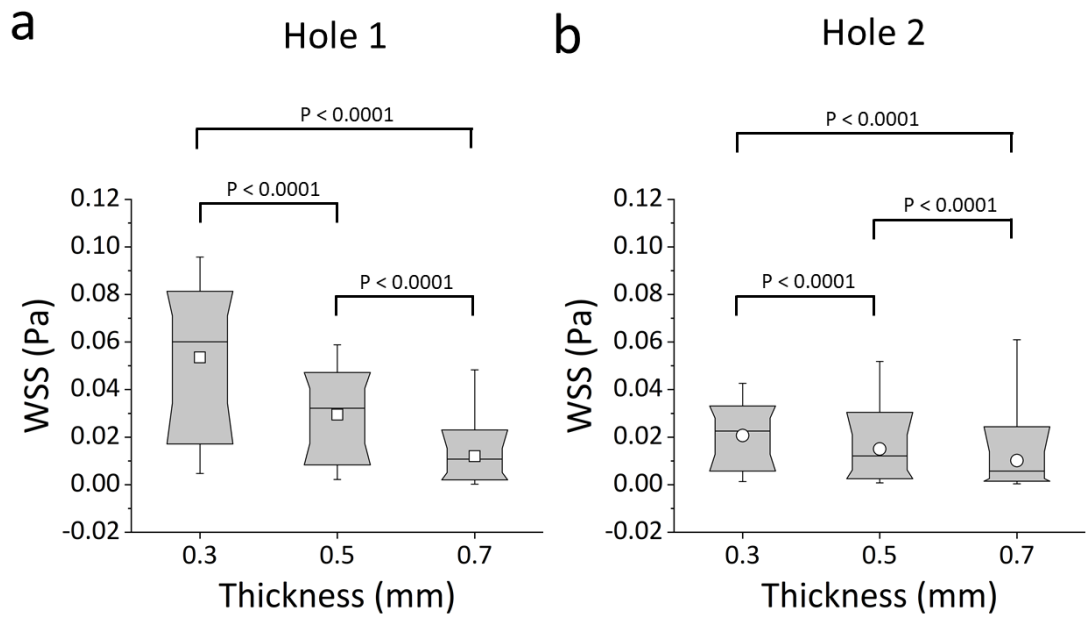

Figure 5-5 Box plots showing the distribution of WSS values (in Pa) over (a) Hole1 and (b) Hole2 of the SoC models. Values were calculated numerically at a flow rate of 1 mL/min, for different stent wall thicknesses of 0.3 mm, 0.5 mm, and 0.7 mm. Box plots show the distribution of the WSS over the ranges of 10%, 25%, 50%, 75% and 90% of the total distribution. The empty squares correspond to the mean values. P-values are reported for statistically significant comparisons, determined through a Kolmogorov Smirnov test.

5.4.1.2 Correlation between WSS and deposition of encrusting crystals

Figure 5-6 shows the simulated WSS spatial distribution over the bottom-wall (bed) of the model, compared to the corresponding experimental images showing accumulation of encrusting crystals. The comparison is made over three regions (Hole 1, Hole 2, and Cavity) and for different wall thicknesses (0.3 mm, 0.5 mm, and 0.7 mm). Figure 5-6 reveals an inverse correlation between the WSS field acting over the stent wall and the distribution of encrustation, for most of the experimental conditions investigated. Low levels of encrustation occurred in regions characterised

by high WSS, and vice versa. Deposition of encrusting particles in side-holes initiated at the lateral edges of the hole, where the WSS was lower. Figure 5-6 also confirms that the occluded cavity is a region prone to the deposition and growth of encrusting particles, and this observation applied to all stent thicknesses investigated. These findings are in agreement with the results described in Chapter 3, and with earlier observations by Clavica *et al.* [165] concerning the presence and role of cavity flow in the occluded and stented ureter.

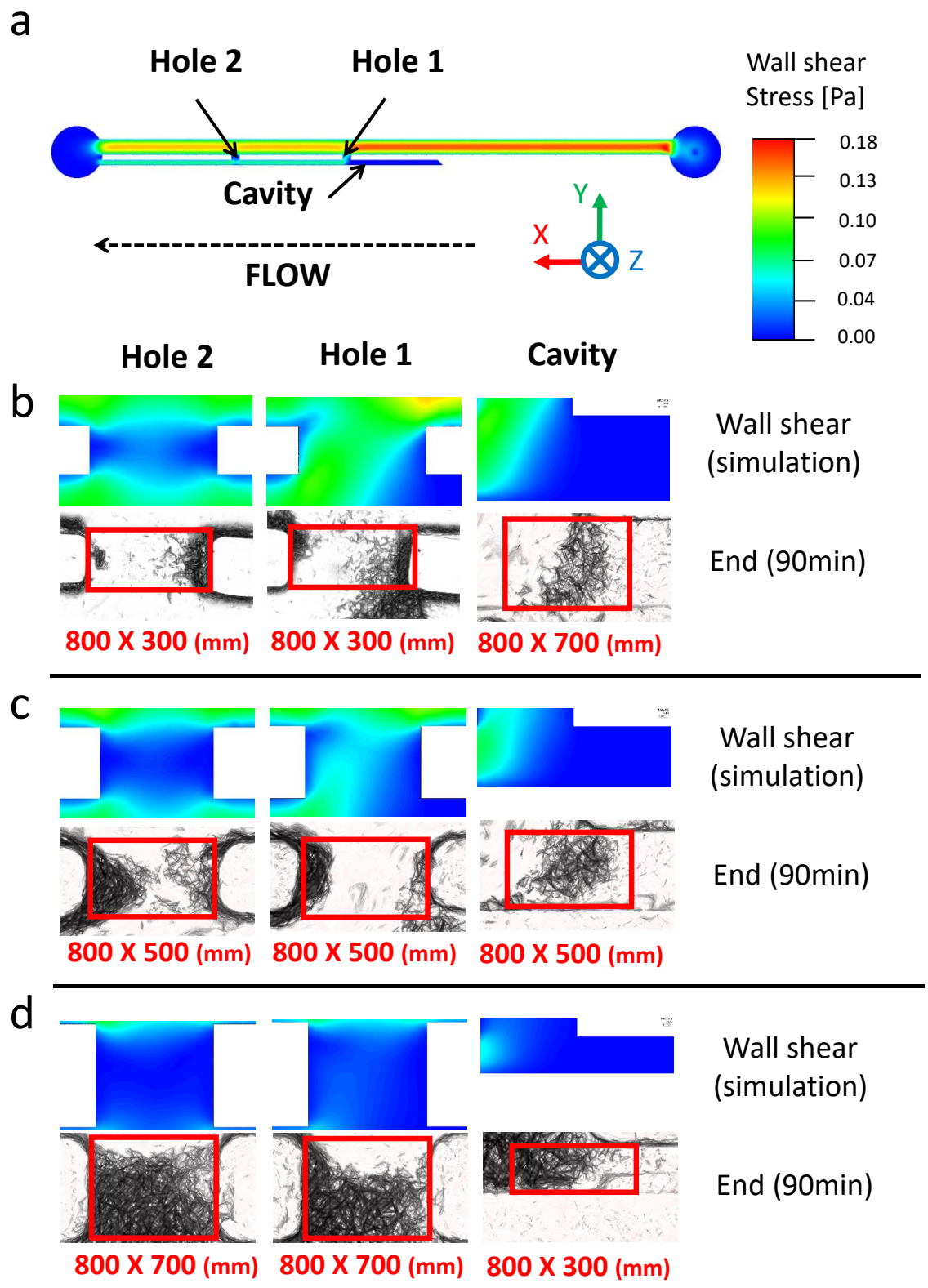

Figure 5-6 (a) Contour of WSS magnitude at the bottom plane (bed) of the SoC model, computed numerically. WSS contours are reported at three hydrodynamic regions within the model (Hole 1, Hole 2, and the cavity), together with the corresponding microscope images showing encrusting deposits, at inlet flow rate of 1 mL/min and wall thicknesses of (a) 0.3 mm, (b) 0.5 mm, and (c) 0.7 mm. Images were taken at 0 min and 90 min from the beginning of the experiment (n = 3). Red boxes (with their size

underneath them, reported as “width × height” in mm) correspond to the regions of interest, over which the % coverage area occupied by encrustation was calculated.

5.4.1.3 Effect of WSS on formation and growth of encrusting deposits in stents

Figure 5-7 reports a quantitative analysis of the level of encrustation over time, within Holes and the Cavity region of the stent, and for the different wall thicknesses investigated. Values were obtained from image analysis, by measuring the percentage area covered by encrusting deposits. The red boxes in Figure 5-6 show the regions over which the % coverage area was calculated, for each wall thickness investigated.

At wall thickness of 0.3 mm, values of Hole 1, Hole 2 and Cavity had mean % coverage areas of 14.1% ± 4.6%, 25% ± 5.2% and 37.5% ± 6.4%, respectively. At a stent thickness of 0.5 mm, values were 42.8% ± 9.5% (Hole 1), 58.7% ± 9.3% (Hole 2) and 73.9% ± 3.7% (Cavity), whilst at a stent thickness of 0.7 mm they were 58.1% ± 10% (Hole 1), 61.5% ± 12.3% (Hole 2) and 66% ± 12.3 (Cavity). Hole 2 and the Cavity regions had statistically lower coverage area at a thickness of 0.3 mm in comparison to a thickness of 0.5 mm (Hole 2: $P = 0.0476$, Cavity: $P = 0.0140$). Meanwhile, coverage area at Hole 1 for a wall thickness of 0.3 mm was significantly lower compared to a wall thickness of 0.7 mm (Hole 1: $P = 0.0315$). Results show that a wall thickness of 0.3 mm exhibited the lowest deposition of encrustation (after 90 min of continuous artificial urine flow), compared to thicker stent walls. Interestingly, at a wall thickness of 0.7 mm, the coverage area was comparable across the different regions investigated (values were 58.1% ± 10%, 61.5% ± 12.3% and 66.1% ± 12.3% for Hole 1, Hole 2 and the Cavity, respectively). This suggests that, at these higher wall thicknesses (> 0.5mm), both ‘inactive’ and ‘active’ side-holes are susceptible to the deposition of encrusting particles, due to the low-WSS levels in both regions of the stent and the % coverage area in these side-holes was not statistically different. (Hole 1 *vs* Hole 2: $P = 0.837$; Hole 1 *vs* Cavity: $P = 0.639$, Hole 2 *vs* Cavity: $P = 0.805$).

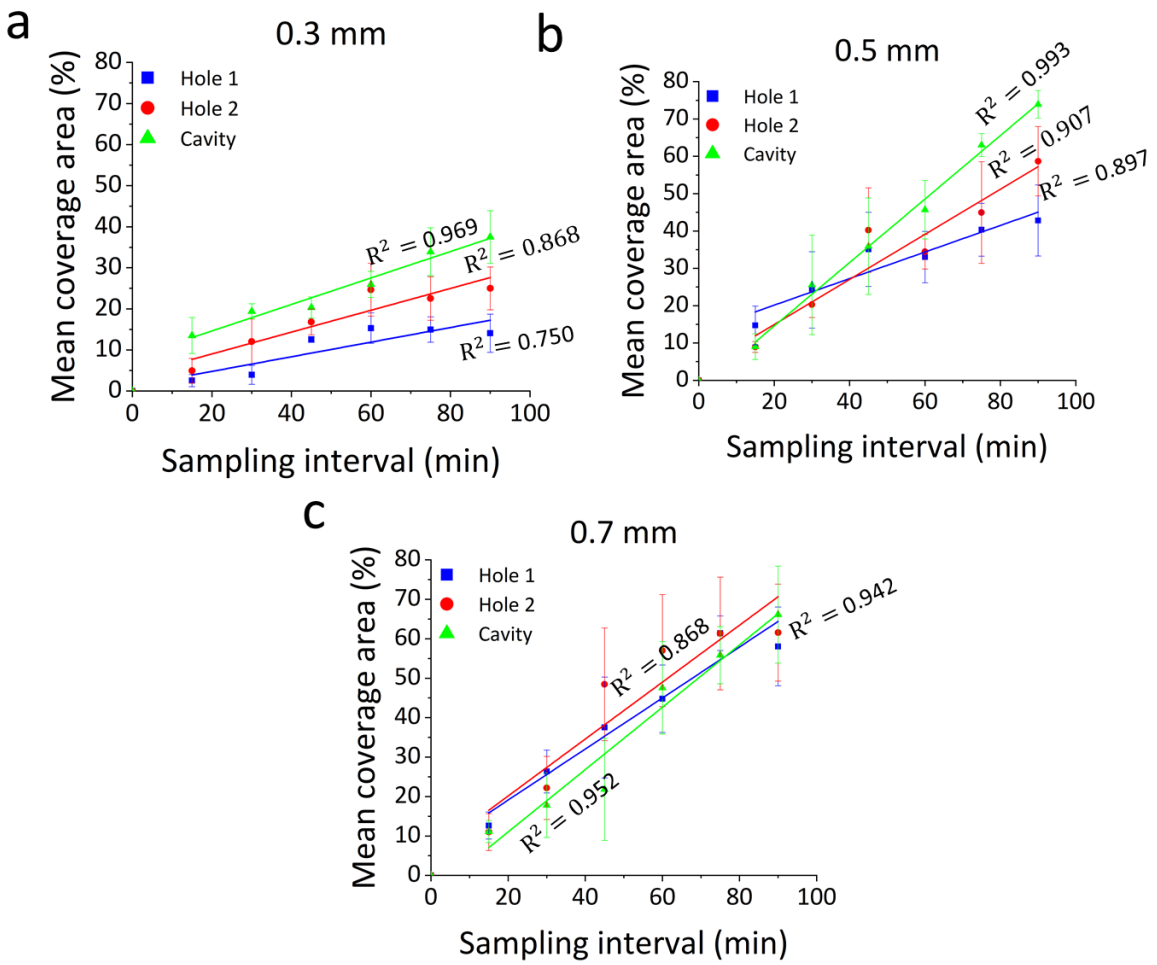

Figure 5-7 Time evolution of the % area covered by encrusting deposits, at specific regions of interest within the models (Hole 1, Hole 2, and Cavity). Results are reported for an inlet flow rate of 1 mL/min, and at three wall thicknesses of (a) 0.3 mm, (b) 0.5 mm, and (c) 0.7 mm. Data are expressed as mean value ± standard deviation of three independent repeats. Linear regression models (for the time interval: 15 min – 90 min) are plotted, together with the corresponding R^2 values.

In conclusion, the results from this first phase of the study indicated that a wall thickness of 0.3 mm allows for enhanced fluid exchange between intra- and extra-luminal compartments of the stent, which, in turn is associated with higher WSS and consequently reduced encrustation rates. Furthermore, as already observed in Chapter 3, WSS fields obtained from CFD simulations displayed a robust and inverse correlation with the distribution of encrusting deposits over the stent wall. This provides confidence in using CFD models to perform hydrodynamic optimization of the stent geometry, as discussed in the next section.

5.4.2 Effects of side-hole shape

The results reported above confirmed that both the occluded cavity and 'inactive' side-holes of the stent are regions prone to the deposition of encrustation, at clinically relevant stent wall thicknesses. Earlier studies have suggested that a large proportion of side-holes in ureteric stents is not interested by inter-compartmental flow exchange and may be obstructed by crystals [183]. Thus, in this section, we will investigate changes to the design of side-holes in order to reduce encrustation rates in these functional regions of the stent.

The validated CFD model described in the previous paragraphs, was initially employed to investigate the WSS field in SoC models with different side-hole shapes. Based upon the results discussed above, a wall thickness of 0.3 mm was selected in this phase of the study, being the most effective in reducing encrustation rate.

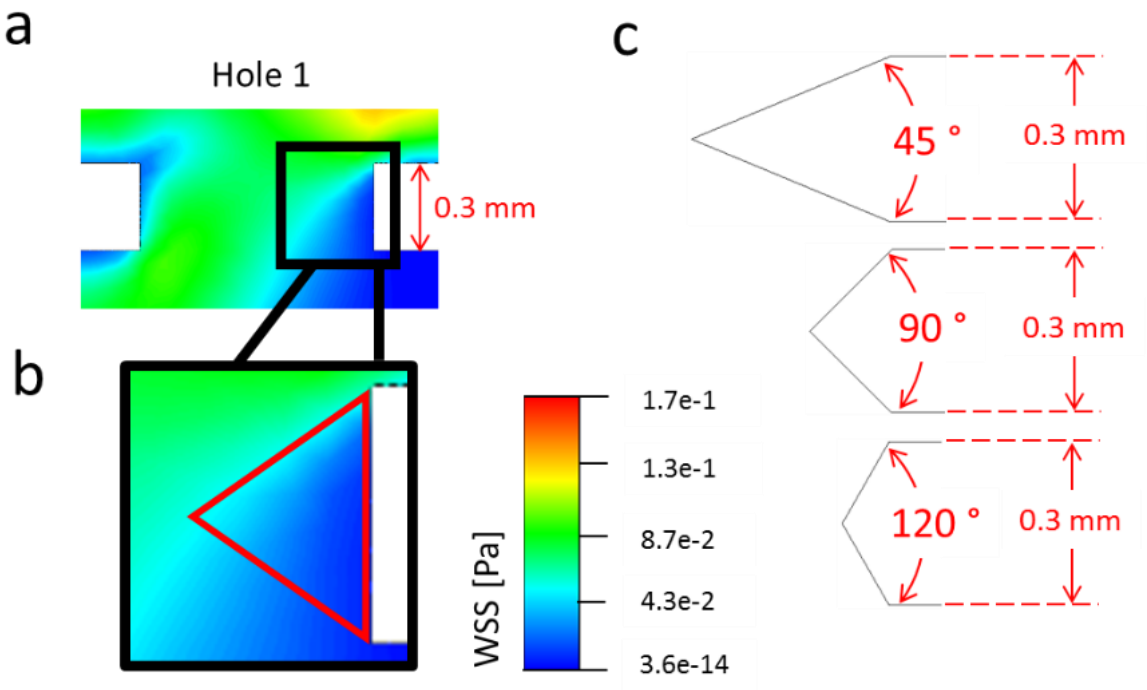

Figure 5-8 (a) Contours of WSS magnitude (in Pa) in Hole 1 of the SoC model, computed numerically at a flow rate of 1 mL/min, for a stent wall thickness of 0.3 mm. The inset in (b) shows a zoomed-in view of the right wall of the hole, with low WSS values represented by dark blue. A red isosceles triangle illustrates a hypothetical side-hole shape. (c) Schematic of different side-hole shapes investigated in this study, each characterised by a different vertex angle of either 45°, 90° or 120°.

5.4.2.1 Simulation of the flow field

CFD simulations performed using a standard side-hole shape (see Figure 5-4) revealed that regions of low WSS (WSS < ~0.02 Pa) within side-holes have an approximately triangular shape. It was therefore hypothesized that 'streamilined' side-holes with a triangular shape could lead to a significant increase of the average WSS, particularly in the more critical 'inactive' side-holes. Side-holes were thus shaped as isosceles triangles, with three different vertex angles (45°, 90° and 120°), as shown in Figure 5-8. Values <45° were proven difficult to manufacture using the micromilling setup employed in this study, and intervals between angles were selected taking into account the specifications of available instruments. For consistency, the width of each hole (i.e. distance between vertex tips in triangular walls) was kept constant and equal to the width of the standard shape (i.e., 0.8 mm). Also, the distance between holes was kept to a constant value of 10 mm.

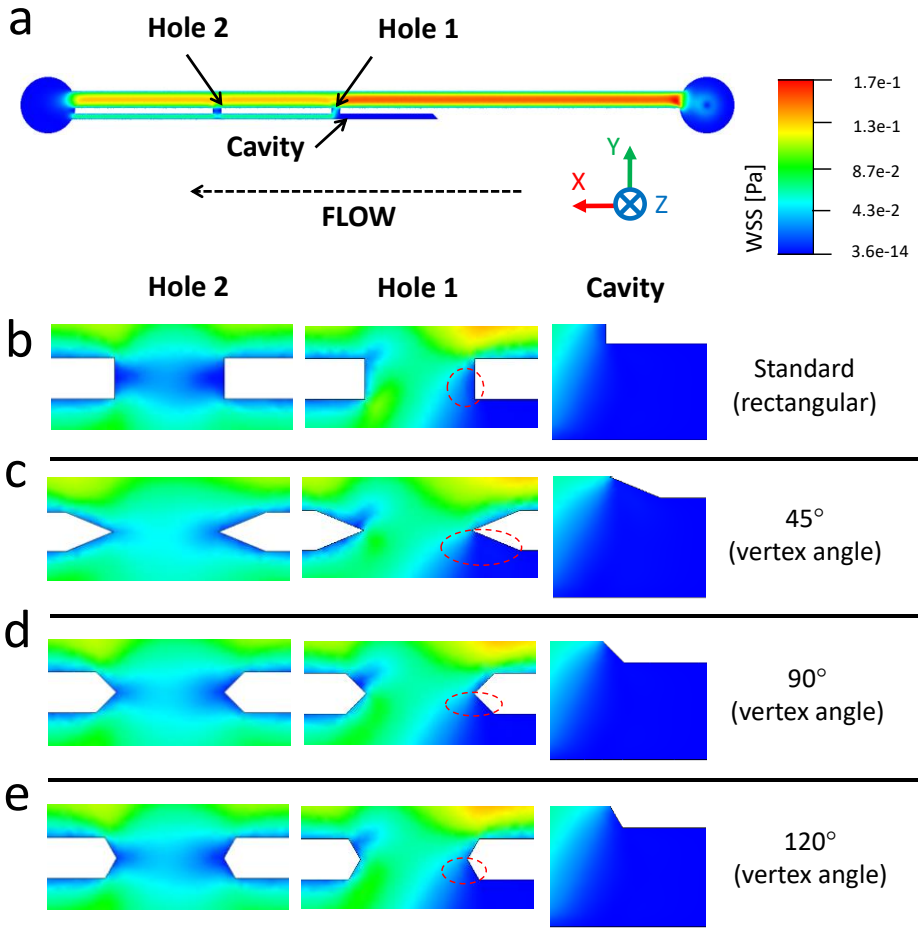

Figure 5-9 (a) Contour of WSS magnitude at the bottom plane (bed) of the SoC model, computed numerically. Contours of WSS are reported at three hydrodynamic regions within the model (Hole 1, Hole 2, and the Cavity), at inlet flow rate of 1 mL/min and vertex angles of (b) 45°, (b) 90°, and (c) 120°. Red dashed circular\oval boxes indicate

stagnant regions with low WSS, located in proximity of side-hole 1 and facing the extra-luminal compartment of the model.

Figure 5-10 shows box plots of WSS calculated numerically, for the standard hole shape (0.3S), and the three aforementioned triangular shapes having vertex angles of 45° (0.3N45), 90° (0.3N90), and 120° (0.3N120). As shown in the figure, the triangular geometries provided a clear benefit, in terms of ultering the value of WSS, only for Hole 2. 0.3S provided the lowest median WSS (i.e. 50th percentile) value.Median values of WSS at Hole 2 were equal to 0.02226 Pa, 0.0373 Pa, 0.0331 Pa and 0.0296 Pa for 0.3S, 0.3N45, 0.3N90 and 0.3N120, respectively, and differences between side-hole designs were very statistically significant (0.3S *vs* 0.345N: $P < 0.0001$, 0.3S *vs* 0.3N90: $P < 0.0001$, 0.3S *vs* 0.3120N: $P < 0.0001$).

In Hole 1, the effect of a triangular geometry is slightly detrimental, as the distribution of WSS shifts towards lower values. The median WSS was equal to 0.0601 Pa, 0.0464 Pa, 0.0533 Pa and 0.05635 Pa for 0.3S, 0.3N45, 0.3N90 and 0.3N120, respectively, and differences between side-hole designs were statistically significant (0.3S vs 0.345N: $P = 0.0300$, 0.3S vs 0.3N90: $P = 0.0450$, 0.3S vs 0.3120N: $P = 0.0690$). However, it should be noted that shape optimization is more critical for Hole 2, as side-holes with no inter-compartmental flow exchange are much more numerous in ureteric stents and are more prone to encrustation (as reported in earlier investigations [183]) compared to active side-holes (i.e. located in proximity to obstructions). This is further illustrated in Figure 5-9, where contour maps of WSS are reported for all the geometries investigated. In Hole 1, inter-compartmental fluid exchange is guaranteed regardless of holes' geometry, and WSS values are overall relatively high (mean WSS > 0.04 Pa); this is further demonstrated by the lowest P - values when comparing 0.3S with each individual triangular shape. Conversely, the 0.3N45 design provides a clear improvement in the performance of the 'inactive' Hole 2, with a decrease of the surface area characterized by low WSS (< 0.02-0.03 Pa). Therefore, 0.3N45 was selected as the most promising side-hole architecture and subject to further investigations.

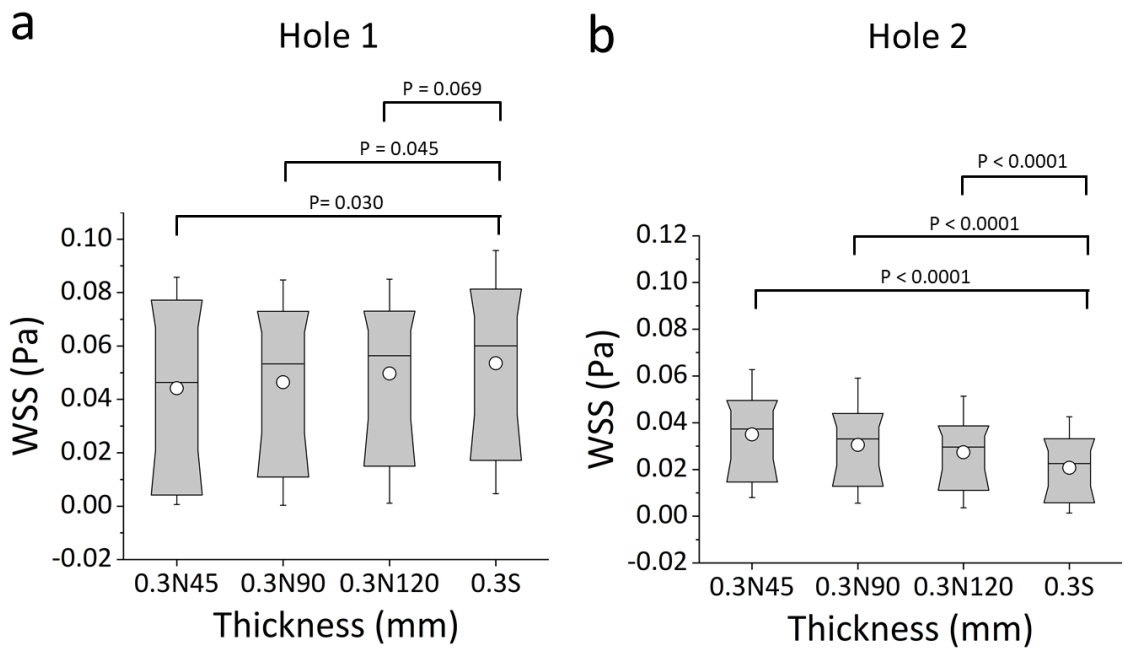

Figure 5-10 Box plots showing the distribution of WSS values (in Pa) over (a) Hole1 and (b) Hole 2 of the SoC models. Values were calculated numerically at a flow rate of 1 mL/min, for a standard side-hole shape (rectangular straight walls) and triangular (isosceles) side-holes with vertex angles of 45° (0.3S45), 90° (0.3S90), and 120° (0.3S120). Box plots show the distribution of the WSS over the ranges of 10%, 25%, 50%, 75% and 90% of the total distribution. The empty squares correspond to the mean values. The statistical significance was determined using the KS-test, and p-values are reported above the box plots.

5.4.3 Standard design ("0.5S") vs. new design ("0.3N45")

5.4.3.1 Simulation of the flow field

Figure 5-11 shows box plots of WSS obtained from CFD simulations of urine flow in both the original stent with standard thickness (0.5S), and the new design combining optimised wall thickness and side-hole shape (0.3N45). The results demonstrate a statistically significant decrease in mean WSS from 0.044 Pa (for 0.3N45) to 0.029 Pa (for 0.5S) in Hole 1 ($P < 0.0001$), and from 0.035 Pa (for 0.3N45) to 0.015 Pa (for 0.5S) in Hole 2 ($P < 0.0001$), corresponding to a % relative rate of 49.8% and 133.4%, respectively.

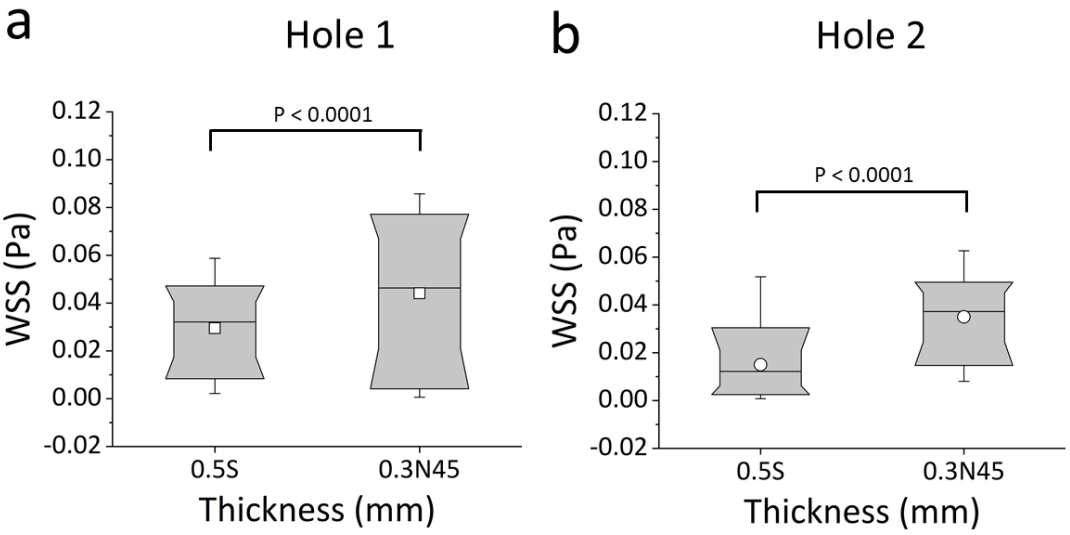

Figure 5-11 Box plots showing the distribution of WSS values (in Pa) over (a) Hole1 and (b) Hole 2 of the SoC models. Values were computed numerically at a flow rate of 1 mL/min, for both the standard stent design (referred to as 0.5S) and the new design (referred to as 0.3N45). Box plots show the distribution of the WSS over the ranges of 10%, 25%, 50%, 75% and 90% of the total distribution. The empty squares correspond to the mean values. The statistical significance was determined using the KS-test, and p-values are reported above the box plots.

5.4.3.2 Correlation between WSS and deposition of encrusting crystals

Figure 5-12 shows the simulated spatial WSS distribution over the bottom-wall (bed) of the model and experimental images of encrustation, both taken at three regions of interest (Hole 1, Hole 2, and Cavity). Experiments again demonstrated a robust, inverse correlation between the simulated WSS field and the accumulation of encrusting particles.

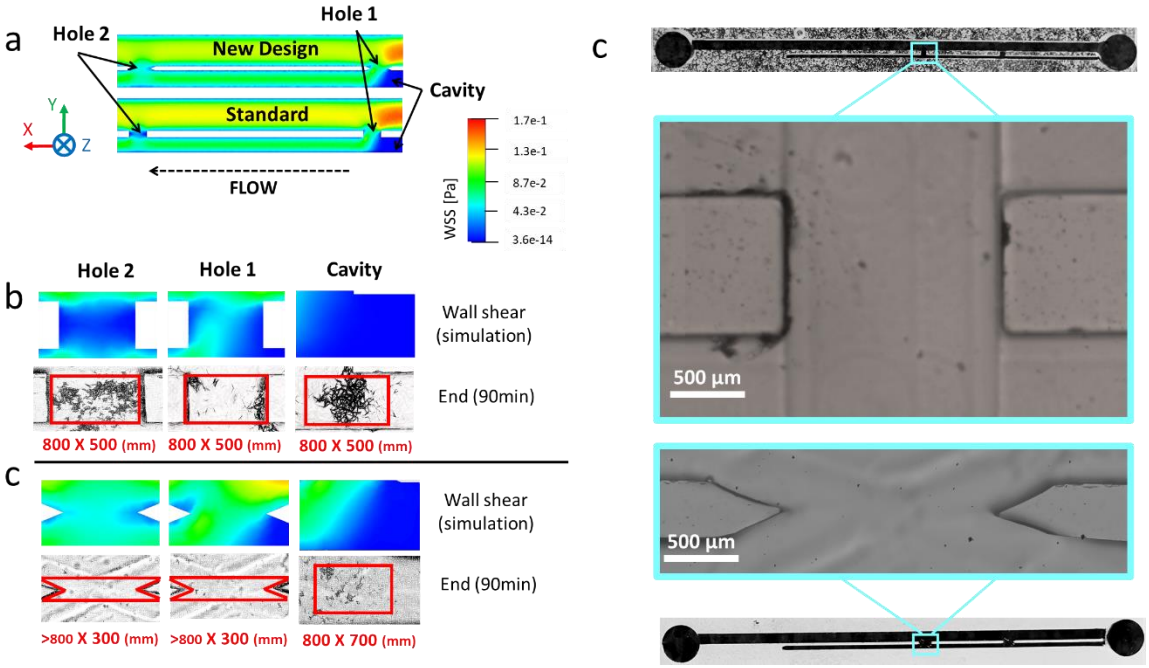

Figure 5-12 (a) Contours of WSS magnitude at the bottom plane (bed) of the SoC model, computed numerically for both standard design and new design. Contours of WSS at three hydrodynamic regions within the model (Hole 1, Hole 2, and Cavity) and corresponding microscope images showing encrusting deposits, at an inlet flow rate of 1 mL/min and for both (b) standard shape (referred to as 0.5S) and (c) new design (referred to as 0.3N45). Images were taken at 0 min and 90 min from the beginning of the experiment (n = 3). Red boxes (with their size reported underneath, as "width × height" in mm) correspond to the regions of interest, over which the % coverage area occupied by encrustation was calculated. (c) Stereozoom top view of the all PDMS microfluidic chip, together with a zoomed-in view of the side-hole for both standard and streamlined designs.

More interestingly, Figure 5-12 shows that the newly proposed stent design is characterized by significantly lower levels of encrustation compared to the standard design, in any region of interest. This significant improvement is further illustrated in Figure 5-13, which shows the time evolution of the % encrusted area in the regions of interest (highlighted in red in Figure 5-12). Results show that both side-holes and the cavity region experienced a drastic reduction of encrusted coverage area in 0.3N45 compared to the standard design (0.5S) (Hole 1: $R^2 = 0.897$, $P = 0.004$, Rate (gradient) = 0.36 min^{-1}; Hole 2: $R^2 = 0.907$, $P = 0.003$, Rate (gradient) = 0.6 min^{-1}; and Cavity: $R^2 = 0.993$, $P < 0.0001$, Rate (gradient) = 0.85 min^{-1}). In particular, in the 0.3N45 design, Hole 1, Hole 2 and Cavity showed a % relative reduction of encrustation of 94.1%, 94.4%, and 86.6%, respectively (Hole 1: $R^2 = 0.933$, $P = 0.002$, Rate (gradient) = 0.02 min^{-1}; Hole 2: $R^2 = 0.984$, P

< 0.0001, Rate (gradient) = 0.03 min^{-1}; and Cavity: R^2 = 0.985, P < 0.0001, Rate (gradient) = 0.01 min^{-1}).

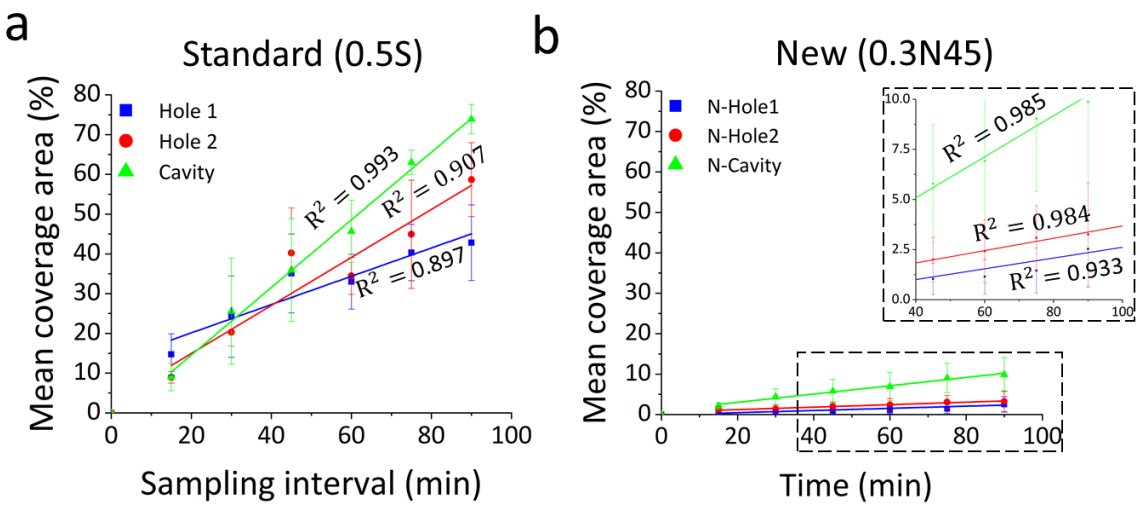

Figure 5-13 Time evolution of the % area covered by encrusting bodies, at specific regions of interest within the models (Hole 1, Hole 2, and Cavity). Results are reported for an inlet flow rate of 1 mL/min, and for both (a) the standard design (referred to as 0.5S) and (b) the new optimised design (referred to as 0.3N45). Experimental data are expressed as the mean value ± standard deviation of three independent repeats. Linear regression models (for the time interval: 15 min – 90 min) are plotted, together with the corresponding R^2 values.

5.5 Conclusions

A SoC microfluidic model was developed as a platform for investigating changes to global (wall thickness) and local (side-hole) architectural features of ureteric stents. A robust and inverse correlation between the local WSS and the rate of deposition of encrusting particles was observed for all geometrical configurations investigated. This confirms our earlier findings, and expands beyond commercial stent geometries.

Notably, by combining both optimal stent wall thickness and hole shape resulted in a major increase in WSS within both 'active' and 'inactive' side-holes and the cavity, causing a significant reduction in the deposition of encrustation in these regions (i.e. relative reduction of 94.1% in Hole 1, 94.4% in Hole 2, and 86.6% in the Cavity).

A potential advantage of our proposed fluid dynamic-based approach against encrustation is in its independence from the bulk material of the stent or surface coatings, which makes it potentially suitable for integration with different clinical or industrial requirements.

In order to validate the performance of the developed stent design under more physiologically relevant conditions, on-going studies are currently being performed in our laboratories using 3D numerical and experimental models. Furthermore, *in-vivo* correlation is required to validate the new designs pre-clinically.

In conclusion, a similar approach against encrustation to the one developed in this study could be potentially applied to other medical devices suffering from similar complications, such as biliary stents [196-198].

However, there is no established method for manufacturing triangular side-holes on ureteric stents, or other tubular medical devices. Therefore, the following chapter will identify and investigate a potential technology to manufacture triangular side-holes, with a specific focus on methods that are simple to perform, cost-effective, and scalable.

Chapter 6 Fabrication of stents with triangular side-holes: first prototypes

6.1 Outline

The present chapter describes the development and characterisation of a first methodological approach towards the manufacturing of ureteric stents containing triangular side-holes. Holes' fabrication was performed on hole-free ureteric stents (obtained from a commercial stent manufacturer), using a milling method developed in-house.

The aim of this study was to evaluate the accuracy and robustness of the method in creating inclined/triangular side-holes through a ureteric stent. Although a vertex angle of 45° provided the best performance against encrustation in the microfluidic-based models (as described in Chapter 4) an angle of 90° was selected in the present study, due to the thickness of the stent being greater than 0.3 mm. A greater vertex angle was thus required to increase the resistance of the vertex tip of the triangle, against deformation during milling. Dimensional and morphological characterisation of the manufactured side-holes was performed, in order to assess the fabrication accuracy and repeatability.

This preliminary study may open new avenues in the manufacturing of stents and catheters containing microscale features, which could potentially expand to include other medical devices with architectural features of comparable shape and dimensions.

The work described in this Chapter was conducted during a Short Term Scientific Mission by Ali Mosayyebi (University of Southampton, UK) at the Artorg Center (University of Bern, Switzerland).

6.2 Introduction

There are different manufacturing processes and technologies that have the potential for fabricating medical devices containing micrometre and/or millimetre sized features [199]. Ureteric stents are currently fabricated following a two-step method: an hollow polymeric tube is first produced *via* extrusion [200], and side-holes are subsequently punched at pre-defined locations along the tube [201]. Manual or automated punching however, does not offer the level of control and the resolution required to manufacture sub-millimetre, triangular side-holes in stents.

A manufacturing method for this specific application should fulfil the following requirements:

a. Ability to create small holes, within the range 500 μm - 800 μm in diameter (as in commercial stents [163]), with fine control over the obtained hole shape;
b. Suitability for usage on thin and flexible tubes, made of polymeric materials (specifically silicone and polyurethane);
c. Should not irreversibly alter the chemical or physical properties of the bulk material of the stent [202];
d. Cost-effectiveness, scalability, and compliance with regulatory requirements [203].

The above criteria limit the range of potentially suitable manufacturing techniques to micro-milling, laser cutting, and water-jet cutting [204]. These are described below, to facilitate the identification of the most appropriate fabrication method.

6.2.1 Micro-Milling

Micro-milling is defined as the mechanical interaction of tools with micron-size cutting grooved tips with a substrate material, resulting in subtraction of a defined amount of material along pre-defined paths [205]. It is largely employed in the fabrication of biomedical microdevices, at relatively low cost and with potential for automation and scaling up [204, 206, 207]. Moreover, it has demonstrated compatibility with different materials, encompassing metals, ceramics, and polymers [208]. A potential challenge associated with milling of flexible elastomers - and of tubular shapes in particular - is the deformation of the substrate during milling. It could however be overcome by a careful selection of the milling tools, spindle speed (especially for smaller features), and supporting material [209].

6.2.2 Laser Cutting

Laser cutting relies on the focusing of thermal energy to a small spot (or around 0.2 mm) on a substrate, in order to vaporise or melt the substrate material with little mechanical stress. There are different types of lasers that differ based on the active medium used for light intensity amplification [210]. Different mechanisms of laser cutting include inert gas melt shearing, reactive gas melt shearing, vaporization, chemical degradation, and scribing [210]. Except for scribing, these methods could be employed on polymeric substrates (including polymeric elastomers). A challenge associated with the use of lasers on polymeric materials is the deformation of the cut zone and the potential melting of material outside the cut zone. These could however be addressed by using a high speed laser, such as a picosecond laser, to reduce unnecessary laser beam interaction with the material [210]. High-speed lasers would however significantly impact on the overall fabrication costs, limiting the scalability of this method.

6.2.3 Water-Jet Cutting

Water jetting uses a high-pressure jet of water in order to cut a substrate along a pre-defined path [211]. It utilises pure water or water containing abrasive particles (to assist cutting of harder materials such as steel) [211, 212]. Compared to other techniques, water-jet cutting is associated with minimal generation of hazardous by-products or fumes [213]. However, cutting holes with diameter smaller than the substrate thickness is challenging; it would require an initial drilling step prior to water jetting, in order prevent the substrate from breaking. This would significantly increase the overall fabrication times and costs.

6.2.4 Selection of the most suitable manufacturing method

Based on the above considerations relating to each candidate fabrication method, and taking into account aspects relating to regulatory approval, access to instrumentation, and ability to customise the experimental setup and vary its functional parameters, micro-milling has been selected as the most suitable manufacturing method.

Therefore, the following sections will describe the development and characterisation of a micro-milling apparatus, which has been customised to generate triangular side-holes through a commercial ureteric stent lumen. It is herein anticipated that a careful selection of the milling tools and operational parameters, together with control over the alignment between milling tool and stent, would provide a platform for creating inclined and triangular side-holes of controlled shape.

6.3 Materials and methods

The following paragraphs describe the materials and methods employed for generating triangular side-holes in a ureteric stent, and their dimensional/morphological characterisation.

It should be noted that this study aims at the manufacturing of triangular side-holes with a vertex angle of 90°, which differs from the optimal 45° angle identified in Chapter 4. This is due to the thickness of the stent being equal to about 0.42 mm, which is greater than the optimal 0.3 mm thickness identified in Chapter 4. A greater vertex angle was thus required to increase the resistance of the vertex tip of the triangle, against deformation during milling. Despite this discrepancy, it is anticipated that a triangular side-hole of 90° vertex angle would still have a beneficial effect on the flow performance of a stent (as discussed in Chapter 4). Moreover, the main aim of the current chapter is to establish a methodology framework for generating triangular side-holes; future adaptations will focus on improving the experimental apparatus towards the manufacturing of stents with different dimensions of their side-holes and lumen.

6.3.1 Milling setup

Hole-free ureteric silicone stents were used as a substrate in this study, and were purchased from a stent manufacturing company (Ningbo GreatCare Trading Co., Ltd., Ningbo, China). A stent with outer diameter of 7 Fr (~2.3 mm), thickness of 0.4 mm (which was the minimum stent thickness available from this manufacturer), and length of 26 mm was employed for conducting this investigation.

In order to avoid undesired deformation (bending) of the stent during milling, a cylindrical core (UL Recognized Appliance Wire Styles E25635, PART NO N303-69-122U, single-conductor thermoplastic (PVC) insulator, Atlas wire LLC, USA) was inserted inside the stent lumen to provide mechanical support. The milling machine used in this study was a Picomax-20 (Fehlmann® AG, Maschinenfabrik, Seon, Switzerland), with a milling tool of 0.65 mm in diameter (Magafor©, France). To cut holes with desired angles, the indexing head on the machine was set to a selected angle that was measured using a protractor. Figure 6-1 shows a schematic of the milling setup (Figure 6-1a) and a photograph of the apparatus (Figure 5-2b), with a zoomed-in view of the supporting material (highlighted with a yellow circle in Figure 6-1b&c). Upon activating the milling machine and waiting until the milling spindle had reached its maximum speed of 10,000 rpm, the milling tool was displaced towards the sample (using a manual handle) until it came into contact with the outer surface of the stent. The tool then started to mill through the stent wall and a complete cut was assessed upon observation of green swarf, which originated from milling of the supporting core. At this time point, the *z*-position of the milling tool was fixed, and the indexing head was manually rotated using the red handle shown in Figure 6-1a.

The spindle speed in the machine was set to its maximum achievable value (10,000 rpm), in order to obtain the best milling finish [214]. Moreover, the indexing head rotation was opposite to the rotation direction of the milling tool, which would also contribute to improve the milling finish [215]. Alignment was carried out to ensure that the tip of the milling tool touched the centre line of the stent lumen surface (see Figure 6-2c&d). Figure 6-2 shows a CAD drawing of a segment of the stent lumen, with a schematic of the elliptical side-hole for the cases in which the milling tool is aligned with the centre line (labelled in light blue, in Figure 6-2c&d). The figure also shows shape distortion and dislocation of the side-hole due to misalignment.

Different milling styles were investigated to achieve a single cut:

a) A single 360° rotation (full round),

b) Two individual 180° rotation (half round)

c) Four individual 90° rotation (quarter rounds).

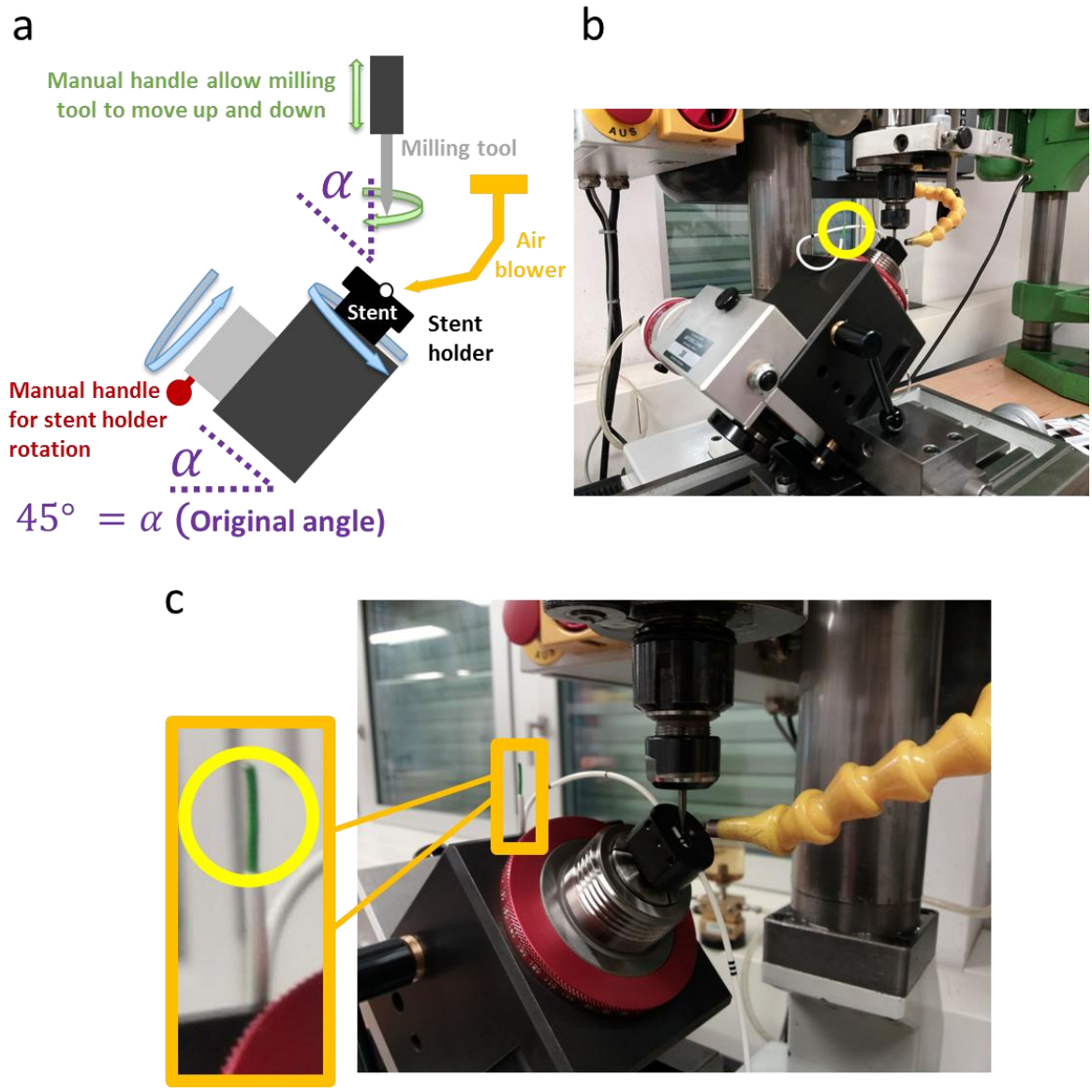

Figure 6-1 (a) Schematic representation of the milling setup used to fabricate triangular side-holes in stents. It comprises a milling tool (grey), a spindle to hold the tool (black), an air blower (orange) to remove debris during milling, the indexing head (grey) and its manual handle (red) for rotating the stent holder (black). The stent appears in white colour. The cutting angle (α) is also shown in purple. A photograph of the milling machine is illustrated in (b), with its integrated indexing head. The yellow circle highlights the supporting core inserted inside the stent, to achieve a better milling finish and prevent bending. A different view of the setup is illustrated in (c), with the inset showing a zoomed-in view of the sent (white) and the supporting core material (green).

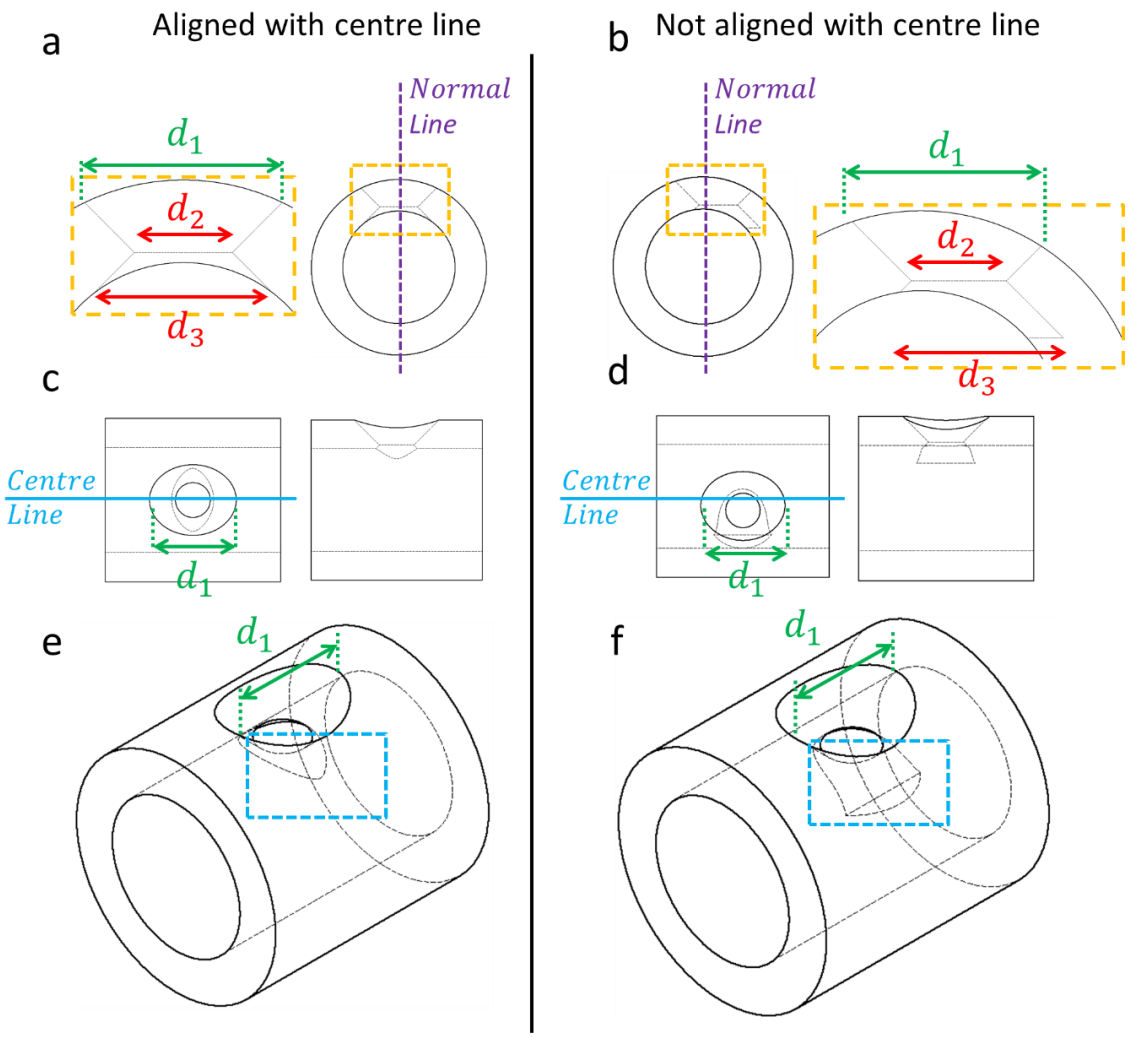

Figure 6-2 (a-b) CAD drawing (Inventor® Pro 2018, Autodesk®, USA) of the cross-sectional view of a segment of the stent, containing the generated side-hole shape. Insets include a labelling for d_1 (green), d_2 (red) and d_3 (red), which represent the major axes of the elliptical side-hole taken at different *z*-positions (top, middle, and bottom, respectively). Side-holes are illustrated for both cases of milling tool that is (a) aligned and (b) not-aligned with the centre line of the stent surface. The normal line (i.e. perpendicular to the surface centre line) is shown as a purple dashed line. (c-d) Top view (left) and side view (right) of the same CAD drawing, with the major axis of the top section of the elliptical side-hole (d_1) shown in green, and the centre line of the stent surface labelled in light blue, for both (c) aligned and (d) not-aligned scenarios. (e-f) Asymmetric view of the same CAD drawing, with the major axis of the top section of the elliptical side-hole (d_1) shown in green, and a dashed blue rectangular box to highlight the conformational change of the side-hole from (e) aligned to (f) not-aligned scenarios, where the change is mostly confined to the portion of side-hole located closer to inner lumen of the stent.

6.3.2 Procedures of analysis

As outlined at the beginning of this chapter, the aim of this study is to evaluate the accuracy and robustness of a method for manufacturing inclined/triangular side-holes through a ureteric stent. Micromilling was identified as a suitable manufacturing technique for this application, and a 45° cutting angle was selected (as shown in Figure 6-1a).

There are few parameters that need to be defined for milling holes with triangular shape on a tubular substrate. These include the diameter of the stent, size of the milling tools, milling style (as defined above), size of the core, lubrication of the core (which is necessary to insert the core inside the stent, but could cause unwanted relative displacement between core and stent during milling), and the alignment between milling tool and stent. Each of these parameters could affect the outcome of the fabrication process thus, it is important to establish a procedure for evaluating them.

The following paragraphs describe the procedures that were followed in order to determine the cutting and vertex angles. These comprised optical imaging and quantification of geometrical features of the stent and its side-holes.

6.3.2.1 Microscope imaging of side-holes

An axioplan-2 upright fluorescence microscope (Zeiss®, Germany) was employed to measure the vertex angle of the milled triangular side-holes. Prior to imaging, the milled segment of the stent was cut using a scalpel and placed on a glass slide. The sample was positioned in such a way that the side-hole would face the lens of the microscope objective (with 5× magnification). Images were captured using the AxioCam HRc (Zeiss®, Germany) with Zeiss 5x EC plan-Neofluar lens (with free working distance of 18.5 mm, numerical aperture of 0.16, field of view of 25 mm, parfocal length of 45.06 mm and coverglass thickness of 017 mm) to measure the shape of the hole at different depths. For this purpose, the distance between the stent surface and the lens was varied for 10 intervals (i.e. by moving the stage the downwards in 10 steps, to obtain a 3D image). Individual images were also combined using the 3D viewer in Fiji (NIH, USA) to reconstruct a 3D architecture of the side-hole. The same protocol was also employed to measure the stent wall thickness.

Overall, measurements and calculations were performed with the aim of assessing the general shape and finish of the hole (qualitative), major and minor axes of holes (quantitative), and stent vertex angle (quantitative) (see Figure 6-3). These steps are outlined in the following paragraph.

6.3.2.2 Dimensional characterisation of side-holes

To determine the wall thickness, the stent was cut into 11 pieces. Then, internal and external radii (i.e., *IR* and *ER* respectively) of the stent were measured using the microscope built-in software (Axiovision, Zeiss®, Germany). The wall thickness (*T*) was then calculated as (see Figure 6-3):

$$T = ER - IR \quad \text{(Eq 6-1)}$$

The major axes of the elliptical cross-section of the side-hole, taken at different depths (d_1, d_2 and d_3; as illustrated in Figure 6-3d) were measured from optical microscope images. The following trigonometrical relations were then employed to calculate the cutting angle (α) and the vertex angle (ϑ)(see Figure 6-3).

$$\alpha = \mathrm{ATan}\left(\mathrm{T} - \left(\frac{d_1 - d_2}{2}\right)\right) / \left(\frac{d_3 - d_2}{2}\right) \quad \text{(Eq 6-2)}$$

$$\theta = 2 \times \alpha \quad \text{(Eq 6-3)}$$

Thus, in order to obtain a vertex angle (θ) of 90° in the side-hole, the cutting angle (α) was set to a nominal value of 45° (see Figure 6-3).

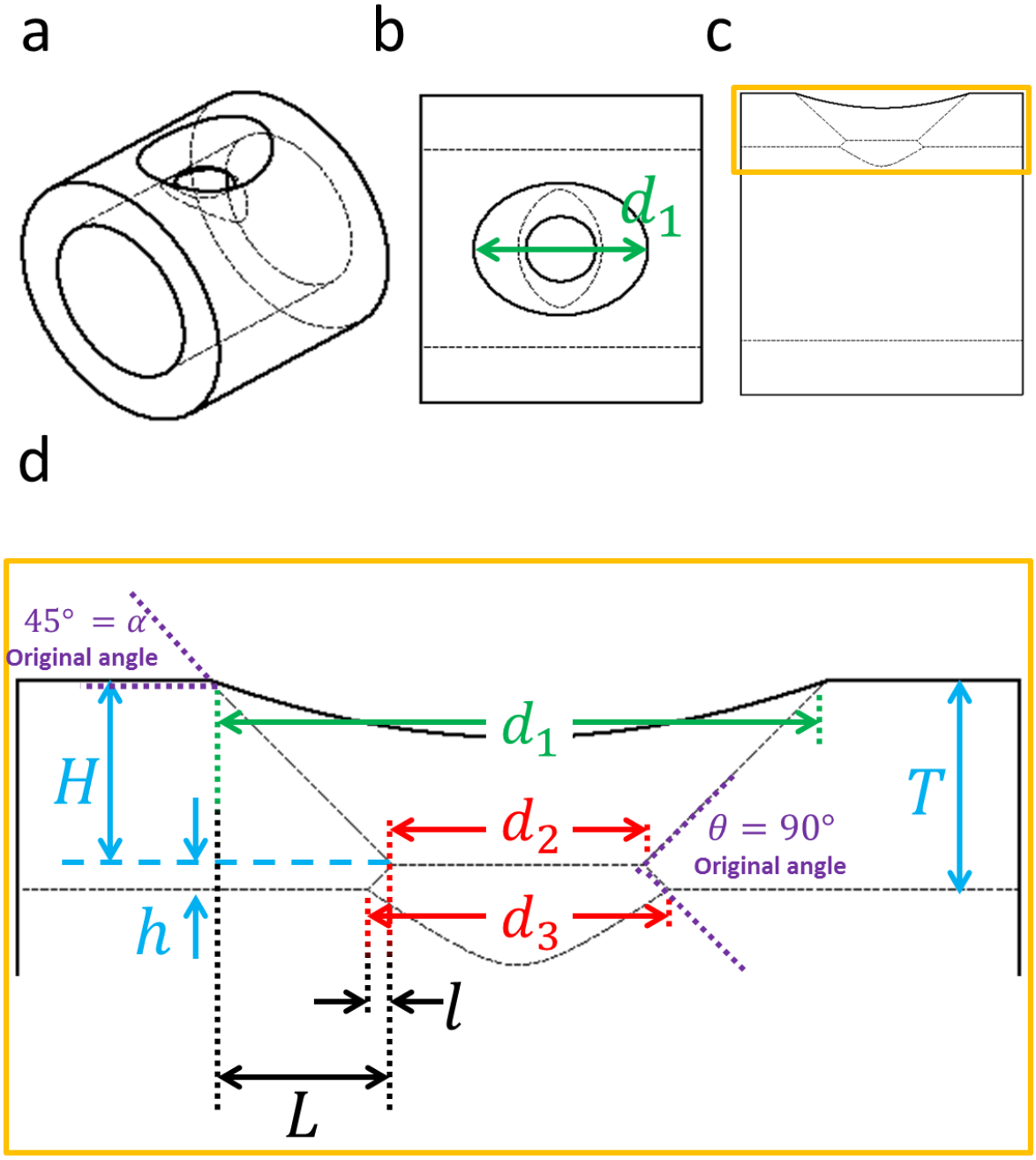

Figure 6-3 (a) Asymmetric view of the CAD drawing of a segment of the stent containing the generated side-hole shape, created using Inventor® Pro 2018 (Autodesk®, USA). (b) A top view of the fabricated side-hole, with an elliptical outlet, and with the major axis of the ellipses labelled in green. (c) Side view of the side-hole, with the corresponding zoomed-in view shown in (d). Labels indicate both inner and outer portions of the hole, and their corresponding thickness resulting from the cutting (*H* and *h*), the total wall thickness (*T*), and the axes of the elliptical major arms (d_1, d_2, d_3) taken at different depths along the side-hole. Both cutting (α) and vertex (θ) angles are also reported, together with their nominal values.

6.4 Results and Discussion

Figure 6-4a shows experimental values of the external radius (*ER*), internal radius (*IR*), and wall thickness (*T*) of the stent, taken at different positions along the stent. Mean values are equal to 1,278.4 ± 2.6 µm (*ER*), 755.3 ± 1.3 µm (*IR*), and 423.2 ± 1.8 µm (*T*). Figure 6-4b&c also shows two representative images of cross-sectional cuts of the stent (i.e., Cut 4 "C4" and Cut 11 "C11"). Variations in the experimental data taken along the stent (as shown in Figure 6-4a), and some localised geometrical alterations (as shown in Figure 6-4b&c), suggest that commercial stent lumens may present some defects or inaccuracies that need to be considered when milling triangular side-holes.

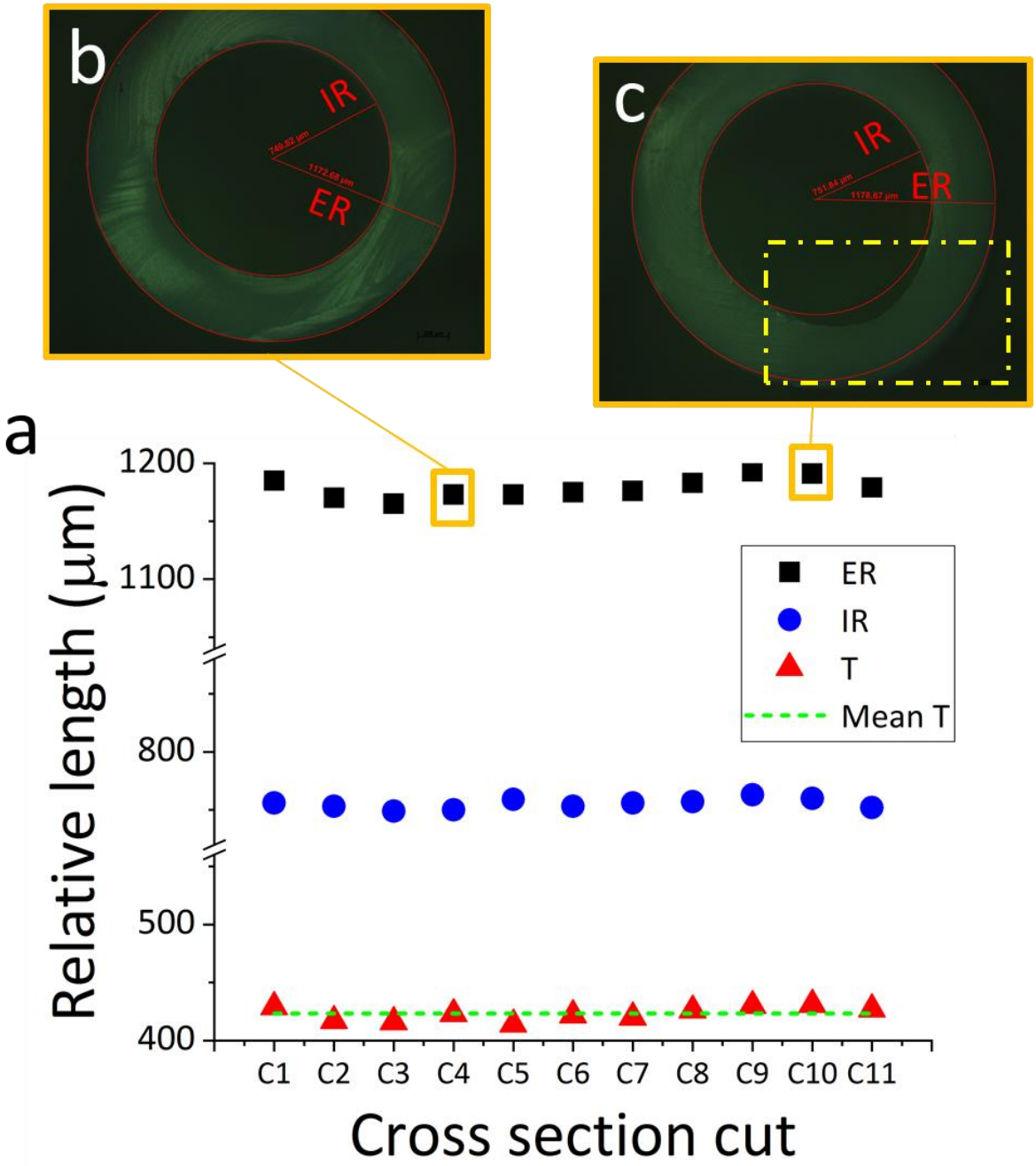

Figure 6-4 (a) shows the values of external radius (*ER*), internal radius (*IR*), wall thickness (*T*) and the mean wall thickness (*Mean T*) taken from 11 cuts along the stent length (single point measurements for each cut). (b) The cross sectional view of 'cut 4'. (c) The cross sectional view of 'cut 11', and a localised deformation of the stent wall shown within a yellow dot-dashed rectangular box.

Figure 6-5 shows a CAD drawing of a segment of a stent lumen with elliptical side-hole, for both cases in which the wall of the stent is uniformly extruded (such as the one shown in Figure 6-4b) and non-uniformly extruded (such as the one shown in Figure 6-4c). The figure demonstrates the effect of wall uniformity on the shape of the obtained side-hole. The side view illustrated in Figure 6-5a shows the presence of three major axes along the depth of the elliptical side-hole, when the

stent wall has a uniform thickness. In the presence of a localised alteration of the cross-section (such as the one shown in Figure 5-4c), only two major axes would be present, with a significant effect on the overall shape of the side-hole (see Figure 5-5b). Moreover, an increase of the external major axis of the elliptical side-hole (i.e., facing the external surface of the stent) would be anticipated in the case of a non-uniform wall, compared to a uniform wall (i.e., $d_{1(U)} < d_{1(NU)}$). This is demonstrated qualitatively in Figure 6-5e&f, for two designs having the same length of the stent lumen.

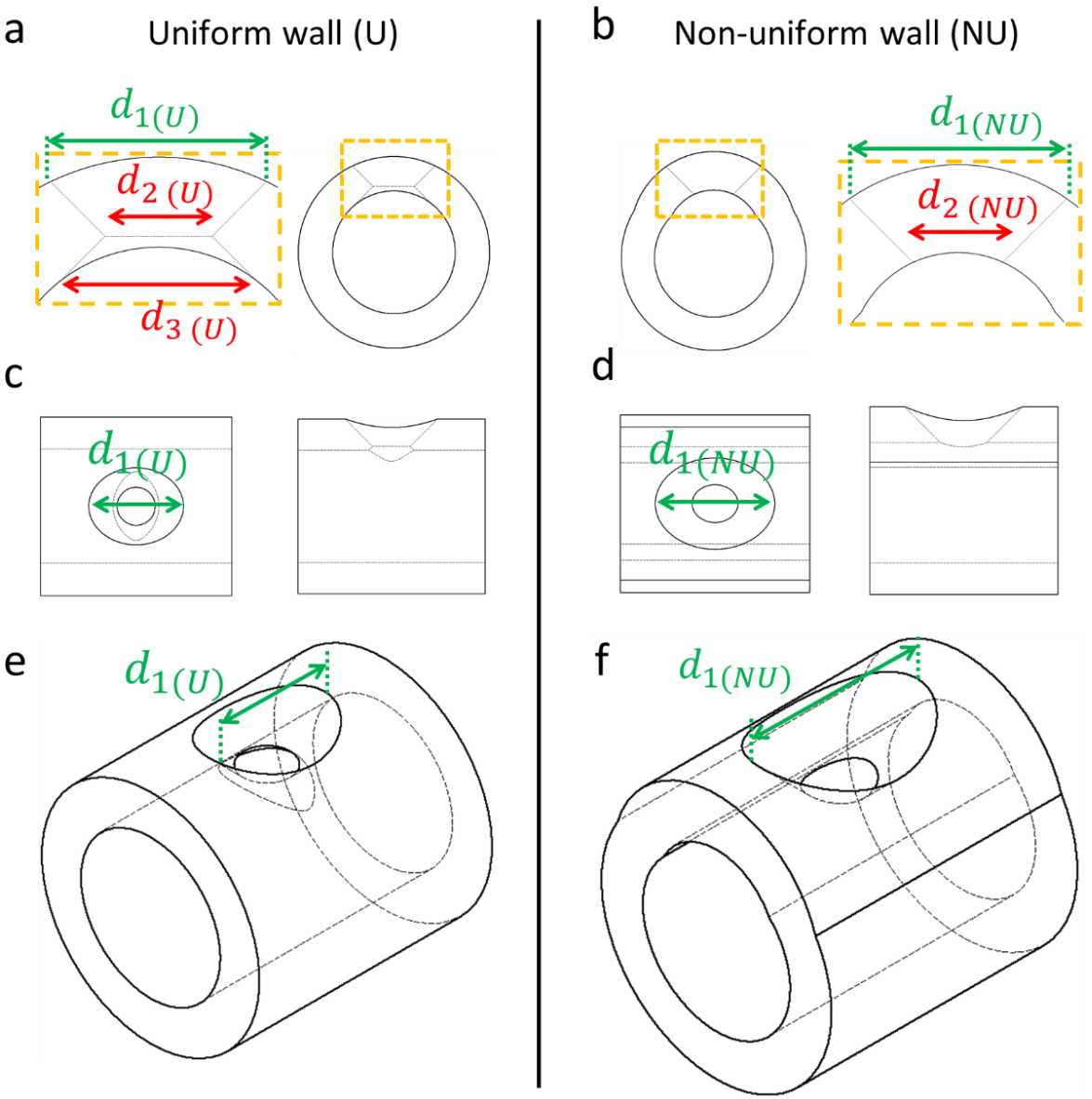

Figure 6-5 (a-b) Cross-sectional view of a CAD drawing of a segment of the stent containing the generated side-hole shape, and designed using Inventor® Pro 2018 (Autodesk®, USA). In the case of (a) uniform wall (U), the inset shows $d_{1(U)}$ (green), $d_{2(U)}$ (red) and $d_{3(U)}$ (red), representing the major axes at the top, middle and bottom sides of the elliptical side-hole, respectively. In the case of (b) a non-uniform wall (NU), the inset shows $d_{1(NU)}$ (green) and $d_{2(NU)}$ (red), representing the major axes at the top and bottom sides of the elliptical side-hole, respectively. (c-d) Top view (left) and side view (right) of the same CAD drawing, with the major axis at the top side of the elliptical side-hole labelled as $d_{1(U)}$ (green) and $d_{1(NU)}$ (green) for (c) U and (d) NU walls, respectively. An asymmetric view of the same drawings is shown in (e-f) for both (e) U and (f) NU walls.

Table 6-1 shows the values of the major axes of the elliptical cross-section of the side-hole taken at different depths (d_1, d_2 and d_3), and measured from four samples. These values, together with the measured value of mean wall thickness reported above, were used to determine the cutting and vertex angles plotted in Figure 6-6.

Table 6-1 length of the major axes of the elliptical sections of the side-hole (d_1, d_2, and d_3) measured experimentally, as well as the corresponding milling style used (for a 7 Fr stent).

Sample number	*d_1 (µm)*	*d_2 (µm)*	*d_3 (µm)*	*Milling Style*
Sample 1	1,873	1,175	1,179	Single Round
Sample 2	2,005	1,343	1,352	Single Round
Sample 3	2,035	1,218	1,215	2 X Half Rounds
Sample 4	1,913	1,120	1,106	4 X Quarter Rounds

Figure 6-6a&b show the calculated values of cutting angle (α) and vertex angle (θ), respectively, and the green dashed line represents the nominal angles. Note that an experimental cutting angle of 45° was set in all cases, and measured using a protractor. The vertex angles were equal to 97.7°, 102.3°, 90.6° and 91.2° for samples 1, 2, 3 and 4, respectively. Sample 1 and 2 were manufactured using the same 'Single Round' milling style, whilst samples 3 and 4 using the '2 X Half Rounds' and '4 X Quarter Rounds' milling styles, respectively. The results show that vertex angles in samples 3 and 4 were very close to the original (nominal) angle. This demonstrates that milling triangular side-holes with multiple half- or quarter-rounds results in a more accurate fabrication process, as opposed to using a single-round cutting method.

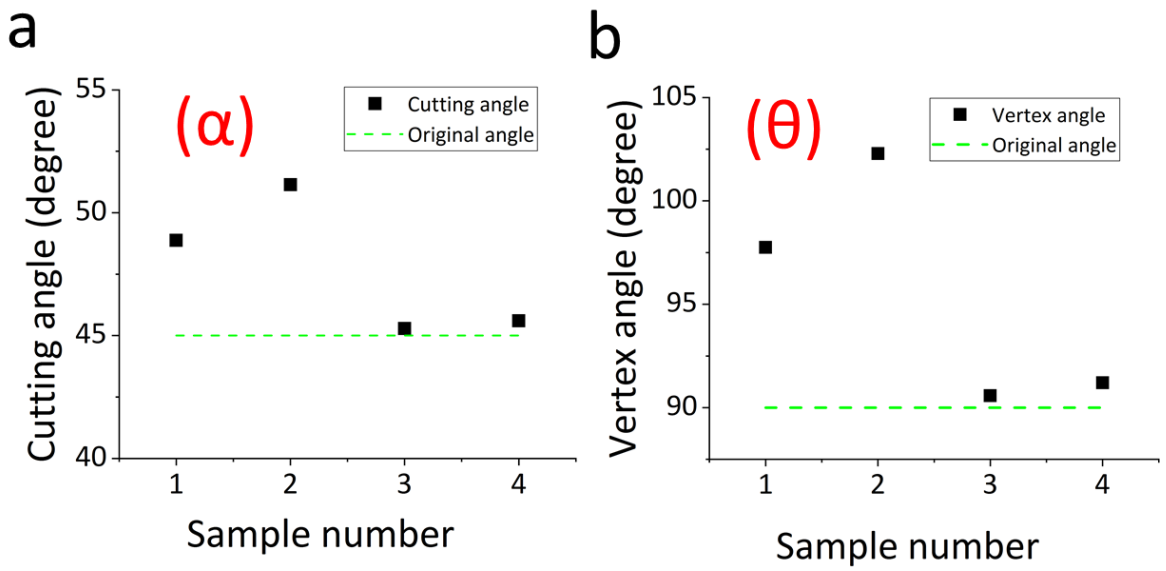

Figure 6-6 (a) values of cutting angle plotted for each test, calculated *via* trigonometrical calculations (described in the Methods section). The dashed green line represents the nominal cutting angle. (b) Values of vertex angle plotted for each test, calculated *via* trigonometrical calculations (described in the Methods section). The dashed green line represents the nominal cutting angle.

Figure 6-7 shows images of the top view of triangular side-holes, which have an elliptical cross-section as anticipated in Figure 6-3. As shown in Figure 6-7a&b, sample 1 and 2 had more debris (see red dashed rectangular boxes) and fractures/bumps (see yellow dashed rectangular box) compared to the images in Figure 6-7c&d, which refer to samples 3 and 4. This further demonstrates that hole cutting using either the Half or Quarter Rounds method is more favourable than a Single Round cutting method, as it provides a higher quality finish. Interestingly, a fracture/bump is located at the left corner of side-holes, which corresponds to the first point of contact between the milling tool and the stent surface, and it is almost identical (in terms of the shape, size and location) across different samples.

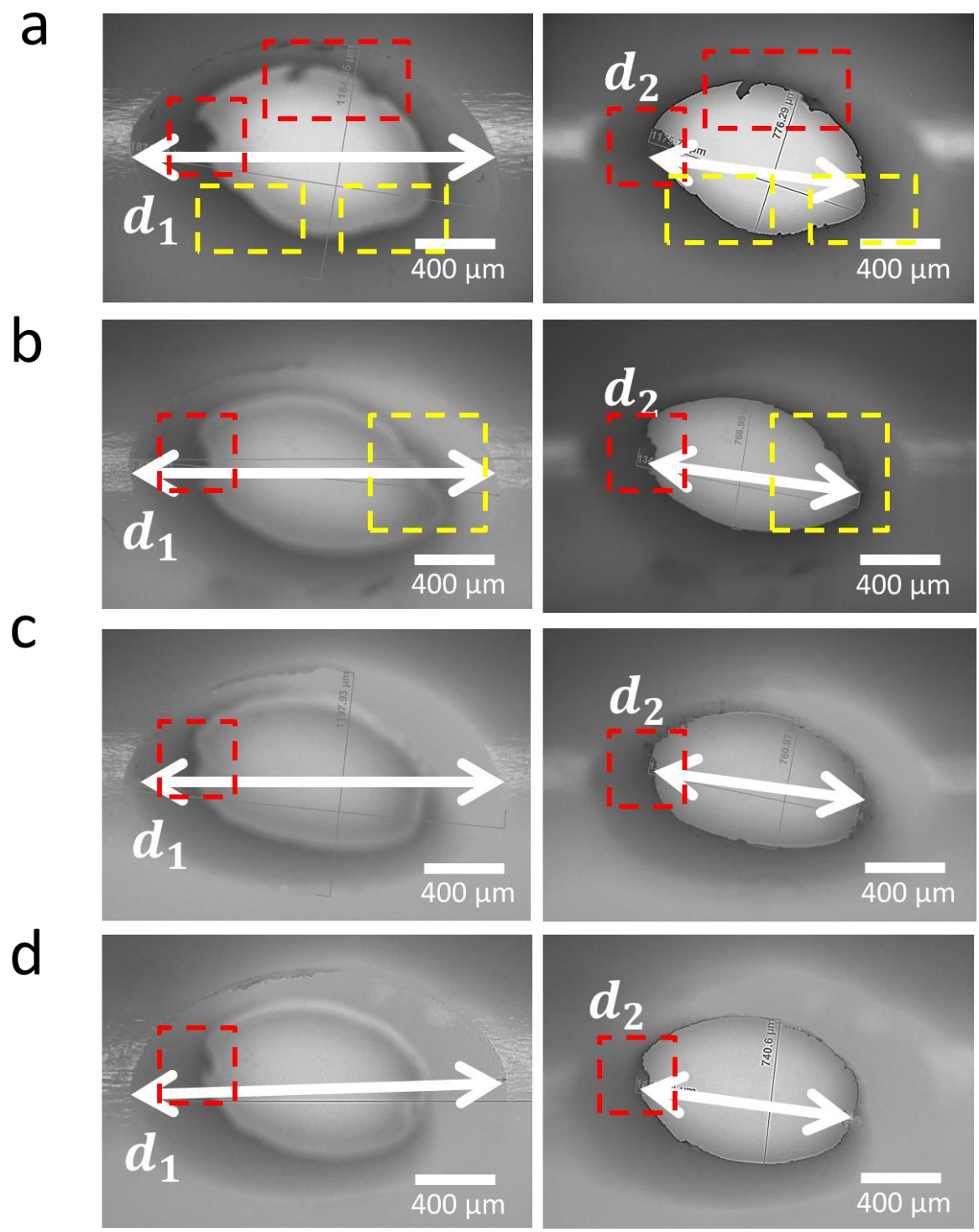

Figure 6-7 Top view of a triangular side-hole manufactured on a 7 Fr silicone stent, focusing on the external surface (left) of the stent and the vertex tip plane (right) of the stent, for sample number (a) 1, (b) 2, (c) 3, and (d) 4. Red dashed rectangular boxes in all pictures indicate the position of debris, and yellow dashed rectangular boxes highlight edges with fractures/bumps.

Figure 6-8 shows the CAD drawing of a segment of the stent containing a side-hole with the novel shape as well as a photo of the prototyped stent using the aforementioned micro-milling method

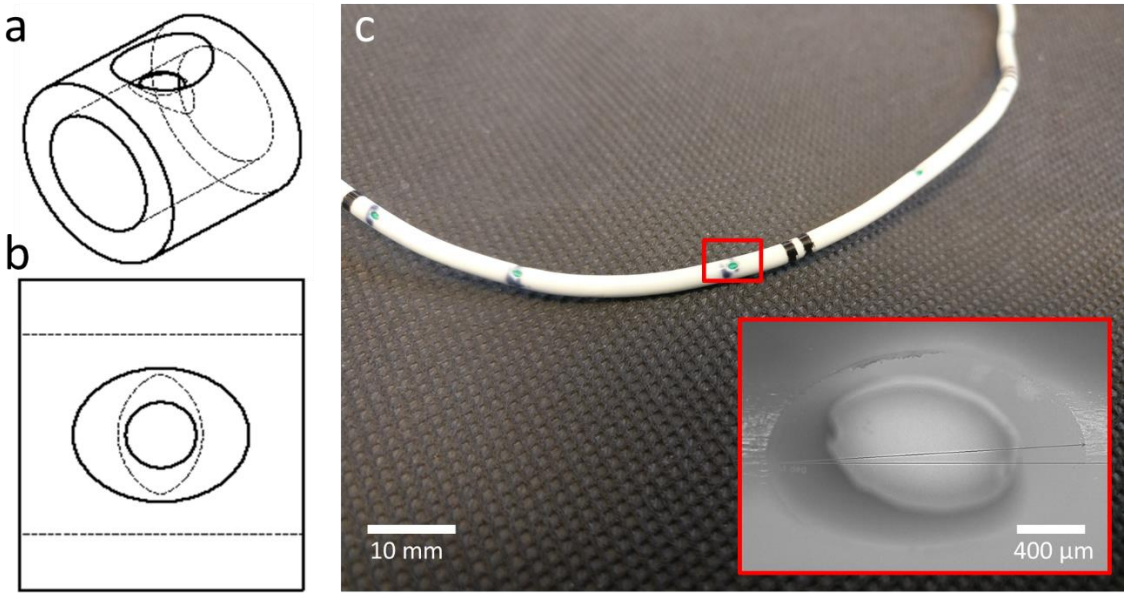

Figure 6-8 (a) Asymmetric view of the CAD drawing of a segment of the stent containing the generated side-hole shape, created using Inventor® Pro 2018 (Autodesk®, USA). (b) A top view of the fabricated side-hole, with an elliptical outlet. (c) Photograph of the newly prototyped stent; the inset shows a top view of a streamlined side-hole manufactured on a 7 Fr silicone stent.

6.5 Conclusion

As shown in Chapter 4, a streamlined side-hole with triangular shape has potential for significantly reducing accumulation of encrusting deposits in ureteric stents, and particularly within inactive side-holes. There is however no established technique for producing this specific side-hole architecture on a ureteric stent. In this study, preliminary results are presented demonstrating the usage of a micromilling-based manufacturing method to fabricate side-holes of arbitrary shape. The method employed a commonly used micro-milling technology and an indexing head, and combined them with an in-house built stent holder in order to cut triangular side-holes through tubular stents containing a supporting core (see Figure 6-8).

The evidence provided in this Chapter indicates that this method has potential for generating triangular side-holes (with elliptical cross-section) through the wall of a ureteric stent. Results also demonstrated that milling using multiple half- and/or quarter-rounds, rather than a single-round, provided a more accurate reproduction of the vertex angle and a superior milling finish.

In this method, there are different parameters that play important role on the quality of the end-product and the fabrication robustness, including the relative size of milling tool and stent, milling style, direction of the milling tool rotation relative to the rotation of the indexing head, material of the supporting core, and procedure of core insertion. The following steps could be performed in order to improve the developed manufacturing method: 1) employ an automated system to assist the alignment of the stent, in order to achieve the correct cutting angle and a repeatable offset position; 2) investigate the effect of employing different core materials on the fabrication accuracy, and compare them with the one used in this study; 3) investigate different milling styles, such as a combination of the ones used in this study (e.g. two individual half rounds, followed by a full round); 4) utilise stents with a more uniform thickness, as it likely influences the vertex angle; 5) increase the number of samples, to obtain statistically significant data; and 6) identify a suitable cleaning procedure for removing debris after manufacturing.

Chapter 7 Conclusion and Future Work

7.1 Outline

This chapter provides a conclusion of the work presented in this thesis, on a chapter-by-chapter basis. It summarises the main research achievements, and how they contributed to the main aim of the study. Furthermore, a discussion of future research directions is provided at the end of the chapter.

7.2 Conclusion

The main function of ureteral stents is to retrieve urine drainage in either cases of external or internal occlusions of the ureter lumen, lowering the static pressure within the kidneys and thus reducing the risk of renal damage. This provides a time frame to practitioners for planning procedures of removal of the source of obstruction. There are however, several side effects associated with ureteral stenting that complicate their clinical management, particularly in the long term. Encrustation and biofilm formation over the stent surface is one of the most common causes of stent failure, and in some cases require open surgery to remove the stent. Given that these issues profoundly affect a patient's quality of life, the overall therapeutic outcome and associated costs, further efforts should be put in place in an attempt to effectively address and resolve them.

Different strategies have been developed in the past in order to reduce the impact of encrustation on the stent lifetime. Most studies have focused on the potential of material and surface properties to reduce encrustation rates. However, the translation of these strategies into the industrial and clinical environments is often hindered by high cost and technological complexity. In the present study, a novel approach against stent encrustation was developed. It relied on the underlying hypothesis that there exists a quantitative correlation between wall shear stress within a stented ureter, and the rate and amount of deposition of encrusting bodies. Upon verification, this principle has been employed to guide the design of new stent architectures promoting the generation of localised shear stress fields, and hence capable of delaying the encrustation process. This approach has the advantage of being a cost-effective route to increase the lifetime of ureteral stents, and would be a viable option to be implemented within existing industrial manufacturing processes.

In a first step of this study (Chapter 2), state-of-the-art ureteric stent technologies were critically reviewed, with a focus on those aiming at preventing or reducing formation of encrustation over

the stent surface. Emphasis was also given to earlier studies that hypothesised a role for urine flow dynamics on the formation of encrusting crystals and biofilms. Notably, a critical analysis of the literature revealed a lack of quantitative studies correlating flow and encrustation processes in stents.

In Chapter 3, a microfluidic-based model of the occluded and stented ureter (referred to as 'stent-on-chip') was developed and employed to quantify the distribution of both wall shear stress (WSS) and encrusting deposits, using numerical simulations and experiments, respectively. Using this model, an inverse correlation between WSS and amount/growth rate of encrusting particles was determined for the first time. Critical regions susceptible to encrustation were thus identified, corresponding to inactive side-holes of the stent and the occluded cavity. It was also speculated that the majority of side-holes in a real stented ureter system would act as stagnation sites, and therefore represent potential "hot spots" for the anchoring and deposition of encrusting deposits. These hydrodynamic regions could provide an environment for the growth of larger crystals and the entrapment of bacteria to form a complex bio-chemical layer, as described in previous studies.

These findings were successfully verified at a full-scale, by performing three-dimensional CFD simulations and experiments *in-vitro*, using an artificial model of the urinary system developed in-house (see Chapter 4). Full-scale simulations confirmed that the large majority of side-holes in a stent suffered from low-WSS, and this was associated with high levels of encrustation in the experiments. Notably, increased WSS at side-holes was observed at regions characterised by a reduction or obstruction of the ureter lumen, which caused diversion of the flow and enhanced inter-compartment fluid exchange through the side-holes.

The work presented in these Chapters contains several aspects of novelty, including:

- A microfluidic device replicating relevant hydrodynamic regions of a stented and occluded ureter has been developed. The device allows for *in situ* monitoring of transport phenomena involving fluid and chemical species, which are relevant to urine flow in the stented ureter.
- A systematic, experimental and computational characterisation of the fluid dynamic field within 2D and 3D models of the occluded and stented ureter has been performed.
- A quantitative correlation between wall shear stress and the growth of encrusting deposits in stents has been determined, and critical regions of the stent which are more susceptible to encrustation have been identified.

In Chapter 5, stent-on-chip models were employed as a platform to investigate changes to both global (wall thickness) and local (side-hole shape) architectural features of the stent. An inverse correlation between the local WSS and the rate of deposition of encrusting bodies was observed for all geometrical configurations investigated, confirming the earlier findings (Chapter 3 and Chapter 4). Remarkably, a combination of an optimal stent wall thickness (0.3 mm) and hole shape (triangular isosceles, vertex angle = 45°) resulted in a significant increase of WSS within both active and inactive side-holes and the occluded cavity, causing a significant reduction in the deposition of encrusting bodies in these regions (up to 90% reduction compared to a standard stent model). The work presented in this Chapter includes the first systematic study of the effect of changing some architectural features of the stent on the formation/growth of encrusting deposits, leading to the identification and design of a novel stent architecture capable of reducing encrustation rates.

In Chapter 6, a first manufacturing approach to the fabrication of triangular side-holes in stents was demonstrated and characterised. The method relied on the use of micromilling technology, with adaptations to allow for the generation of triangular holes on tubular structures. Triangular holes were successfully manufactured for the first time; however, further optimisation of this technique is required to improve its flexibility and the quality of the end product.

In conclusion, results from this study may open new avenues for the development of flow-based solutions to the major complication represented by stent encrustation. However, future validation of the developed stent design (including pre-clinical investigations) is required, to demonstrate its efficacy against encrustation within a more physiologically relevant environment. These future steps of the study are described in the following paragraph.

7.3 Future Work

Aspects of future work are described in the following paragraphs, and relate to stent's fabrication, and the evaluation of its performance *in-vitro* and *in-vivo*.

7.3.1 Improving the stent fabrication procedure

Further investigations are needed to improve the procedure developed to manufacture triangular side-holes in ureteric stents. The following aspects will be investigated:

(i) The effect of the following parameters on the milling finish and fabrication accuracy: diameter of the milling tools, milling spindle speed, automation of the milling tool alignment, type of core, and alternative methods of keeping the stent in position (such as using coolants; i.e. liquid nitrogen).

(ii) Methods of cleaning and sterilising the stent, which is required for performing *in-vivo* studies.

(iii) The potential usage of ultrafast lasers for fabricating side-holes with higher accuracy and quality of the end-product (i.e., to reduce the amount of debris and defects). Although this method has been regarded as costly, potential for reducing manufacturing costs *via* scaled-up production will be investigated.

7.3.2 Pre-clinical *in-vivo* study

In collaboration with a centre specialised in pre-clinical studies (Vancouver Stone Centre, Canada), experiments will be conducted on animal models, to validate the performance of the new stent prototype in a physiologically relevant model. The potential design of the study is described below:

The scientific literature concerning *in-vivo* studies on encrustation and biofilm formation in stents suggests that 21 days is a sufficient time window for evaluating initiation of these complications. A time window of 2-3 weeks has proven to be sufficiently long to investigate formation of encrustation and biofilms, as shown by Peter et al. [216]. This is also consistent with typical clinical stent deployment times.

A sample size of 12 animals will be employed, as a compromise between statistical relevance of the proof-of-concept study, costs, and minimisation of animal usage.

The animal model chosen is the porcine model, which is widely employed in pre-clinical evaluation of urinary devices. Animals will be sourced few weeks before the beginning of the study, in order to undergo quarantine. Feeding, homing, vaccination, identification, and deworming of the animals is mandatory. Surgical procedures will be performed under general anaesthesia, and animals will be given the approved antibiotic and analgesic treatments after every procedure.

The study is articulated in the following milestones:

1. Baseline evaluation. All 12 animals will undergo a baseline study in order to evaluate and discard any morphological and functional anomalies that may interfere with the study. This assessment includes:

    i. Blood analysis: haematology, blood biochemistry.

    ii. Urinalysis.

    iii. Urine culture: urine sterility before placement of the stent will be assessed.

iv. Ultrasonographic evaluation of the urinary tract: morphologic and haemodynamic assessment to check the level of hydrourter or hydronophrosis.

Upon evaluation of the results from urinalysis and culture (duration = 1 week), stent deployment will be performed

2. Retrograde stent placement.

i. Blood analysis: haematology, blood biochemistry.

ii. Urinalysis.

iii. Urine culture.

iv. Placement of the ureteral stent by endoscopic and fluoroscopic approach.

3. First follow-up (7 days from insertion)

i. Blood analysis: haematology, blood biochemistry.

ii. Urinalysis.

iii. Urine culture.

iv. Ultrasonographic evaluation of the urinary tract: morphologic and haemodynamic assessment.

4. Second follow-up (14 days from insertion). Upon completion of the same evaluation tests as in the baseline study and the 7-day follow-up, the ureteral stents will be withdrawn to perform:

i. Microbiological study: detection and identification of bacteria on the stent surface. Output: type and number of bacteria present over the stent surface.

ii. Optical study: qualitative/quantitative optical assessment of encrustation and side-hole obstruction. Output: type and size of encrustation, including % area covered by encrustation and % number of occluded side-holes.

The above qualitative and quantitative criteria will be employed to assess the performance of the new stent prototype against the competing solution (commercial stent).

7.3.3 *SoC* modelling in a more complex chemical and biological environment

Experiments similar to the ones described in Chapter 3 will be conducted in order to evaluate formation and deposition of encrusting crystals with SOCs, in a more complex chemical and

micro-biological environment. In order to gain a deeper understanding of the role of bacteria in stent encrustation, experiments will be conducted both in the presence and absence of relevant microorganisms. The chemical composition of the surrogate urine and the type and volumetric concentration of microorganisms will be varied, in order to replicate distinct physiological and pathological conditions. These experiments may open new insights into the mechanisms governing formation and accumulation of crystals in stents.

7.3.4 *In-vitro* full-scale urinary system model

Another important step towards clinical translation of the developed stent prototypes involves evaluating their effect on the physiogical urodynamics. For instance, it is important to assess the effect of a new stent model on the renal pelvic pressure, the peristaltic activity of the ureter, and the priming and voiding dynamics of the bladder. *In-vitro* models developed previously are not capable of replicating these complex features of the urinary system. Future work will thus focus on developing artificial models capable of replicating some physiological characteristics of the urinary system, which will be employed as a screening platform to investigate different stent prototypes and compare them against commercial stents.

Preliminary prototypes of these models are illustrated in Figure 7-1, and comprise an artificial model of a collapsible bladder with physiologically relevant dimensional and mechanical properties (see Figure 6-1a), and a model of the peristaltic activity of the ureter (see Figure 6-1b) with potential for regulating amplitude and frequency of the peristaltic wave.

Notably, these models have significant potential for reducing the usage of animal models in pre-clinical urological research, and could also be employed as an educational platform for the training of future urologists.

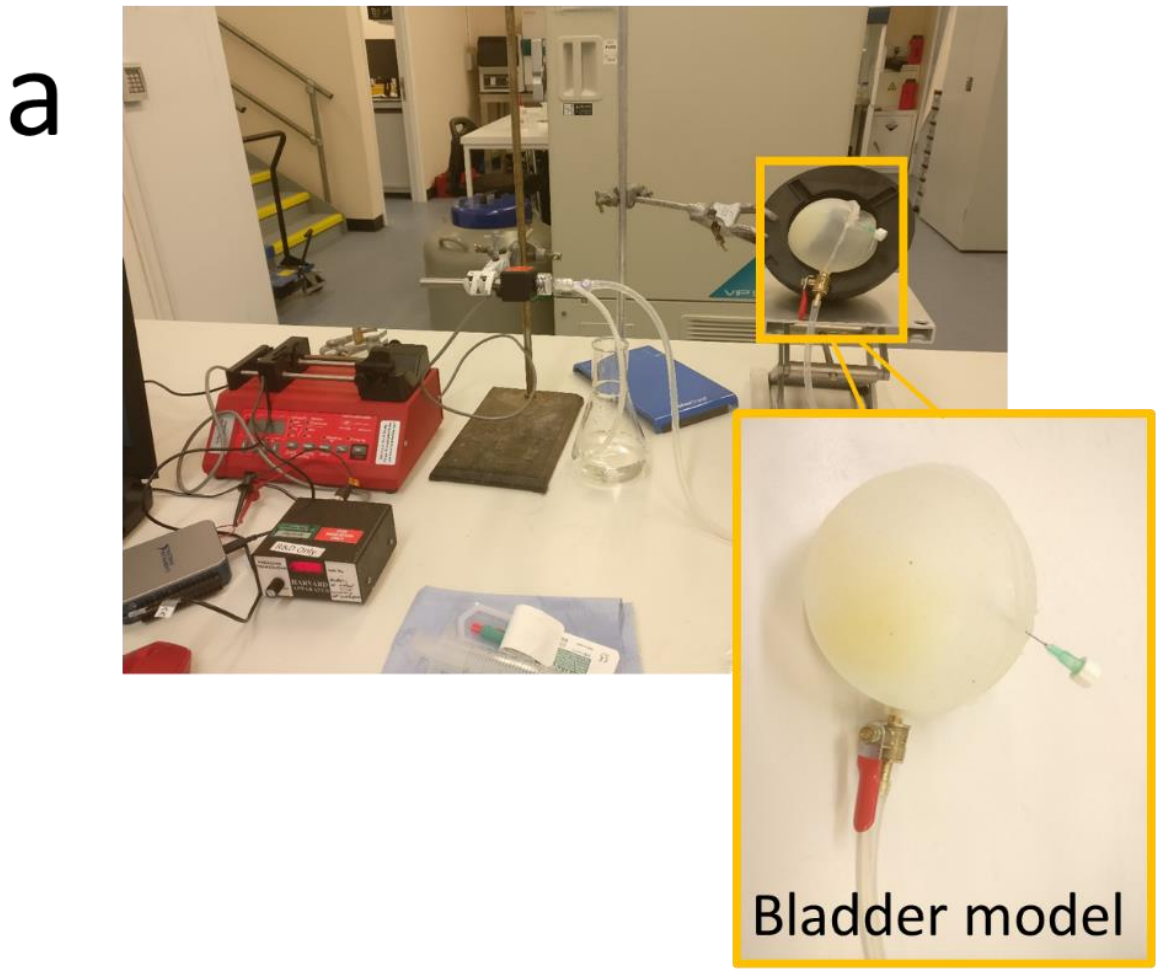

Figure 7-1 (a) Artificial model of the bladder, replicating the priming/voiding dynamics of a physiological bladder; and (b) artificial model of the ureteric peristalsis, allowing to replicate a physiological bolus-flow.

List of References

1. Rosdahl, C.B. and M.T. Kowalski, *Textbook of basic nursing*. 2008, Lippincott Williams & Wilkins. p. 277-286.

2. Fillingham, S. and J. Douglas, *Urological nursing*. 2004, Baillière Tindall. p. 11.

3. Caine, S.B., F.J. Hinman, and M, *Benign Prostatic Hypertrophy*. 2011: Springer. 1128.

4. Tseng, T.Y. and M.L. Stoller, *Obstructive Uropathy.* Clinics in Geriatric Medicine, 2009. **25**(3): p. 437-443.

5. *Management of Acute Kidney Problems*, ed. A.J. Kellum, R. Claudio, and A. John. 2009: Springer. 678.

6. (NHS), N.H.S. *Kidney Stone*. 2017; Available from: https://www.nhs.uk/conditions/kidney-stones/causes/.

7. Pfau, A. and F. Knauf, *Update on Nephrolithiasis: Core Curriculum 2016.* American Journal of Kidney Diseases. **68**(6): p. 973-985.

8. Sohgaura, A. and P. Bigoniya, *A Review on Epidemiology and Etiology of Renal Stone.* 2017.

9. Soria, F., *Memorandum of Understanding for the implementation of the COST Action "European network of multidisciplinary research to improve the urinary stents" (ENIUS) CA16217*. 2017, COST "european cooperation in science and technology": Brussels. p. 19.

10. Fung, L.C. and A. Atala, *Constant elevation in renal pelvic pressure induces an increase in urinary N-acetyl-beta-D-glucosaminidase in a nonobstructive porcine model.* The Journal of urology, 1998. **159**(1): p. 212-216.

11. *Obstructive Uropathy*, ed. P.H. O'Reilly. 2012: Springer. 326.

12. Greenberg, A. and A.K. Cheung, *Primer on Kidney Diseases, 4e (Greenberg, Primer on Kidney) 4th Edition by Greenberg, Arthur published by Saunders Paperback*. 1994: Saunders.

13. *Renal and Electrolyte Disorders (Renal and Electrolyte Disorders (Schrier))*, ed. R.W. Schrier. 2010: LWW. 640.

14. Kyle, S.S.-R. and Theresa, *Maternity and Pediatric Nursing*. 2008: Lippincott Williams and Wilkins. 1968.

15. Sc, B.N.G.M.H., G.K.D.A.S.B.A.D.N.M.P.H.D.B.V.G.C.B.M. Jodie Hughson Mph Grad Cert Health Promotion Rn Certificate Iv Tae, and A. Kate Stainton Dip, *Tabbner's Nursing Care: Theory and Practice, 6e*. 2013: Churchill Livingstone. 1104.

16. Pnp, P. and D.R. Dr Adele Pillitteri Ph, *Maternal and Child Health Nursing: Care of the Childbearing and Childrearing Family*. 2013: LWW. 1744.

17. Jones, J.A.M., D.F. Ralph, D. Catherine, and M.Douglas, *Oski's Solution: Oski's Pediatrics - Principles and Practice: Plus Intergrated Content Website (Pediatrics: Principles & Practice (Oski's/ McMillan))*. 2006: Lippincott Williams & Wilkins,US. 2808.

18. *Diagnostic Nuclear Medicine (Medical Radiology)*, ed. C. Schiepers. 2005: Springer. 356.

19. Djeribi, R., W. Bouchloukh, T. Jouenne, and B. Menaa, *Characterization of bacterial biofilms formed on urinary catheters.* American Journal of Infection Control, 2012. **40**(9): p. 854-859.

20. Liu, C., X.-J. Liu, D. Liu, and D.-W. Yao, *A giant ureteral polyp mimicking as a bladder mass resected ureteroscopically by diode laser: A case report and literature review.* International journal of clinical and experimental pathology, 2015. **8**(11): p. 14580.

21. Pishchalnikov, Y.A., O.A. Sapozhnikov, M.R. Bailey, J.C. Williams Jr, R.O. Cleveland, T. Colonius, L.A. Crum, A.P. Evan, and J.A. McAteer, *Cavitation bubble cluster activity in the breakage of kidney stones by lithotripter shockwaves.* Journal of endourology, 2003. **17**(7): p. 435-446.

22. *Smith's Textbook of Endourology*, ed. A.D.S.M.D. Kavoussi, et al. 2012: Wiley-Blackwell. 1894.

23. *Difficult Cases in Endourology*, ed. A.A.-K. Smith, I.I.I.G. Michael, and D. Arthur. 2012: Springer. 364.

24. Albala, D.M., L.G. Gomella, A.F. Morey, and J.P. Stein, *Oxford American handbook of urology*. 2010, Oxford University Press. p. 571-658.

25. Davenport, K., V. Kumar, J. Collins, R. Melotti, A.G. Timoney, and F.X. Keeley Jr, *New Ureteral Stent Design Does Not Improve Patient Quality of Life: A Randomized, Controlled Trial.* The Journal of Urology, 2011. **185**(1): p. 175-178.

26. Stoller, M.L., B.F. Schwartz, J.R. Frigstad, L. Norris, J.B. Park, and M.J. Magliochetti, *An in vitro assessment of the flow characteristics of spiral-ridged and smooth-walled JJ ureteric stents.* BJU International, 2000. **85**(6): p. 628-631.

27. Ryan, P.C., G.M. Lennon, P.A. McLean, and J.M. Fitzpatrick, *The effects of acute and chronic JJ stent placement on upper urinary tract motility and calculus transit.* British Journal of Urology, 1994. **74**(4): p. 434-439.

28. Patel, U. and M.J. Kellett, *Ureteric drainage and peristalsis after stenting studied using colour Doppler ultrasound.* British Journal of Urology, 1996. **77**(4): p. 530-535.

29. Lennon, G.M., J.A. Thornhill, R. Grainger, T.E.D. McDermott, and M.R. Butler, *Double pigtail ureteric stent versus percutaneous nephrostomy: Effects on stone transit and ureteric motility.* European Urology, 1997. **31**(1): p. 24-29.

30. Clavica, F., X.F. Zhao, M. ElMahdy, M.J. Drake, X.L. Zhang, and D. Carugo, *Investigating the Flow Dynamics in the Obstructed and Stented Ureter by Means of a Biomimetic Artificial Model.* Plos One, 2014. **9**(2).

31. Richter, S., A. Ringel, M. Shalev, and I. Nissenkorn, *The indwelling ureteric stent: a 'friendly' procedure with unfriendly high morbidity.* BJU International, 2000. **85**(4): p. 408-411.

32. *Urinary Stone Disease: The Practical Guide to Medical and Surgical Management (Current Clinical Urology)*. 2007 ed. Current Clinical Urology, ed. M.L. Stoller, Meng, Maxwell V. 2007: Humana Press.

33. Haleblian, G., K. Kijvikai, J. de la Rosette, and G. Preminger, *Ureteral Stenting and Urinary Stone Management: A Systematic Review.* The Journal of Urology, 2008. **179**(2): p. 424-430.

34. Wilks, S.A., M.J. Fader, and C.W. Keevil, *Novel Insights into the <italic>Proteus mirabilis</italic> Crystalline Biofilm Using Real-Time Imaging.* PLoS ONE, 2015. **10**(10): p. e0141711.

35. Hausegger, K. and H. Portugaller, *Percutaneous nephrostomy and antegrade ureteral stenting: technique—indications—complications.* European Radiology, 2006. **16**(9): p. 2016-2030.

36. Schulze, K.A., J.N. Wettlaufer, and G. Oldani, *Encrustation and stone formation: Complication of indwelling ureteral stents.* Urology, 1985. **25**(6): p. 616-619.

37. Keane, P.F., M.C. Bonner, S.R. Johnston, A. Zafar, and S.P. Gorman, *Characterization of biofilm and encrustation on ureteric stents in vivo.* British Journal of Urology, 1994. **73**(6): p. 687-691.

38. Kawahara, T., H. Ito, H. Terao, M. Yoshida, and J. Matsuzaki, *Ureteral Stent Encrustation, Incrustation, and Coloring: Morbidity Related to Indwelling Times.* Journal of Endourology, 2011. **26**(2): p. 178-182.

39. KohlerOckmore, J. and R.C.L. Feneley, *Long-term catheterization of the bladder: Prevalence and morbidity.* British Journal of Urology, 1996. **77**(3): p. 347-351.

40. Keane, P.F., M.C. Bonner, S.R. Johnston, A. Zafar, and S.P. Gorman, *Characterisation of biofilm and encrustation on ureteral stents in-vivo.* British Journal of Urology, 1994. **73**(6): p. 687-691.

41. Stickler, D.J., A. Evans, N. Morris, and G. Hughes, *Strategies for the control of catheter encrustation.* International Journal of Antimicrobial Agents, 2002. **19**(6): p. 499-506.

42. Harber, M., *Practical Nephrology*. 2014, Springer. p. 439-452.

43. Parapiboon, W., A. Ingsathit, S. Disthabanchong, A. Nongnuch, A. Jearanaipreprem, C. Charoenthanakit, S. Jirasiritham, and V. Sumethkul, *Impact of Early Ureteric Stent Removal and Cost-Benefit Analysis in Kidney Transplant Recipients: Results of a Randomized Controlled Study.* Transplantation Proceedings, 2012. **44**(3): p. 737-739.

44. Frederick, L., C. Ellimoottil, A. Kadlec, A. Shah, T. Turk, and B.F. Schwartz, *Cost analysis of metallic stents for chronic ureteral obstruction: a multicenter study.* Urology Practice, 2017. **4**(1): p. 21-24.

45. Buchholz, N., O. Hakenberg, C. Bach, and J. Masood, *Handbook of Urinary Stents: Basic Science and Clinical Applications*. 2016: JP Medical Ltd.

46. Kulkarni, R., *Ureteric Stenting*. 2017, John Wiley & Sons. p. 1-55.

47. Riedl, C.R., M. Witkowski, E. Plas, and H. Pflueger, *Heparin coating reduces encrustation of ureteral stents: a preliminary report.* International Journal of Antimicrobial Agents, 2002. **19**(6): p. 507-510.

48. Siggers, J.H., S. Waters, J. Wattis, and L. Cummings, *Flow dynamics in a stented ureter.* Mathematical Medicine and Biology-a Journal of the Ima, 2009. **26**(1): p. 1-24.

49. Waters, S.L., K. Heaton, J.H. Siggers, R. Bayston, M. Bishop, L.J. Cummings, D.M. Grant, J.M. Oliver, and J.A.D. Wattis, *Ureteric stents: investigating flow and encrustation.* Proceedings of the Institution of Mechanical Engineers Part H-Journal of Engineering in Medicine, 2008. **222**(H4): p. 551-561.

50. Cummings, L.J., S.L. Waters, J.A.D. Wattis, and S.J. Graham, *The effect of ureteric stents on urine flow: Reflux.* Journal of Mathematical Biology, 2004. **49**(1): p. 56-82.

51. Roos, R. and P.S. Lykoudis, *The fluid mechanics of the ureter.* Journal of Fluid Mechanics, 1971. **46**(04): p. 625-630.

52. Ramsay, J.W.A., S.R. Payne, P.T. Gosling, H.N. Whitfield, J.E.A. Wickham, and D.A. Levison, *The Effects of Double J Stenting on Unobstructed Ureters. An Experimental and Clinical Study*.* British Journal of Urology, 1985. **57**(6): p. 630-634.

53. Brewer, A.V., A.M. Elbahnasy, E. Bercowsky, K.L. Maxwell, A.L. Shalhav, S.A. Kahn, E.M. McDougall, and R.V. Clayman, *Mechanism of ureteral stent flow: A comparative in vivo study.* Journal of Endourology, 1999. **13**(4): p. 269-271.

54. Choong, S.K.S., S. Wood, and H.N. Whitfield, *A model to quantify encrustation on ureteric stents, urethral catheters and polymers intended for urological use.* BJU International, 2000. **86**(4): p. 414-421.

55. Gu, Y., J. Zhang, and G. Wang, *Use of cystourethroscopy to remove an indwelling double-J ureteral stent 6 years following simultaneous radical sigmoid colon cancer and partial bladder resection: A case report.* Experimental and therapeutic medicine, 2016. **11**(6): p. 2467-2469.

56. Halldorsson, S., E. Lucumi, R. Gómez-Sjöberg, and R.M.T. Fleming, *Advantages and challenges of microfluidic cell culture in polydimethylsiloxane devices.* Biosensors and Bioelectronics, 2015. **63**: p. 218-231.

57. Streets, A.M. and Y. Huang, *Chip in a lab: Microfluidics for next generation life science research.* Biomicrofluidics, 2013. **7**(1): p. 011302.

58. Velve-Casquillas, G., M. Le Berre, M. Piel, and P.T. Tran, *Microfluidic tools for cell biological research.* Nano today, 2010. **5**(1): p. 28-47.

59. Wong, K.H.K., J.M. Chan, R.D. Kamm, and J. Tien, *Microfluidic Models of Vascular Functions*, in *Annual Review of Biomedical Engineering, Vol 14*, M.L. Yarmush, Editor. 2012, Annual Reviews: Palo Alto. p. 205-230.

60. Kim, J., K. Yang, H.-J. Park, S.-W. Cho, S. Han, Y. Shin, S. Chung, and J.H. Lee, *Implantable microfluidic device for the formation of three-dimensional vasculature*

by human endothelial progenitor cells. Biotechnology and Bioprocess Engineering, 2014. **19**(3): p. 379-385.

61. Huh, D., B.D. Matthews, A. Mammoto, M. Montoya-Zavala, H.Y. Hsin, and D.E. Ingber, *Reconstituting Organ-Level Lung Functions on a Chip.* Science, 2010. **328**(5986): p. 1662-1668.

62. Lecuyer, S., R. Rusconi, Y. Shen, A. Forsyth, H. Vlamakis, R. Kolter, and H.A. Stone, *Shear Stress Increases the Residence Time of Adhesion of Pseudomonas aeruginosa.* Biophysical Journal, 2011. **100**(2): p. 341-350.

63. Lovchik, R.D., F. Bianco, M. Matteoli, and E. Delamarche, *Controlled deposition of cells in sealed microfluidics using flow velocity boundaries.* Lab on a Chip, 2009. **9**(10): p. 1395-1402.

64. Zhe, J., V. Modi, and K.R. Farmer, *A microfabricated wall shear-stress sensor with capacitative sensing.* Journal of Microelectromechanical Systems, 2005. **14**(1): p. 167-175.

65. Pan, J., T.X. Zhang, L. Mi, B.B. Zhang, B. Wang, L. Yang, L.H. Deng, and L.Y. Wang, *Stepwise Increasing and Decreasing Fluid Shear Stresses Differentially Regulate the Functions of Osteoblasts.* Cellular and Molecular Bioengineering, 2010. **3**(4): p. 376-386.

66. Krishnan B. Chandran, S.E.R., Ajit P. Yoganathan, *Biofluid Mechanics: The Human Circulation*. Second ed. 2012: CRC Press.

67. *Biofluid Mechanics: Blood Flow in Large Vessels*. 1991: Springer.

68. Davies, P., J.A. Spaan, and R. Krams, *Shear Stress Biology of the Endothelium.* Annals of Biomedical Engineering, 2005. **33**(12): p. 1714-1718.

69. Harms, J., X. Wang, T. Kim, X. Yang, and A.S. Rathore, *Defining process design space for biotech products: case study of Pichia pastoris fermentation.* Biotechnology progress, 2008. **24**(3): p. 655-662.

70. Acharya, G., C.H. Lee, and Y. Lee, *Optimization of cardiovascular stent against restenosis: factorial design-based statistical analysis of polymer coating conditions.* PLoS One, 2012. **7**(8): p. e43100.

71. Raju, P., M. Sarcar, and B. Satyanarayana, *Optimization of wire electric discharge machining parameters for surface roughness on 316 L stainless steel using full factorial experimental design.* Procedia Materials Science, 2014. **5**: p. 1670-1676.

72. Jiang, J., F.Q. Zhu, Q. Jiang, and L.F. Wang, *Extraction of a long-forgotten ureteral stent by ureteroscopic pneumatic lithotripsy.* Chinese Medical Journal, 2004. **117**(9): p. 1435-1436.

73. Yenicesu, M., E. Aydur, I. Yildirim, F. Yenicesu, and B. Seckin, *A long-forgotten indwelling ureteral stent in a renal transplant patient.* Transplantation Proceedings, 2004. **36**(5): p. 1395-1397.

74. Lai, D.H., Y.Z. He, Y.P. Dai, T. Li, M.L. Chen, and X. Li, *A Long-Forgotten Indwelling Single-J Stent in a Transplant Kidney.* Jcpsp-Journal of the College of Physicians and Surgeons Pakistan, 2014. **24**: p. S152-S154.

75. Brotherhood, H., D. Lange, and B.H. Chew, *Advances in ureteral stents.* Transl Androl Urol, 2014. **3**(3): p. 314-9.

76. Scameciu, I., S. Lupu, C. Pricop, and C. Scaneciu, *Morbidity and impact on quality of life in patients with indwelling ureteral stents: A 10-year clinical experience.* Pakistan Journal of Medical Sciences, 2015. **31**(3): p. 522-526.

77. Giannarini, G., F.X. Keeley, F. Valent, F. Manassero, A. Mogorovich, R. Autorino, and C. Selli, *Predictors of morbidity in patients with indwelling ureteric stents: results of a prospective study using the validated Ureteric Stent Symptoms Questionnaire.* Bju International, 2011. **107**(4): p. 648-654.

78. Singh, I., N.P. Gupta, A.K. Hemal, M. Aron, A. Seth, and P.N. Dogra, *Severely encrusted polyurethane ureteral stents: Management and analysis of potential risk factors.* Urology, 2001. **58**(4): p. 526-531.

79. Leibovici, D., A. Cooper, A. Lindner, R. Ostrowsky, J. Kleinmann, S. Velikanov, H. Cipele, E. Goren, and Y.I. Siegel, *Ureteral stents: Morbidity and impact on quality of life.* Israel Medical Association Journal, 2005. **7**(8): p. 491-494.

80. Dakkak, Y., A. Janane, T. Ould-Ismail, M. Ghadouane, A. Ameur, and M. Abbar, *Management of encrusted ureteral stents.* African Journal of Urology, 2012. **18**(3): p. 131-134.

81. *Urinary Tract Stone Disease*, ed. N.P.R. Kavanagh, M.P. Glenn, and P. John. 2011: Springer. 720.

82. Pansota, M.S., M. Rasool, M.S. Saleem, S.A. Tabassum, and A. Hussain, *Indications and complications of double J ureteral stenting: our experience.* Gomal Journal of Medical Sciences, 2013. **11**(1).

83. Ratner, B., *Biomaterials Science*. 2012: Academic Press. 1264.

84. Chew, B.H., D. Lange, R.F. Paterson, K. Hendlin, M. Monga, K.W. Clinkscales, S.W. Shalaby, and B.A. Hadaschik, *Next Generation Biodegradable Ureteral Stent in a Yucatan Pig Model.* The Journal of Urology, 2010. **183**(2): p. 765-771.

85. Wei-Jun, F., W. Zhong-Xin, L. Gang, C. Fu-Zhai, Z. Yuanyuan, and Z. Xu, *Comparison of a biodegradable ureteral stent versus the traditional double-J stent for the treatment of ureteral injury: an experimental study.* Biomedical Materials, 2012. **7**(6): p. 065002.

86. Mardis, H.K., T.W. Hepperlen, and H. Kammandel, *Double Pigtail Ureteral Stent.* Urology, 1979. **14**(1): p. 23-26.

87. Gorman, S.P., D.S. Jones, M.C. Bonner, M. Akay, and P.F. Keane, *Mechanical performance of polyurethane ureteral stents in vitro and ex vivo.* Biomaterials, 1997. **18**(20): p. 1379-1383.

88. Tunney, M.M., P.F. Keane, D.S. Jones, and S.P. Gorman, *Comparative assessment of ureteral stent biomaterial encrustation.* Biomaterials, 1996. **17**(15): p. 1541-1546.

89. Abrams, H.L., *Abrams' angiography: interventional radiology*. 2006: Lippincott Williams & Wilkins.

90. Hendlin, K., K. Dockendorf, C. Horn, N. Pshon, B. Lund, and M. Monga, *Ureteral stents: Coil strength and durometer.* Urology, 2006. **68**(1): p. 42-45.

91. Christman, M.S., J.O. L'Esperance, C.H. Choe, S.P. Stroup, and B.K. Auge, *Analysis of Ureteral Stent Compression Force and its Role in Malignant Obstruction.* Journal of Urology, 2009. **181**(1): p. 392-396.

92. Bregg, K. and R.A. Riehle, *Morbidity Associated with Indwelling Internal Ureteral Stents after Shock-Wave Lithotripsy.* Journal of Urology, 1989. **141**(3): p. 510-512.

93. Pryor, J.L., M.J. Langley, and A.D. Jenkins, *Comparison of Symptom Characteristics of Indwelling Ureteral Catheters.* Journal of Urology, 1991. **145**(4): p. 719-722.

94. Joshi, H.B., S.V. Chitale, M. Nagarajan, S.O. Irving, A.J. Browning, C.S. Biyani, and N.A. Burgess, *A prospective randomized single-blind comparison of ureteral stents composed of firm and soft polymer.* Journal of Urology, 2005. **174**(6): p. 2303-2306.

95. Lennon, G.M., J.A. Thornhill, P.A. Sweeney, R. Grainger, T.E. McDermott, and M.R. Butler, *'Firm' versus 'soft' double pigtail ureteric stents: a randomised blind comparative trial.* Eur Urol, 1995. **28**(1): p. 1-5.

96. Venkatesan, N., S. Shroff, K. Jayachandran, and M. Doble, *Polymers as Ureteral Stents.* Journal of Endourology, 2010. **24**(2): p. 191-198.

97. Beiko, D.T., B.E. Knudsen, and J.D. Denstedt, *Reviews in endourology - Advances in ureteral stent design.* Journal of Endourology, 2003. **17**(4): p. 195-199.

98. Denstedt, J., *Biomaterials and Tissue Engineering in Urology (Woodhead Publishing Series in Biomaterials)*, ed. J.D. Atala and Anthony. 2009: Woodhead Publishing Ltd. 592.

99. Liatsikos, E., P. Kallidonis, I. Kyriazis, C. Constantinidis, K. Hendlin, J.-U. Stolzenburg, D. Karnabatidis, and D. Siablis, *Ureteral obstruction: is the full metallic double-pigtail stent the way to go?* European urology, 2010. **57**(3): p. 480-487.

100. Kirby, R.S., S.R. Heard, P. Miller, I. Eardley, S. Holmes, J. Vale, J. Bryan, and S. Liu, *Use of the Asi Titanium Stent in the Management of Bladder Outflow Obstruction Due to Benign Prostatic Hyperplasia.* Journal of Urology, 1992. **148**(4): p. 1195-1197.

101. Song, H.-Y., H. Park, T.-S. Suh, G.-Y. Ko, T.-H. Kim, E.-S. Kim, and T. Park, *Recurrent traumatic urethral strictures near the external sphincter: treatment with a covered, retrievable, expandable nitinol stent—initial results.* Radiology, 2003. **226**(2): p. 433-440.

102. Papatsoris, A.G. and N. Buchholz, *A novel thermo-expandable ureteral metal stent for the minimally invasive management of ureteral strictures.* Journal of endourology, 2010. **24**(3): p. 487-491.

103. Finney, R.P., *Experience with New Double J-Ureteral Catheter Stent.* Journal of Urology, 1978. **120**(6): p. 678-681.

104. Al-Aown, A., I. Kyriazis, P. Kallidonis, P. Kraniotis, C. Rigopoulos, D. Karnabatidis, T. Petsas, and E. Liatsikos, *Ureteral stents: new ideas, new designs.* Ther Adv Urol, 2010. **2**(2): p. 85-92.

105. Finney, R.P., *Externally grooved ureteral stent*. 1981, Google Patents.

106. Skolnick, M.L., *Intra- and Extraluminal Fluid*, in *Real-time Ultrasound Imaging in the Abdomen*. 1981, Springer New York: New York, NY. p. 191-212.

107. Anderson, D.L. and J.T. Maerzke, *Spiral ureteral stent*. 1989, Google Patents.

108. Stoller, M.L., B.F. Schwartz, J.R. Frigstad, L. Norris, J.B. Park, and M.J. Magliochetti, *An in vitro assessment of the flow characteristics of spiral-ridged and smooth-walled JJ ureteric stents.* BJU Int, 2000. **85**(6): p. 628-31.

109. Mucksavage, P., D. Pick, D. Haydel, M. Etafy, D.C. Kerbl, J.Y. Lee, C. Ortiz-Vanderdys, F. Saleh, S. Olamendi, and M.K. Louie, *An in vivo evaluation of a novel spiral cut flexible ureteral stent.* Urology, 2012. **79**(3): p. 733-737.

110. Denstedt, J.D., *Advances in ureteral stent design.* Renal Stone Disease, 2007. **900**: p. 272-277.

111. Olweny, E.O., A.J. Portis, C.P. Sundaram, J.S. Afane, P.A. Humphrey, R. Ewers, E.M. McDougall, and R.V. Clayman, *Evaluation of a chronic indwelling prototype mesh ureteral stent in a porcine model.* Urology, 2000. **56**(5): p. 857-862.

112. Anis, R.R. and K.R. Karsch, *The future of drug eluting stents.* Heart, 2006. **92**(5): p. 585-588.

113. Liatsikos, E.N., D. Karnabatidis, G.C. Kagadis, K. Rokkas, C. Constantinides, N. Christeas, N. Flaris, T. Voudoukis, C.D. Scopa, P. Perimenis, K.S. Filos, G.C. Nikiforidis, J.-U. Stolzenburg, and D. Siablis, *Application of Paclitaxel-Eluting Metal Mesh Stents within the Pig Ureter: An Experimental Study.* European Urology, 2007. **51**(1): p. 217-223.

114. Lugmayr, H. and W. Pauer, *Self-expanding metal stents for palliative treatment of malignant ureteral obstruction.* American Journal of Roentgenology, 1992. **159**(5): p. 1091-1094.

115. Barbalias, G.A., D. Siablis, E.N. Liatsikos, D. Karnabatidis, S. Yarmenitis, K. Bouropoulos, and J. Dimopoulos, *Metal Stents: A New Treatment of Malignant Ureteral Obstruction.* The Journal of Urology, 1997. **158**(1): p. 54-58.

116. Burt, H.M. and W.L. Hunter, *Drug-eluting stents: A multidisciplinary success story.* Advanced Drug Delivery Reviews, 2006. **58**(3): p. 350-357.

117. Dunn, M.D., A.J. Portis, S.A. Kahn, Y. Yan, A.L. Shalhav, A.M. Elbahnasy, E. Bercowsky, D.M. Hoenig, J.S. Wolf, E.M. McDougall, and R.V. Clayman, *Clinical effectiveness of new stent design: Randomized single-blind comparison of tail and double-pigtail stents.* Journal of Endourology, 2000. **14**(2): p. 195-202.

118. Yew, J. and G. Bellman, *Modified "tubeless" percutaneous nephrolithotomy using a tail-stent.* Urology, 2003. **62**(2): p. 346-349.

119. BostonScientific, *Ureteral Stent Portfolio*, in *Boston Scientific*.

120. Scientific, B. *Ureteral Stent Portfolio - Boston Scientific*. Available from: http://www.google.co.uk/url?sa=t&rct=j&q=&esrc=s&source=web&cd=1&cad=rja&uact=8&ved=0CCEQFjAA&url=http%3A%2F%2Fwww.bostonscientific.com%2Fcontent%2Fdam%2Fbostonscientific%2Furo-wh%2Fportfolio-group%2Fureteral-stents%2FPercuflex-Brochure.pdf&ei=4L4JVaS9MoHV7AbU14HACA&usg=AFQjCNGSB0bOSjiX_X60VQfw9NTK9zGXnA&sig2=dFJob7e9_JRadPk3OmcpWw&bvm=bv.88198703,d.ZGU.

121. Netto, N.R., J. Ikonomidis, and C. Zillo, *Routine ureteral stenting after ureteroscopy for ureteral lithiasis: is it really necessary?* The Journal of urology, 2001. **166**(4): p. 1252-1254.

122. Taylor, W.N. and I.T. McDougall, *Minimally Invasive Ureteral Stent Retrieval.* The Journal of Urology, 2002. **168**(5): p. 2020-2023.

123. Hafron, J., M.C. Ost, B.J. Tan, J.D. Fogarty, D.M. Hoenig, B.R. Lee, and A.D. Smith, *Novel dual-lumen ureteral stents provide better ureteral flow than single ureteral stent in ex vivo porcine kidney model of extrinsic ureteral obstruction.* Urology, 2006. **68**(4): p. 911-915.

124. CookMedical, *Resonance Metallic Ureteral Stent brochure*. p. 2.

125. Wah, T., H. Irving, and J. Cartledge, *Initial Experience with the Resonance Metallic Stent for Antegrade Ureteric Stenting.* CardioVascular and Interventional Radiology, 2007. **30**(4): p. 705-710.

126. Facs, P.M.H.M.D.M.P.H., J.G.M.D.M.P.H. Thomas, S.B.M. MD, and J.W.M.D.P. Alan, *Penn Clinical Manual of Urology: Expert Consult - Online and Print, 2e*. 2014: Saunders. 960.

127. Ryan, P.C., G.M. Lennon, P.A. Mclean, and J.M. Fitzpatrick, *The Effects of Acute and Chronic Jj Stent Placement on Upper Urinary-Tract Motility and Calculus Transit.* British Journal of Urology, 1994. **74**(4): p. 434-439.

128. Monga, M., *Ureteroscopy (Current Clinical Urology)*. 2012: Springer. 494.

129. Md, K.V., *The Practice of Interventional Radiology, with online cases and video: Expert Consult Premium Edition - Enhanced Online Features and Print, 1e (Expert Consult Title: Online + Print)*. 2011: Saunders. 784.

130. Rowlands, A.B., F.M. Peter, and Brian, *ABC of Tubes, Drains, Lines and Frames (ABC Series)*. 2008: Wiley-Blackwell. 88.

131. Bach, N.B., H. Oliver, M. Junaid, and J. Christian, *Handbook of Urinary Stents: Basic Science and Clinical Applications*. 2016: JP Medical Ltd. 376.

132. *Ureteral Stone Management: A Practical Approach*, ed. S.R.P. Nakada and Y. Stephen. 2014: Springer. 232.

133. Dyer, R.B., M.Y. Chen, R.J. Zagoria, J.D. Regan, C.G. Hood, and P.V. Kavanagh, *Complications of Ureteral Stent Placement.* RadioGraphics, 2002. **22**(5): p. 1005-1022.

134. Paick, S.H., H.K. Park, S.-J. Oh, and H.H. Kim, *Characteristics of bacterial colonization and urinary tract infection after indwelling of double-J ureteral stent.* Urology, 2003. **62**(2): p. 214-217.

135. Lasser, M. and G. Pareek, *Smith's Textbook of Endourology*. 2012, Wiley-Blackwell.

136. Wilks, S.A., M.J. Fader, and C.W. Keevil, *Novel insights into the Proteus mirabilis crystalline biofilm using real-time imaging.* PloS one, 2015. **10**(10): p. e0141711.

137. Liatsikos, E.N., D. Karnabatidis, G.C. Kagadis, K. Rokkas, C. Constantinides, N. Christeas, N. Flaris, T. Voudoukis, C.D. Scopa, P. Perimenis, K.S. Filos, G.C. Nikiforidis, J.U. Stolzenburg, and D. Siablis, *Application of paclitaxel-eluting metal mesh stents within the pig ureter: An experimental study.* European Urology, 2007. **51**(1): p. 217-223.

138. Liatsikos, E., D. Karnabatidis, P. Kallidonis, and D. Siablis, *Metal stents in the upper urinary tract.* Biomaterials and Tissue Engineering in Urology, 2009: p. 104-133.

139. Ducheyne, P., K. Healy, and D. Hutmacher, *In Comprehensive Biomaterials II.* Ducheyne, P., Grainger, DB, Healy, KE, Hutmacher, DW, Kirkpatrick, CJ, Eds, 2017: p. 2017.

140. Liatsikos, E., P. Kallidonis, I. Kyriazis, C. Constantinidis, K. Hendlin, J.U. Stolzenburg, D. Karnabatidis, and D. Siablis, *Ureteral Obstruction: Is the Full Metallic Double-Pigtail Stent the Way to Go?* European Urology, 2010. **57**(3): p. 480-486.

141. Grases, F., M. Ramis, A. Villacampa, and A. Costa-Bauza, *Uric acid urolithiasis and crystallization inhibitors.* Urologia internationalis, 1999. **62**(4): p. 201-204.

142. Hildebrandt, P., M. Sayyad, A. Rzany, M. Schaldach, and H. Seiter, *Prevention of surface encrustation of urological implants by coating with inhibitors.* Biomaterials, 2001. **22**(5): p. 503-507.

143. Fellström, B., B.D. Danielson, F.A. Karlsson, and S. Ljunghall, *Crystal Inhibition:Binding of Heparin and Chondroitin Sulphate to Calcium Oxalate, Sodium Urate and Uric Acid Crystals,* in *Urolithiasis and Related Clinical Research,* P.O. Schwille, et al., Editors. 1985, Springer US: Boston, MA. p. 831-834.

144. Cauda, F., V. Cauda, C. Fiori, B. Onida, and E. Garrone, *Heparin coating on ureteral Double J stents prevents encrustations: an in vivo case study.* Journal of endourology, 2008. **22**(3): p. 465-472.

145. Watterson, J.D., P.A. Cadieux, D.T. Beiko, A.J. Cook, J.P. Burton, R.R. Harbottle, C. Lee, E. Rowe, H. Sidhu, G. Reid, and J.D. Denstedt, *Oxalate-degrading enzymes from Oxalobacter formigenes: A novel device coating to reduce urinary tract biomaterial-related encrustation.* Journal of Endourology, 2003. **17**(5): p. 269-274.

146. Grill, A., *Diamond-like carbon coatings as biocompatible materials—an overview.* Diamond and Related Materials, 2003. **12**(2): p. 166-170.

147. Laube, N., L. Kleinen, J. Bradenahl, and A. Meissner, *Diamond-Like Carbon Coatings on Ureteral Stents—A New Strategy for Decreasing the Formation of Crystalline Bacterial Biofilms?* The Journal of Urology, 2007. **177**(5): p. 1923-1927.

148. John, T., A. Rajpurkar, G. Smith, M. Fairfax, and J. Triest, *Antibiotic pretreatment of hydrogel Ureteral Stent.* Journal of Endourology, 2007. **21**(10): p. 1211-1215.

149. Campbell, E.J., V. O'byrne, P.W. Stratford, I. Quirk, T.A. Vick, M.C. Wiles, and Y.P. Yianni, *Biocompatible surfaces using methacryloylphosphorylcholine laurylmethacrylate copolymer.* Asaio Journal, 1994. **40**(3): p. M853-M857.

150. Lo, J., D. Lange, and B.H. Chew, *Ureteral stents and foley catheters-associated urinary tract infections: the role of coatings and materials in infection prevention.* Antibiotics, 2014. **3**(1): p. 87-97.

151. Raad, I., H. Hanna, Y. Jiang, T. Dvorak, R. Reitzel, G. Chaiban, R. Sherertz, and R. Hachem, *Comparative activities of daptomycin, linezolid, and tigecycline against catheter-related methicillin-resistant Staphylococcus bacteremic isolates embedded in biofilm.* Antimicrobial agents and chemotherapy, 2007. **51**(5): p. 1656-1660.

152. Rose, W.E. and P.T. Poppens, *Impact of biofilm on the in vitro activity of vancomycin alone and in combination with tigecycline and rifampicin against Staphylococcus aureus.* Journal of Antimicrobial Chemotherapy, 2008. **63**(3): p. 485-488.

153. Cirioni, O., A. Giacometti, R. Ghiselli, G. Dell'Acqua, Y. Gov, W. Kamysz, J. Łukasiak, F. Mocchegiani, F. Orlando, and G. D'Amato, *Prophylactic efficacy of topical temporin A and RNAIII-inhibiting peptide in a subcutaneous rat Pouch model of graft infection attributable to staphylococci with intermediate resistance to glycopeptides.* Circulation, 2003. **108**(6): p. 767-771.

154. Singh, R., P. Ray, A. Das, and M. Sharma, *Penetration of antibiotics through Staphylococcus aureus and Staphylococcus epidermidis biofilms.* Journal of antimicrobial chemotherapy, 2010. **65**(9): p. 1955-1958.

155. Minardi, D., O. Cirioni, R. Ghiselli, C. Silvestri, F. Mocchegiani, E. Gabrielli, G. d'Anzeo, A. Conti, F. Orlando, M. Rimini, L. Brescini, M. Guerrieri, A. Giacometti, and G. Muzzonigro, *Efficacy of Tigecycline and Rifampin Alone and in Combination against Enterococcus faecalis Biofilm Infection in a Rat Model of Ureteral Stent.* Journal of Surgical Research, 2012. **176**(1): p. 1-6.

156. Yang, L., S. Whiteside, P.A. Cadieux, and J.D. Denstedt, *Ureteral stent technology: Drug-eluting stents and stent coatings.* Asian Journal of Urology, 2015. **2**(4): p. 194-201.

157. Chung, H.-H., S.H. Lee, S.B. Cho, H.S. Park, Y.S. Kim, B.C. Kang, J.K. Frisoli, and M.K. Razavi, *Comparison of a New Polytetrafluoroethylene-Covered Metallic Stent to a Noncovered Stent in Canine Ureters.* CardioVascular and Interventional Radiology, 2008. **31**(3): p. 619-628.

158. Lange, D., C.N. Elwood, K. Choi, K. Hendlin, M. Monga, and B.H. Chew, *Uropathogen Interaction With the Surface of Urological Stents Using Different Surface Properties.* The Journal of Urology, 2009. **182**(3): p. 1194-1200.

159. Nowatzki, P.J., R.R. Koepsel, P. Stoodley, K. Min, A. Harper, H. Murata, J. Donfack, E.R. Hortelano, G.D. Ehrlich, and A.J. Russell, *Salicylic acid-releasing polyurethane acrylate polymers as anti-biofilm urological catheter coatings.* Acta Biomaterialia, 2012. **8**(5): p. 1869-1880.

160. Carlson, R.P., R. Taffs, W.M. Davison, and P.S. Stewart, *Anti-biofilm properties of chitosan-coated surfaces.* Journal of Biomaterials Science, Polymer Edition, 2008. **19**(8): p. 1035-1046.

161. Yang, S.H., Y.S.J. Lee, F.H. Lin, J.M. Yang, and K.s. Chen, *Chitosan/poly (vinyl alcohol) blending hydrogel coating improves the surface characteristics of segmented polyurethane urethral catheters.* Journal of Biomedical Materials Research Part B: Applied Biomaterials, 2007. **83**(2): p. 304-313.

162. Siggers, J.H., S. Waters, J. Wattis, and L. Cummings, *Flow dynamics in a stented ureter.* Mathematical medicine and biology: a journal of the IMA, 2008. **26**(1): p. 1-24.

163. Waters, S., K. Heaton, J. Siggers, R. Bayston, M. Bishop, L. Cummings, D. Grant, J. Oliver, and J. Wattis, *Ureteric stents: investigating flow and encrustation.* Proceedings of the Institution of Mechanical Engineers, Part H: Journal of Engineering in Medicine, 2008. **222**(4): p. 551-561.

164. Carugo, D., X. Zhang, J.M. Drake, and F. Clavica. *Formation and characteristics of laminar vortices in microscale environments within an obstructed and stented ureter: a computational study*. in *Proceedings of the 18th International Conference on Miniaturized Systems for Chemistry and Life Sciences, MicroTAS 2014*. 2014.

165. Clavica, F., X. Zhao, M. ElMahdy, M.J. Drake, X. Zhang, and D. Carugo, *Investigating the flow dynamics in the obstructed and stented ureter by means of a biomimetic artificial model.* PloS one, 2014. **9**(2): p. e87433.

166. Hofmann, R. and R. Hartung, *Ureteral stents—materials and new forms.* World Journal of Urology, 1989. **7**(3): p. 154-157.

167. Mardis, H.K., R.M. KROEGER, J.J. MORTON, and J.M. DONOVAN, *Comparative evaluation of materials used for internal ureteral stents.* Journal of endourology, 1993. **7**(2): p. 105-115.

168. Lugmayr, H. and W. Pauer, *Self-expanding metal stents for palliative treatment of malignant ureteral obstruction.* AJR. American journal of roentgenology, 1992. **159**(5): p. 1091-1094.

169. Abrams, H.L., *Abrams' angiography: interventional radiology*. 2006, Lippincott Williams & Wilkins. p. 669 - 697.

170. Chung, S.Y., R.J. Stein, D. Landsittel, B.J. Davies, D.C. Cuellar, R.L. Hrebinko, T. Tarin, and T.D. Averch, *15-year experience with the management of extrinsic ureteral obstruction with indwelling ureteral stents.* The Journal of urology, 2004. **172**(2): p. 592-595.

171. Lange, D., S. Bidnur, N. Hoag, and B.H. Chew, *Ureteral stent-associated complications [mdash] where we are and where we are going.* Nature Reviews Urology, 2015. **12**(1): p. 17-25.

172. Lange, D. and B.H. Chew, *Update on ureteral stent technology.* Therapeutic Advances in Urology, 2009. **1**(3): p. 143-148.

173. Tofft, H.P., J. Frøkiœr, J. Mortensen, and J.C. Djurhuus, *Renal Pelvic Peristalsis in Pigs during Standardized Flow Rate Variations1*. Urologia internationalis, 1986. **41**(4): p. 292-298.

174. Carugo, D., J.Y. Lee, A. Pora, R.J. Browning, L. Capretto, C. Nastruzzi, and E. Stride, *Facile and cost-effective production of microscale PDMS architectures using a combined micromilling-replica moulding (μMi-REM) technique.* Biomedical microdevices, 2016. **18**(1): p. 4.

175. Brooks, T. and C.W. Keevil, *A simple artificial urine for the growth of urinary pathogens.* Lett Appl Microbiol, 1997. **24**(3): p. 203-6.

176. Hobbs, T., L.N. Schultz, E.G. Lauchnor, R. Gerlach, and D. Lange, *Evaluation of Biofilm Induced Urinary Infection Stone Formation in a Novel Laboratory Model System.* The Journal of urology, 2018. **199**(1): p. 178-185.

177. Tong, J.C.K., E.M. Sparrow, and J.P. Abraham, *Numerical Simulation of the Urine Flow in a Stented Ureter.* Journal of Biomechanical Engineering, 2006. **129**(2): p. 187-192.

178. Olweny, E.O., A.J. Portis, J.S. Afane, A.V. Brewer, A.L. Shalhav, K. Luszczynski, E.M. McDOUGALL, and R.V. Clayman, *Flow characteristics of 3 unique ureteral stents: investigation of a poiseuille flow pattern.* The Journal of urology, 2000. **164**(6): p. 2099-2103.

179. Stoller, M., B. Schwartz, J. Frigstad, L. Norris, J. Park, and M. Magliochetti, *An in vitro assessment of the flow characteristics of spiral-ridged and smooth-walled JJ ureteric stents.* BJU international, 2000. **85**(6): p. 628-631.

180. Gorman, S.P., C.P. Garvin, F. Quigley, and D.S. Jones, *Design and validation of a dynamic flow model simulating encrustation of biomaterials in the urinary tract.* Journal of Pharmacy and Pharmacology, 2003. **55**(4): p. 461-468.

181. Choong, S., S. Wood, and H. Whitfield, *A model to quantify encrustation on ureteric stents, urethral catheters and polymers intended for urological use.* BJU international, 2000. **86**(4): p. 414-421.

182. Gordon, N., *Stalactites and Stalagmites: Crystal Formation on Ureteric Double-J Stents.* BJU International, 1989. **64**(2): p. 195-197.

183. Buchholz, N., O. Hakenberg, C. Bach, and J. Masood, *Handbook of Urinary Stents: Basic Science and Clinical Applications*. 2016, JP Medical Ltd. p. 7-14.

184. Kawahara, T., H. Ishida, Y. Kubota, and J. Matsuzaki, *Ureteroscopic removal of forgotten ureteral stent.* BMJ case reports, 2012. **2012**: p. bcr0220125736.

185. Singh, I., N. Gupta, A. Hemal, M. Aron, A. Seth, and P. Dogra, *Severely encrusted polyurethane ureteral stents: management and analysis of potential risk factors.* Urology, 2001. **58**(4): p. 526-531.

186. Kim, K.-W., Y.H. Choi, S.B. Lee, Y. Baba, H.-H. Kim, and S.-H. Suh, *Numerical analysis of the effect of side holes of a double J stent on flow rate and pattern.* Biomedical materials and engineering, 2015. **26**(s1): p. S319-S327.

187. Damiano, R., R. Autorino, M. De Sio, F. Cantiello, G. Quarto, S. Perdonà, R. Sacco, and M. D'Armiento, *Does the size of ureteral stent impact urinary symptoms and quality of life? A prospective randomized study.* European urology, 2005. **48**(4): p. 673-678.

188. Tong, J.C., E.M. Sparrow, and J.P. Abraham, *Numerical simulation of the urine flow in a stented ureter.* Journal of biomechanical engineering, 2007. **129**(2): p. 187-192.

189. Wilks, S.A., M.J. Fader, and C.W. Keevil, *Novel Insights into the Proteus mirabilis Crystalline Biofilm Using Real-Time Imaging.* Plos One, 2015. **10**(10).

190. Lykoudis, P.S. and R. Roos, *The fluid mechanics of the ureter from a lubrication theory point of view.* Journal of Fluid Mechanics, 1970. **43**(04): p. 661-674.

191. Band, L.R., L.J. Cummings, S.L. Waters, and J.A.D. Wattis, *Modelling crystal aggregation and deposition in the catheterised lower urinary tract.* Journal of Mathematical Biology, 2009. **59**(6): p. 809-840.

192. Tong, J.C.K., E.M. Sparrow, and J.P. Abraham, *Numerical simulation of the urine flow in a stented ureter.* Journal of Biomechanical Engineering-Transactions of the Asme, 2007. **129**(2): p. 187-192.

193. Gomez-Blanco, J.C., Mart, F.J. Martinez-Reina, D. Cruz, J.B. Pagador, F.M. Sanchez-Margallo, and F. Soria, *Fluid Structural Analysis of Urine Flow in a Stented Ureter.* Computational and Mathematical Methods in Medicine, 2016. **2016**: p. 7.

194. Brooks, T. and C.W. Keevil, *A simple artificial urine for the growth of urinary pathogens.* Letters in Applied Microbiology, 1997. **24**(3): p. 203-206.

195. Carugo, D., J.Y. Lee, A. Pora, R.J. Browning, L. Capretto, C. Nastruzzi, and E. Stride, *Facile and cost-effective production of microscale PDMS architectures using a combined micromilling-replica moulding (μMi-REM) technique.* Biomedical Microdevices, 2016. **18**: p. 4.

196. Kwon, C.-I. and G.A. Lehman, *Mechanisms of Biliary Plastic Stent Occlusion and Efforts at Prevention.* Clinical Endoscopy, 2016. **49**(2): p. 139-146.

197. Koizumi, K., S. Masuda, J.H. Sung, and M. Kako, *Removal of a biliary stent encrusted with a large stone by use of a new digital cholangioscope with a holmium: yttrium aluminum garnet laser.* VideoGIE, 2016. **1**(2): p. 40-42.

198. Farnbacher, M.J., R. Lederer, A. Blana, and H.T. Schneider, *Does heparin coating reduce encrustation of biliary plastic endoprostheses? A prospective randomized trial.* Scandinavian Journal of Gastroenterology, 2012. **47**(10): p. 1141-1147.

199. Qin, Y., *Micromanufacturing engineering and technology*. 2010, William Andrew. p. 1-34.

200. Ghebre-Selassie, I., C.E. Martin, F. Zhang, and J. DiNunzio, *Pharmaceutical extrusion technology*. 2018, CRC Press. p. 267-310.

201. Towbin, R. and K. Baskin, *Pediatric interventional radiology*. 2015, Cambridge University Press. p. 297-356.

202. Lantada, A.D. and P.L. Morgado, *General Considerations for the Development of Biomedical Devices*, in *Handbook on Advanced Design and Manufacturing Technologies for Biomedical Devices*. 2013, Springer. p. 19-45.

203. Esawi, A. and M.F. Ashby, *Cost-based ranking for manufacturing process selection*, in *Integrated Design and Manufacturing in Mechanical Engineering'98*. 1999, Springer. p. 603-610.

204. Negarestani, R. and L. Li, *Laser machining of fibre-reinforced polymeric composite materials*, in *Machining Technology for Composite Materials*. 2012, Elsevier. p. 288-308.

205. Alting, L., F. Kimura, H.N. Hansen, and G. Bissacco, *Micro engineering.* CIRP Annals-Manufacturing Technology, 2003. **52**(2): p. 635-657.

206. Yen, D.P., Y. Ando, and K. Shen, *A cost-effective micromilling platform for rapid prototyping of microdevices.* Technology, 2016. **4**(4): p. 234-239.

207. Tugrul, Ã., *Biomedical devices: design, prototyping, and manufacturing*. 2016, John Wiley & Sons. p. 79-160.

208. Guckenberger, D.J., T.E. de Groot, A.M.D. Wan, D.J. Beebe, and E.W.K. Young, *Micromilling: A method for ultra-rapid prototyping of plastic microfluidic devices.* Lab on a chip, 2015. **15**(11): p. 2364-2378.

209. Shih, A.J., J. Luo, M.A. Lewis, and J.S. Strenkowski, *Chip morphology and forces in end milling of elastomers.* Journal of Manufacturing Science and Engineering, 2004. **126**(1): p. 124-130.

210. Ion, J., *Laser processing of engineering materials. 2005*, in *Elsevier Butterworth-Heinemann, ISBN 0*. 2005. p. 347-383.

211. Kong, C., *Water-Jet Cutting*, in *CIRP Encyclopedia of Production Engineering*, L. Laperrière and G. Reinhart, Editors. 2014, Springer Berlin Heidelberg: Berlin, Heidelberg. p. 1297-1301.

212. Chen, F.L. and E. Siores, *The effect of cutting jet variation on striation formation in abrasive water jet cutting.* International Journal of Machine Tools and Manufacture, 2001. **41**(10): p. 1479-1486.

213. Krajcarz, D., *Comparison Metal Water Jet Cutting with Laser and Plasma Cutting.* Procedia Engineering, 2014. **69**: p. 838-843.

214. Grote, K.-H. and E.K. Antonsson, *Springer handbook of mechanical engineering*. 2009, Springer Science & Business Media. p. 606-655.

215. Tschätsch, H., *Applied machining technology*. 2010, Springer Science & Business Media. p. 325-348.

216. Tenke, P., C.R. Riedl, G.L. Jones, G.J. Williams, D. Stickler, and E. Nagy, *Bacterial biofilm formation on urologic devices and heparin coating as preventive strategy.* International Journal of Antimicrobial Agents, 2004. **23**: p. 67-74.